

ALMA MATER STUDIORUM · UNIVERSITY OF BOLOGNA

---

School of Science  
Department of Physics and Astronomy  
Master Degree in Physics

# Constraining leptophilic dark matter with KM3NeT

Supervisor:  
Prof. Fabio Maltoni

Submitted by:  
Veronika Fedotova

Co-supervisor:  
Dr. Chiara Arina

Academic Year 2019/2020

## Abstract

Revealing the nature of the dark matter is among the most puzzling issues of today particle physics, astrophysics and cosmology. Given the striking evidences for dark matter at all astrophysical scales, starting from galactic and going to cosmological scales, a widespread and well motivated assumption on the nature of the dark matter is that it is made by a new particle that extends the Standard Models of Particle Physics.

Indirect detection of dark matter, which annihilates in over-dense regions like the galactic centre, is an important probe of a possible dark matter interaction with the Standard Model particles. It could provide insights both to the underlying production mechanism of dark matter in the early Universe, on the annihilation properties at present time in galactic halos and on the underlying particle physics model.

In this master thesis project we will focus on simplified leptophilic models for dark matter. These models feature an massive boson, called for instance  $Z'$ , and a Dirac dark matter candidate, that complement the Standard Model of particle physics. We will study the annihilation of dark matter into leptons, focusing in particular on neutrino lines and box-shaped energy spectra. These tow signals are smoking gun signature to discover the dark matter properties. We will perform a numerical analysis using the dark matter software MADDM to predict the expected flux from the galactic centre, by performing scans in the model parameter space. We will implement the constrains from the Fermi-LAT telescope and the XENON1T experiment. Finally we will use the predictions of those models to assess the reach of the future KM3NeT neutrino telescope.

# Contents

<b>1</b>	<b>Introduction</b>	<b>3</b>
<b>2</b>	<b>History of the Universe</b>	<b>6</b>
2.1	A brief review of cosmology . . . . .	6
2.2	Thermal History . . . . .	11
2.2.1	Early Universe . . . . .	11
2.2.2	Entropy conservation . . . . .	15
2.2.3	Departure from Equilibrium . . . . .	16
2.3	Structure formation . . . . .	20
2.4	Dark matter evidences . . . . .	23
2.4.1	Rotation curves of galaxies . . . . .	23
2.4.2	The Cosmic Microwave Background . . . . .	25
2.4.3	Gravitational lensing . . . . .	27
<b>3</b>	<b>Dark matter</b>	<b>29</b>
3.1	A first classification . . . . .	29
3.1.1	The standard $\Lambda$ CDM model . . . . .	31
3.2	Overview of dark matter candidates . . . . .	31
3.2.1	Non-WIMP candidates . . . . .	33
3.2.2	WIMP candidates . . . . .	36
3.3	Detection methods . . . . .	38
3.3.1	Indirect detection . . . . .	39
3.3.2	Direct detection . . . . .	46
3.3.3	Collider searches . . . . .	47
3.4	Experimental constrains . . . . .	49
3.4.1	Indirect detection experiments . . . . .	49
3.4.2	Direct detection experiments . . . . .	52
3.4.3	Experimental bounds from collider searches . . . . .	53

<b>4</b>	<b>Simplified models</b>	<b>55</b>
4.1	Simplified models vs EFT approach . . . . .	56
4.2	Model building and motivations . . . . .	57
4.3	Spin 1-s-channel mediator . . . . .	58
4.4	Numerical tools . . . . .	62
4.4.1	MADDM . . . . .	63
4.4.2	RUNDM . . . . .	64
4.5	State of the art of the experimental constraints . . . . .	65
4.6	Spin 1-s-channel results . . . . .	66
4.7	Secluded WIMP dark matter . . . . .	67
4.7.1	Sommerfeld enhancement . . . . .	69
4.7.2	Secluded model: $m_{Z'} \simeq m_\chi$ case . . . . .	72
4.7.3	Secluded models: $m_{Z'} \ll m_\chi$ case . . . . .	74
4.8	$L_\mu - L_\tau$ gauge model . . . . .	75
<b>5</b>	<b>Conclusions and outlook</b>	<b>81</b>

# Chapter 1

## Introduction

Revealing the nature of the dark matter is among one of the most puzzling issues of today's particle physics, astrophysics and cosmology. Despite plenty of evidence, which include the measurement of galactic rotation curves, the Cosmic Microwave Background, gravitational lensing, and that confirm the presence of non baryonic matter in our Universe, its nature remains elusive. Currently, we know that dark matter should satisfy a few properties: it interacts gravitationally and it represents 26% of the energy budget of the Universe and more than 80% of its total matter content, according to the latest measurements by the Planck satellite [1].

Given the stunning evidence at all astrophysical and cosmological scales, a widespread assumption on the nature of the dark matter is that it is composed by new particles that extend the content of the Standard Model of particle physics. Many different types of dark matter candidates have been proposed, i.e., axions [2], supersymmetric neutralinos [3], sterile neutrinos [4] just to name a few. They are expected in different mass ranges and with interaction strength. However, they share the characteristics of being neutral, stable (or long-lived on Universe timescales), and hopefully interacting with the Standard Model particles other than gravitationally. In this thesis we will focus on the so-called Weakly Interacting Massive Particle (WIMP) scenarios, where massive dark matter particles can interact weakly with the known particles.

Based on the assumptions above, WIMPs have been in thermal equilibrium in the early Universe and have decoupled via the freeze-out mechanism to provide the relic abundance measured today. At present time, the dark matter particles are widespread in our galaxy, hence they can be detected by Earth or space-based experiments and satellites. The three main strategies to uncover the dark matter are: (i) indirect detection, which studies the products of dark matter annihilation in locally over-dense regions such as the galactic center; (ii) direct detection that studies scattering processes between nuclei in underground detectors, hit by dark matter particles and (iii) colliders, that can produce dark matter particles through collision of Standard Model particles to further search for missing energy signals. These methods and their combination are designed to

---

provide insights on the dark matter characteristics.

Indirect dark matter detection is based on the measurement of a flux of stable particles ( $e^+$ ,  $e^-$ ,  $p$ ,  $\bar{p}$ ,  $\nu_e$ ,  $\nu_\mu$ ,  $\nu_\tau$  and  $\gamma$ ), which are the primary products of dark matter annihilation in the galactic halo. Typically, these spectra feature a continuous and smooth energy distribution of e.g. gamma rays or neutrinos, as a result of the showering, hadronization, decay of the dark matter annihilation final states. Consequently, such energy spectra are not clearly distinguishable from the astrophysical background, making the discovery of dark matter signals a very challenging task. For this reason, it is convenient to focus on signatures which can provide sharp features in the energy spectra. The spectral features are considered smoking gun signatures for dark matter detection, because they can be easily distinguished from the astrophysical background and are hardly mimicked by any astrophysical source. Striking examples of spectral features are the monochromatic lines and box-shaped energy spectra. The first are obtained by annihilation of dark matter in two  $\gamma$  or into a  $\nu\bar{\nu}$  pair, while the latter by dark matter decaying into a pair of boosted and unstable particles which further decay into pairs of photons or neutrinos.

In this thesis we focus on dark matter models that give rise to neutrino line signals at the tree level, using a simplified model approach. This consists in adding to the Standard Model a minimal content: a dark matter particle and a mediator particle, which connects the dark matter to the Standard Model. In particular, we consider a s-channel simplified model [5, 6] with a Dirac dark matter candidate,  $\chi$ , annihilating into Standard Model particles via a massive spin-1 mediator,  $Z'$ . This model features a velocity independent annihilation cross section  $\langle\sigma v\rangle$ , which proceeds primarily through s-wave. This is promising because at present time  $\langle\sigma v\rangle$  is not suppressed by the small velocity of the dark matter in the galaxy and can give rise to signals in the ballpark of detection of current and future experiments. Moreover, by considering only couplings to leptons (leptophilic model), this model not only provides potentially visible and detectable signals but also smoking gun signatures for neutrino telescopes, searching for heavy dark matter well beyond the reach of colliders.

After computing analytically the cross section leading to neutrino monochromatic lines, we perform a numerical analysis using the dark matter software MadDM [7] to predict the expected flux from the galactic centre of those neutrinos. We perform scans in the model parameter space for different realisations of our leptophilic simplified model. MADDM is used to compute the annihilation cross section  $\langle\sigma v\rangle$  relevant for both the relic density and the indirect detection computations, as well as to compare the theoretical observables against the experimental results from indirect and direct searches. More specifically, we consider the experimental bounds of Fermi-LAT [8] for indirect detection and XENON1T [9] for direct detection.

Our main goal is to use the predictions of this model to assess the reach of the future KM3NeT [10] neutrino telescope to leptophilic dark matter models. KM3NeT is already in construction in the Mediterranean sea, hence it has the optimal position to observe dark matter annihilation from the galactic centre. We use two different predictions for

---

KM3NeT sensitivity considering both the angular power spectrum method [11] and the predictions made with a likelihood analysis and based on ANTARES data [12].

This thesis is organized as follows. In chapter 2, we briefly review the relevant concepts of cosmology to understand the production of the dark matter in the early Universe; we further provide a description of the main evidences for dark matter at different astrophysical scales. In chapter 3, we provide examples of particle dark matter candidates and describe the main detection methods and experimental limits related to weakly interacting candidates. Finally in chapter 4 we provide a detailed description of the work performed during this thesis. We first present the Simplified Model for neutrino lines and the different realisation we have considered; we then show the results of the model parameter scans performed with the numerical tool MADDM and further assess the limits set by current experiments on this parameter space, and most importantly, we show the reach of the future KM3NeT neutrino telescope. We finally conclude and discuss future prospects in chapter 5.

# Chapter 2

## History of the Universe

This chapter is a brief review of the most important concepts in cosmology. We will derive a few key concepts of General Relativity and underline the equations that govern the evolution of the Universe in sec. 2.1.

In sec. 2.2 we will show how to treat the Universe from a thermodynamical point of view, by describing the early Universe thermodynamics. We further analyse the decoupling of species in sec. 2.2.1 using the Boltzmann equation.

We will illustrate how the structures such as galaxies and galaxy clusters can be explained in terms of perturbation theory in sec. 2.3.

Finally, we will show in sec. 2.4 how the necessity for dark matter emerges in a natural way and which are the experimental evidences for it. This is just a summary of different topics; one can find a more complete treatment in different books, such as [13, 14]. For this thesis we follow [15, 16, 17].

### 2.1 A brief review of cosmology

Cosmology uses the framework of General Relativity that provides a description of gravity as a geometric property of four-dimensional spacetime, unifying Special Relativity and Newton's law of universal gravitation. In particular, the curvature of spacetime is directly related to the stress-energy tensor. The relation is specified by the Einstein field equations

$$R_{\mu\nu} - \frac{1}{2}g_{\mu\nu}R + \Lambda g_{\mu\nu} = 8\pi G_N T_{\mu\nu}, \quad (2.1)$$

where  $g_{\mu\nu}$  is the spacetime metric tensor,  $R_{\mu\nu}$  is the Ricci tensor (1-4 contraction of the Riemann tensor  $R^\mu_{\nu\rho\sigma}$ ),  $R = g^{\mu\nu}R_{\mu\nu}$  is the Ricci scalar,  $\Lambda$  is the cosmological constant,  $G_N$  is the gravitational constant and finally  $T_{\mu\nu}$  is the energy momentum tensor.

Einstein's eq. (2.1) can be solved assuming the cosmological principle to obtain a metric that describes the Universe at large scales. The cosmological principle states that

on the largest scales, the Universe is spatially homogeneous and isotropic. Homogeneity means that the Universe looks identical at every point in space while isotropy that it looks the same in every direction. Notice that these properties are referred to space, not to time. The cosmological principle is confirmed by both the Cosmic Microwave Background (CMB) that we will discuss afterwards in sec. 2.4.2 and by redshift surveys, according which galaxies are roughly homogeneous at large distances.

Assuming the cosmological principle, the solution of eq. (2.1) is the Friedmann-Lemaître-Robertson-Walker (FLRW) metric

$$ds^2 = dt^2 - a^2(t) \left( \frac{dr^2}{1 - kr^2} + r^2 d\theta^2 + r^2 \sin^2 \theta d\phi^2 \right), \quad (2.2)$$

where  $r, \theta, \phi$  are the spherical coordinates,  $k$  represents the curvature and  $a(t)$  is the scale factor. The curvature can have 3 different values:  $k = +1$  represents a closed Universe,  $k = 0$  represents a flat Universe, while  $k = -1$  an open one. The Universe is described by the FLRW metric with both expansion and contraction captured by the scale factor  $a(t)$ . One then needs to find an equation for  $a(t)$  taking in account the matter and energy densities, encoded in  $T_{\mu\nu}$ .

The Universe is filled with different matter components. Matter and energy sources can be represented via perfect fluids i.e. fluids with no shear stresses, viscosity, or heat conduction. They are characterized by pressure  $P(t)$  and density  $\rho(t)$  linked by an equation of state. In particular, the non relativistic matter, called dust, has  $P = 0$  and the relativistic gas, or radiation, has  $P = 1/3\rho$ . Summarizing, the equation of state looks like

$$P = w\rho, \quad (2.3)$$

with  $w = 0$  for dust and  $w = 1/3$  for radiation.

As the Universe expands, one expects the energy density to decrease. The way in which this happens is described by energy conservation, i.e. the continuity equation, which can be written in a simple way as

$$\dot{\rho} + 3H(\rho + P) = 0, \quad (2.4)$$

where  $\dot{\rho}$  denotes the derivative with respect to time of the density, and  $H$  is the Hubble parameter describing the expansion of the Universe. It is related to the scale factor according

$$H = \frac{\dot{a}(t)}{a(t)}, \quad (2.5)$$

where  $\dot{a}(t)$  is the time derivative of the scale factor. The value of the Hubble parameter depends on time; its value nowadays is [1]

$$H_0 = (67.36 \pm 0.54) \text{ km} \cdot \text{s}^{-1} \cdot \text{Mpc}^{-1}. \quad (2.6)$$

Usually one considers the dimensionless parameter  $h = (0.6736 \pm 0.0054)$ , defined as  $h \equiv H_0/(100 \text{ km} \cdot \text{s}^{-1} \cdot \text{Mpc}^{-1})$ . Substituting eq. (2.3) in eq. (2.4), one can obtain the dependence of the fluid components as a function of the scale factor

$$\frac{\dot{\rho}}{\rho} = -3(1+w)\frac{\dot{a}}{a}, \quad (2.7)$$

and performing an integration on it, we have

$$\rho(t) \propto a^{-3(w+1)}. \quad (2.8)$$

This becomes

- matter:  $\rho_{\text{m}} \propto a^{-3}$
- radiation:  $\rho_{\text{r}} \propto a^{-4}$

For the former, the behaviour of  $\rho$  simply reflect the expansion of the volume  $V \propto a^3$ ; we will see that actually in the Universe two components for the matter are required to explain the experimental data:

- dark matter represents most of the matter in the Universe in the form of invisible matter;
- baryonic matter which is the ordinary matter.

The radiation is a gas of relativistic particles, i.e. the energy density is dominated by the kinetic energy. Radiation is composed for instance by photons, always relativistic because massless. Actually, at high temperatures as  $T \gtrsim 200 \text{ GeV}$  all the particle content of the Standard Model is relativistic.

However, matter and radiation are not enough to describe the evolution of the Universe. Instead, the Universe today seems to be dominated by a component having a negative pressure  $P = -\rho$ , i.e.  $w = -1$ . Usually this component is called vacuum energy or cosmological constant and its density evolution, according to eq. (2.7), is

$$\rho \propto a^0. \quad (2.9)$$

The last step in our discussion is the understanding of how a perfect fluid affects the expansion of the Universe. We need to come back to the Einstein's equations, eq. (2.1), and explicit the energy-momentum tensor in the perfect fluid approximation. In this case it takes the following simple form

$$T_{\mu\nu} = \text{diag}(\rho, -P, -P, -P), \quad (2.10)$$

because we do not have nor heat conduction neither viscosity working in the perfect fluid approximation and all the components of  $T_{\mu\nu}$  which are not diagonal vanish. The dynamics is described by solving the Einstein's equations with the FLRW metric, eq. (2.2), and considering the energy momentum tensor as in eq. (2.10). The solutions are known as Friedmann equations:

$$\dot{a}^2 + k = \frac{8}{3}\pi G\rho a^2, \quad (2.11)$$

for the  $T^{00}$ ; for  $T^{ii}$  one has

$$\ddot{a} = -\frac{4}{3}(\rho + 3P)a. \quad (2.12)$$

The first equation, eq. (2.11), has the following solution

$$H^2(t) + \frac{k}{a^2(t)} = \rho(t)\frac{8\pi G}{3}, \quad (2.13)$$

which is useful to define the critical density as

$$\rho_c = \frac{3H^2(t)}{8\pi G}, \quad (2.14)$$

and which separates an expanding Universe from a collapsing one, having assumed  $\Lambda = 0$ . It is convenient to define the dimensionless quantity

$$\Omega(t) = \frac{\rho(t)}{\rho_c(t)}. \quad (2.15)$$

Using the solution in eq. (2.13) together with the above definition, and solving for the curvature  $k$ , one obtains that the curvature is determined by the time-dependent total energy density of the Universe according to

$$k = H^2(t)a^2(t)(\Omega(t) - 1). \quad (2.16)$$

One can have

- $\Omega > 1$ :  $k > 0$  and the Universe is closed;
- $\Omega < 1$ :  $k < 0$  and the Universe is opened;
- $\Omega = 1$ :  $k = 0$  and the Universe is flat.

From experiments, we know that our Universe is flat, i.e.  $\Omega = 1$ . This means that

$$\Omega = \frac{\rho_m + \rho_r + \rho_\Lambda}{\rho_c} = 1. \quad (2.17)$$

Hitherto we have described the Universe in terms of the scale factor  $a(t)$  and  $\rho(t)$  obeying the Friedmann equations; what we want now is to describe its evolution using the time variable. We use the power law ansatz  $a(t) \propto t^\beta$  in the Friedmann eq. (2.12), obtaining for different components of the total density

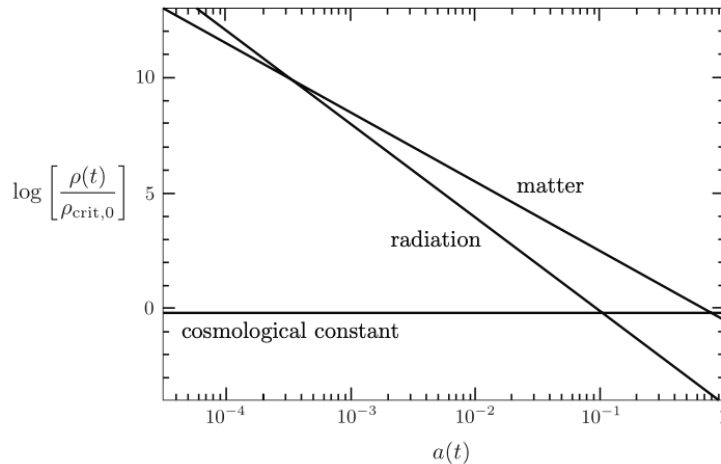


Figure 2.1: Composition of the Universe as a function of the scale factor  $a(t)$ . The figure is taken from [16].

- non relativistic matter:  $a(t) \propto t^{2/3}$ ;
- relativistic radiation:  $a(t) \propto t^{1/2}$ ;
- vacuum energy:  $a(t) \propto e^{\sqrt{\Lambda(t)/3}t}$ .

Looking at the composition of the Universe in terms of relativistic states, non-relativistic and cosmological constant, one notices that at large temperatures the Universe is dominated by relativistic states. When it starts to expand and  $a(t)$  increases, the relativistic energy drops like  $1/a^4$  while non relativistic energy drops like  $1/a^3$ : this means that as long as the relativistic energy density dominates, the relative fraction of matter increases linearly in  $a$ . The time at which both the radiation and the matter contributed with the same amount of density to the total density is known as matter-radiation equality. Being  $\Lambda$  in general constant, its contribution never changed and it starts to dominate now. This evolution is shown in fig. 2.1. One can conclude that there are 3 different epochs for the Universe: radiation dominated era in which the expansion was mostly dictated by the radiation. This era finished at the matter-radiation equality time, after which matter started to dominate. Nowadays the Universe expansion is determined mostly by the cosmological constant  $\Lambda$ .

Our next goal is the introduction of the main concepts regarding the thermal history of Universe.

## 2.2 Thermal History

After Inflation the Universe was hot and dense and the thermodynamical properties were determined by chemical and kinetic equilibrium, being all the species in a thermal bath. This is confirmed by the perfect blackbody spectrum of the CMB, which can be produced only by an isothermal, opaque and non-reflecting object.

However, as we know, the history of the Universe is a history of cooling: during its expansion, non equilibrium dynamics took place and different key events such as Electroweak (EW) and Quantum chromodynamics (QCD) phase transitions, freeze-out of different species and Big Bang Nucleosynthesis (BBN) happened.

The key point to understand the thermal history of the Universe is the comparison between the rate of interaction  $\Gamma$  of the species in equilibrium and the rate of expansion  $H$  of the Universe. The rate of interaction is described via

$$\Gamma = n\sigma v, \quad (2.18)$$

where  $\sigma$  is the interaction cross section,  $v$  is the average velocity and  $n$  is the number density of the particles. Comparing  $\Gamma$  and  $H$ , 3 different scenarios are possible:

- $\Gamma \gg H$ : local equilibrium is reached before the expansion becomes relevant;
- $\Gamma \simeq H$ : particles decouple from thermal bath;
- $\Gamma \ll H$ : expansion is dominating.

### 2.2.1 Early Universe

The right framework to describe the thermal equilibrium is Statistical Mechanics. The better choice is the description of particles in phase space, given by particle momenta and positions. To obtain the number density of particles, it is useful to define the distribution function  $f(\vec{x}, \vec{p}, t)$  which tells how particles are distributed over the momentum eigenstates. According to the cosmological principle,  $f = f(\vec{p}, t)$ , because of homogeneity, and  $f(|\vec{p}|)$  because of isotropy. The particle density in phase space is the density of states multiplied by the distribution function,  $g/(2\pi)^3 \cdot f(p)$ , hence the number density of particles is

$$n = \frac{g}{(2\pi)^3} \int d^3p f(p), \quad (2.19)$$

where  $g$  is the number of internal degree of freedom. Assuming

$$E(p) = \sqrt{p^2 + m^2}, \quad (2.20)$$

it is a good approximation for weakly interacting particles of the gas, i.e. they are almost free and their interactions are negligible. The energy density is then defined as

$$\rho = \frac{g}{(2\pi)^3} \int d^3p f(p) E(p). \quad (2.21)$$

Analogously for the pressure one has

$$P = \frac{g}{(2\pi)^3} \int d^3p f(p) \frac{p^2}{3E}. \quad (2.22)$$

The equilibrium is characterized by the state of maximum entropy in which the distribution functions are given by Fermi-Dirac and Bose-Einstein distributions; the former describes the collective behaviour of fermions while the second describes bosons. These distribution functions are

$$f(p) = \frac{1}{e^{(E(p)-\mu)/T} \pm 1}, \quad (2.23)$$

where the "+" is for fermions and "-" for bosons;  $\mu$  represents the chemical potential and  $T$  is the temperature. In the early Universe the chemical potential is very small and can be neglected in first approximation. This happens because if we have an equilibrium condition as

$$1 + 2 \rightleftharpoons 3 + 4, \quad (2.24)$$

it is reflected on chemical potentials as

$$\mu_1 + \mu_2 \rightleftharpoons \mu_3 + \mu_4. \quad (2.25)$$

It can be shown that  $\mu_i$  is related to the difference of number densities of particles and antiparticles  $\mu_i \propto n_i - \bar{n}_i$  present in the thermal bath and this difference is very small. It can not be zero because asymmetry is required to have the Universe we observe today.

Substituting eq. (2.23) in eqs. (2.19) and (2.21) and using  $x = m/T$  and  $\xi = p/T$  one gets

$$n = \frac{g}{2\pi^2} T^3 \int_0^\infty \frac{\xi^2}{\exp(\sqrt{\xi^2 + x^2} \pm 1)} d\xi, \quad (2.26)$$

$$\rho = \frac{g}{2\pi^2} T^4 \int_0^\infty \frac{\xi^2 \sqrt{\xi^2 + x^2}}{\exp(\sqrt{\xi^2 + x^2} \pm 1)} d\xi. \quad (2.27)$$

$$P = \frac{g}{6\pi^2} T^4 \int_0^\infty \frac{\xi^4}{(\exp(\sqrt{\xi^2 + x^2} \pm 1)) \sqrt{\xi^2 + x^2}} d\xi. \quad (2.28)$$

It is convenient to study two different limits of the expressions above: the case of relativistic particles, with  $m \ll T$ , and the case of non relativistic particles, with  $m \gg T$ .

- For the relativistic case one gets

$$n = \begin{cases} \frac{\zeta(3)}{\pi^2} g T^3 & \text{bosons,} \\ \frac{3}{4} \frac{\zeta(3)}{\pi^2} g T^3 & \text{fermions,} \end{cases} \quad (2.29)$$

$$\rho = \begin{cases} \frac{\pi^2}{30} g T^4 & \text{bosons,} \\ \frac{7}{8} \frac{\pi^2}{30} g T^4 & \text{fermions,} \end{cases} \quad (2.30)$$

$$P = \frac{\rho}{3}. \quad (2.31)$$

- For non-relativistic case

$$n = g \left( \frac{mT}{2\pi} \right) e^{-m/T}, \quad (2.32)$$

$$\rho \simeq mn. \quad (2.33)$$

Notice that in the case characterized by  $T \ll m$ , the exponential suppression comes from the distribution function in eq. (2.23): massive particles are exponentially rare at low temperatures. Moreover, the energy density  $\rho$  is simply equal to the mass density. For what concerns the pressure  $P$ , a non relativistic gas of particles acts like pressureless dust as anticipated in eq. (2.3), being  $P = nT \ll \rho$ . Summarizing, in the non relativistic limit, the number density, energy density and pressure of particles are Boltzmann suppressed when the temperature drops below the mass of the particle. This fact can be interpreted as particle-antiparticle annihilation; at high energies, when  $T \gg m$ , annihilations occur as well but they are compensated by production mechanisms. At low temperatures, the thermal particles energies are not sufficient for pair production and the particle decouple from the thermal bath and freeze-out.

It is useful to define the effective number of degrees of freedom  $g_*$  which is a function of the temperature. Starting with the radiation case, the total radiation density is the sum over the energy densities of all relativistic species

$$\rho_r = \sum_i \rho_i = \frac{\pi^2}{30} g_*(T) T^4, \quad (2.34)$$

where  $g_*$  is the effective number of relativistic degrees of freedom with a fixed temperature  $T$ . We need to consider separately two cases, when relativistic species are in thermal equilibrium (i) and when they are decoupled from thermal bath (ii).

## 2.2. THERMAL HISTORY

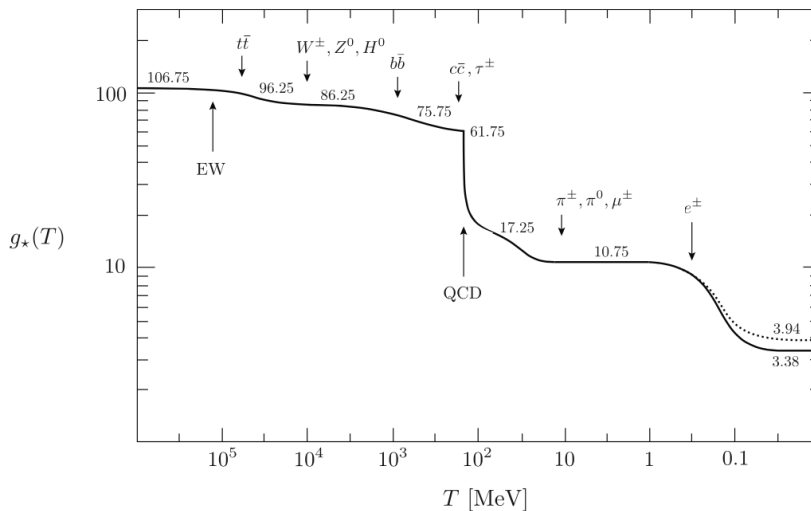


Figure 2.2: Evolution of the relativistic degrees of freedom  $g_*$  considering only the Standard Model particle content. The maximum value corresponds to the condition when all the particles are relativistic while the minimum corresponds to today's value, which is 3.6. The figure is taken from [16].

- For relativistic species in thermal equilibrium with  $T_i = T \gg m_i$  the effective number of degrees of freedom can be expressed as

$$g_*^{th}(T) = \sum_{i=\text{bosons}} g_i + \frac{7}{8} \sum_{i=\text{fermions}} g_i. \quad (2.35)$$

When the temperature  $T$  drops below the mass  $m_i$ , the specie becomes non relativistic and decouples from the thermal bath. As a consequence, its degrees of freedom are removed from eq. 2.35. Superscript "th" stays for thermal (equilibrium).

- For relativistic species which are not in thermal equilibrium with  $T_i \neq T \gg m_i$ ,  $g_*$  is

$$g_*^{dec}(T) = \sum_{i=\text{bosons}} g_i \left(\frac{T_i}{T}\right)^4 + \frac{7}{8} \sum_{i=\text{fermions}} g_i \left(\frac{T_i}{T}\right)^4; \quad (2.36)$$

the superscript "dec" stays for decoupled, to underline that considered species are not in thermal equilibrium.

Figure 2.2 shows the evolution of  $g_*$  as a function of the temperature  $T$ . At  $T \gtrsim 175$  GeV (top quark mass) all particles of the Standard Model are relativistic: from eq. (2.35) one has

- $g_{\text{bosons}} = 2 \cdot 1_\gamma + 3 \cdot 3_{W^\pm, Z} + 2 \cdot 8_g + 1_H = 28$ ,
- $g_{\text{fermions}} = 12 \cdot 6_q + 4 \cdot 3_l + 2 \cdot 3_\nu = 90$ .

$g_\star$  then is

$$g_\star = g_{\text{bosons}} + \frac{7}{8}g_{\text{fermions}} = 106.75. \quad (2.37)$$

As the temperature drops, various particle species become non-relativistic and further on decouple. Being most massive in Standard Model particle content, top quarks become non-relativistic first and the number of effective degrees of freedom reduced to 96.25. The Higgs boson and the electroweak gauge bosons become non relativistic next and the  $g_\star$  dropped to 86.25. Next, bottom and charm quarks as well as tau lepton and  $g_\star$  reduced to 61.76. Following the solid line in fig. 2.2, notice that at  $T \simeq 250$  MeV, the QCD phase transition happened and quarks form bound states known as baryon and mesons. As the temperature decreased, other species become non-relativistic and only left are pions, electrons, muons, neutrinos and photons, all contributing to  $g_\star = 17.25$ .

To describe the evolution of the Universe it is useful to introduce a conserved quantity. This quantity is the entropy being the expansion of the Universe, to a good approximation, adiabatic.

## 2.2.2 Entropy conservation

Considering the second law of thermodynamics

$$TdS = dU + PdV, \quad (2.38)$$

with  $U = \rho V$ , one has

$$\begin{aligned} dS &= \frac{1}{T} (d[(\rho + P)V] - VdP), \\ &= d \left[ \frac{\rho + P}{T} V \right]. \end{aligned} \quad (2.39)$$

It is convenient to define the entropy density  $s = S/V$ , and using eq. (2.21) one has

$$s = \sum_i \frac{\rho_i + P_i}{T_i} = \frac{2\pi^2}{45} g_{\star S}(T) T^3, \quad (2.40)$$

where  $g_{\star S}$  is the effective number of degrees of freedom in entropy i.e.

$$g_{\star S}(T) = g_{\star S}^{\text{th}}(T) + g_{\star S}^{\text{dec}}(T). \quad (2.41)$$

In particular one has

- for species in thermal equilibrium

$$g_{\star S}^{th}(T) = \sum_{i=\text{boson}} g_i + \frac{7}{8} \sum_{i=\text{fermion}} g_i = g_{\star}(T), \quad (2.42)$$

- for decoupled species one gets

$$g_{\star S}^{dec}(T) = \sum_{i=\text{boson}} g_i \left(\frac{T_i}{T}\right)^3 + \frac{7}{8} \sum_{i=\text{fermion}} g_i \left(\frac{T_i}{T}\right)^3 \neq g_{\star}^{dec}(T). \quad (2.43)$$

The conservation of entropy has an important implication. Considering the relation eq. (2.40), the conserved entropy is

$$S = sV \propto sa^3 \propto g_{\star S}(T)T^3 a^3. \quad (2.44)$$

Inverting the latter relation one obtains

$$T \propto g_{\star S}^{-1/3} a^{-1}. \quad (2.45)$$

When a particle species becomes non relativistic and decouples from the thermal bath, its entropy is transferred to the other particles that are still in equilibrium in the thermal bath. As a consequence, the temperature  $T$  of the thermal bath increases while  $g_{\star S}$  decreases.

### 2.2.3 Departure from Equilibrium

The tool to describe the departure from equilibrium, such as decoupling from the thermal bath, is the Boltzmann equation.

Let's analyze the moment of the decoupling. We consider a certain species with number density of particles  $n_i$  and such that are not interacting. The number of particles per comoving volume is then a constant

$$\frac{dN}{dt} = \frac{d(n_i a^3)}{dt} = 0 \rightarrow \frac{dn_i}{dt} + 3Hn_i = 0. \quad (2.46)$$

To include interactions, one adds a collision term

$$\frac{1}{a^3} \frac{d(n_i a^3)}{dt} = C_i[\{n_j\}], \quad (2.47)$$

where the right-hand side represents the collision term which depends on the specific interactions. The eq. (2.47) is called the Boltzmann equation.

Let's consider as an example the following process



i.e. 1 and 2 annihilating in 3 and 4 and vice versa. Pointing the attention on  $n_1$ , the rate of change in the abundance of species 1 is given by the competition of rates for production and the one of annihilation. In other words, we have

$$\frac{1}{a^3} \frac{d(n_1 a^3)}{dt} = -\langle \sigma v \rangle \left[ n_1 n_1 - \left( \frac{n_1 n_2}{n_3 n_4} \right)_{\text{eq}} n_3 n_4 \right]. \quad (2.49)$$

where  $\langle \sigma v \rangle$  is the thermally averaged cross. This expression has two contributions: looking at the right hand side of the equation, the term with "+" sign represents the production of particles, while the term with "-" sign denotes the annihilation process. In terms of number of particles in a comoving volume, eq. (2.49) can be written as

$$\frac{d \ln N_1}{d \ln a} = -\frac{\Gamma_1}{H} \left[ 1 - \left( \frac{N_1 N_2}{N_3 N_4} \right)_{\text{eq}} \frac{N_3 N_4}{N_1 N_2} \right], \quad (2.50)$$

with  $\Gamma_1 = n_2 \langle \sigma v \rangle$ . The right-hand side of eq. (2.50) contains two crucial factors: outside the brackets we have the interaction efficiency while inside the brackets the deviation from equilibrium.

If  $\Gamma_1 \gg H$  the system is described by equilibrium. Indeed, if  $N_1 \gg N_1^{\text{eq}}$  then the right-hand side of the equation is negative and push the  $N_1$  to its equilibrium value. In case of  $N_1 \ll N_1^{\text{eq}}$  the right-hand side of eq. (2.50) is positive and the production of  $N_1$  is pushed up to its equilibrium value.

When  $\Gamma_1 < H$ , the right-hand side is suppressed and the comoving density is a constant. Both cases are represented in fig. 2.3.

A simple case is when  $n_1 = n_2$  and  $n_3 = n_4$ , that can describe massive dark matter freeze-out. We will largely study the dark matter properties in next chapters; for the moment, it is enough to know that dark matter is constituted by massive non baryonic matter.

In the early Universe, dark matter particles were in equilibrium with the thermal bath, cosmic plasma at high temperatures but then experienced freeze-out at a critical temperature  $T_f$ . Solving the Boltzmann equation eq. (2.50) it is possible to determine the epoch of freeze-out and its relic density.

The assumption we need to do is that in the early Universe, heavy dark matter particles  $\chi$  and antiparticles  $\bar{\chi}$  can annihilate to produce two very light particles  $l$  and  $\bar{l}$  according to



Moreover, we assume that the light particles are tightly coupled to the thermal bath i.e. they maintain their equilibrium with thermal bath and their densities are  $n_l = n_l^{\text{eq}}$ .

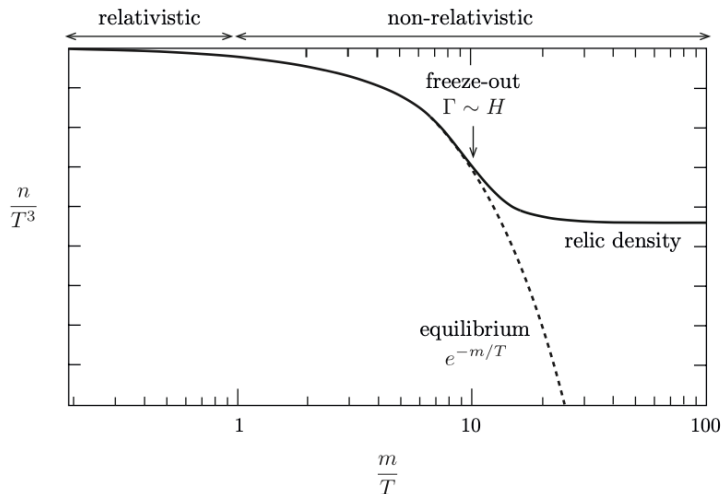


Figure 2.3: Schematic representation of particle freeze-out. When  $T \gg m$  the particles are in equilibrium with the thermal bath. When the temperature decreases reaching the condition  $T \ll m$ , the particles freeze out and give rise to a constant density (relic density) that is larger than the equilibrium abundance suppressed by the Boltzmann factor. Indeed, if a massive particle species remained in thermal equilibrium until the present, its abundance would be absolutely negligible. The figure is taken from [16].

Finally, we assume that there is no initial asymmetry between dark matter particles and antiparticles.

The Boltzmann eq. (2.49) then reduces to

$$\frac{dN_\chi}{dt} = -s\langle\sigma v\rangle [N_\chi^2 - (N_\chi^{\text{eq}})^2], \quad (2.52)$$

considering the evolution of the number of dark matter particles in a comoving volume  $N_\chi = n_\chi/s$ . We are interested to study the dynamics at  $T \simeq m_\chi$ ; it is convenient to define a new measure of time:

$$x = \frac{m_\chi}{T}. \quad (2.53)$$

To write the Boltzmann equation in terms of  $x$  rather than  $t$ , notice that

$$\frac{dx}{dt} = \frac{d}{dt} \left( \frac{m_\chi}{T} \right) = -\frac{1}{T} \frac{dT}{dt} x \simeq Hx, \quad (2.54)$$

considering that  $T \propto a^{-1}$  for times relevant for freeze-out. Assuming that radiation dominates, so  $H = H(m_\chi)/x^2$ , one can define  $\lambda$  as

$$\lambda = \frac{2\pi^2}{45} g_* s \frac{m_\chi^3 \langle\sigma v\rangle}{H(m_\chi)}; \quad (2.55)$$

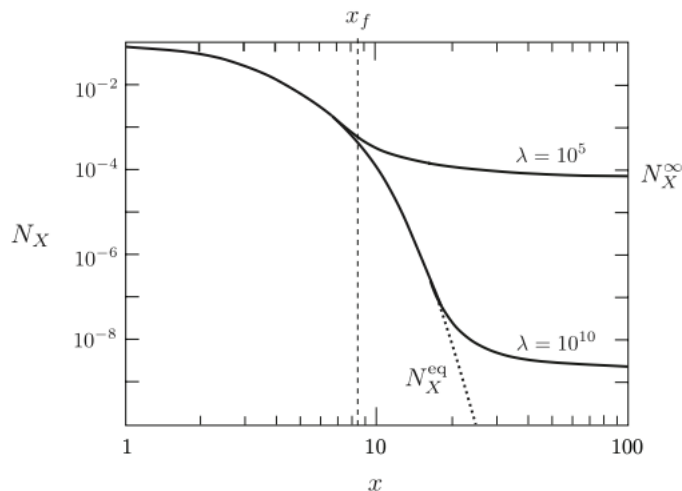


Figure 2.4: Numerical solutions for dark matter particles abundance as a function of  $x = m_\chi/T$ . There are represented two different values of  $\lambda$  which represents the interaction rate and determines the today dark matter particles abundance. Being proportional to the inverse of  $\lambda$ , as interaction rate increases,  $N_\chi^\infty$  decreases. The figure is taken from [16].

With eq. (2.55), the eq. (2.52) becomes the so-called Riccati equation

$$\frac{dN_\chi}{dx} = -\frac{\lambda}{x^2} [N_\chi^2 - (N_\chi^{\text{eq}})^2]. \quad (2.56)$$

A good approximation is that  $\lambda$  in eq. (2.55) is a constant but the equation does not have an analytic solution. In fig. 2.4 are shown the results of the numerical solutions for eq. (2.56). For very high values of temperature,  $x < 1$ , one has  $N_\chi = N_\chi^{\text{eq}} \simeq 1$ . At low temperatures,  $x \gg 1$  and the equilibrium becomes exponentially suppressed with  $N_\chi \simeq e^{-x}$ . Numerically it is found that the freeze-out happens at  $x_f \simeq 10$ . At this point the number of particles deviate from equilibrium. The final relic abundance, namely  $N_\chi^\infty$ , determines the freeze-out density of dark matter. Considering that at freeze-out  $N_\chi^\infty \gg N_\chi^{\text{eq}}$ ,  $N_\chi^{\text{eq}}$  can be dropped in eq. (2.56)

$$\frac{dN_\chi}{dx} \simeq -\frac{\lambda N_\chi^2}{x^2}, \quad (2.57)$$

where  $x > x_f$ . Integrating from  $x_f$  to  $x = \infty$ , one finds

$$\frac{1}{N_\chi^\infty} - \frac{1}{N_\chi(x_f)} = \frac{\lambda}{x_f}. \quad (2.58)$$

Usually,  $N_\chi^\infty \ll N_\chi(x_f)$  and a simple analytic approximated solution is

$$N_\chi^\infty \simeq \frac{x_f}{\lambda}. \quad (2.59)$$

This means that the abundance of number of particles depends on unknown freeze-out time  $x_f$ , estimated  $x_f \simeq 10$  and decreases as the interaction rate  $\lambda$  increases. In other words, larger interactions maintain equilibrium longer and vice-versa. For small values of  $\lambda$  the abundance of particles is bigger than for high values of  $\lambda$ , as one verifies in fig. 2.4.

## 2.3 Structure formation

Hitherto we have said that at large scales the Universe is homogeneous and isotropic according to the cosmological principle and this statement is confirmed by measurement of the CMB radiation and by redshift surveys.

However, on small scales the Universe appears lumpy: the density of galaxies is about  $10^5$  times the average density of the Universe and the one of cluster of galaxies is near  $10^2 - 10^3$  the average density of the Universe. These structures can be explained considering small primordial inhomogeneities of density. In other words the homogeneous and isotropic Universe was disturbed by tiny gravitational wells. These have been amplified to produce the galaxies, galaxy groups and super-clusters we observe today.

The leading theory for the origin of these perturbation is based on quantum fluctuations of the inflaton field, responsible for the exponential expansion of our Universe after the Big Bang. As we will see, the evolution of the primordial over-densities during the expansion of the Universe gives us information about the dark matter density and its properties.

In general, a density perturbation is defined as

$$\delta = \frac{\delta\rho}{\rho} = \frac{\rho - \bar{\rho}}{\bar{\rho}}, \quad (2.60)$$

where  $\bar{\rho}$  is the average density. These perturbations are of the order  $\delta \simeq 10^2$  nowadays and we need to explain how they evolved to reach such values from an almost smooth condition in early Universe. The idea is to treat the problem from a Newtonian point of view, studying the evolution of the matter density in the presence of a gravitational field.

The matter density  $\rho$  with velocity  $\mathbf{u}$  and its gravitational potential  $\phi$  satisfy the following equations

$$\frac{\partial\rho}{\partial t} + \nabla \cdot (\rho\mathbf{u}) = 0 \quad \text{continuity equation,} \quad (2.61)$$

$$\left( \frac{\partial}{\partial t} + \mathbf{u} \cdot \nabla \right) \mathbf{u} = -\frac{1}{\rho} \nabla P - \nabla\phi \quad \text{Euler equation,} \quad (2.62)$$

$$\nabla^2\phi = 4\pi G_N\rho \quad \text{Poisson equation,} \quad (2.63)$$

### 2.3. STRUCTURE FORMATION

---

The set of eqs. (2.61) to (2.63) can be solved considering a homogeneously expanding fluid; here we denote with subscript "0" quantities without perturbations for later convenience

$$\rho_0 = \rho_0(t_0) \left(\frac{a_0}{a}\right)^2, \quad \mathbf{u}_0 = \frac{\dot{a}}{a} \mathbf{r} = H \mathbf{r}, \quad \phi = \frac{4\pi G_N \rho_0}{3} \mathbf{r}^2, \quad \nabla P_0 = 0. \quad (2.64)$$

Now the idea is to add small perturbations to the quantities defined above

$$\rho = \rho_0 + \delta_\rho, \quad \mathbf{u} = \mathbf{u}_0 + \delta_\mathbf{u}, \quad \phi = \phi + \delta_\phi, \quad P = P_0 + \delta_P. \quad (2.65)$$

Substituting in eqs. (2.61) to (2.63) the assumptions in eq. (2.65), keeping only the first orders and defining co-moving coordinates, one obtains a second order differential equation for the density fluctuations  $\delta$ . By taking the Fourier transform of  $\delta(t, \mathbf{x})$  to  $\delta(t, \mathbf{k}) = \delta$ , one obtains

$$\ddot{\delta} + 2H\dot{\delta} - \left(\frac{c_s^2 k^2}{a^2} - 4\pi G_N \rho_0\right) \delta = 0, \quad (2.66)$$

where  $c_s$  is the speed of sound. Basically one can interpret the term in brackets as the competition of two processes: gravitational compression and a pressure resisting this compression.

Equation (2.66) is called the Jeans equation. It is then possible to define the constant Jeans wave number

$$k_J = \frac{4\pi G_N \rho_0 a^2}{c_s^2}, \quad (2.67)$$

the corresponding Jeans length (2.67)

$$\lambda_J = \frac{2\pi}{k_J}, \quad (2.68)$$

and the Jeans mass

$$M_J = \rho \lambda_J^3. \quad (2.69)$$

The Jeans mass is the mass contained on a sphere of radius equal to the Jeans length. Equation (2.66) with eq. (2.67) becomes

$$\ddot{\delta} + 2H\dot{\delta} + 4\pi G_N \rho_0 \left(\frac{k^2}{k_J^2} - 1\right) \delta = 0. \quad (2.70)$$

Equation (2.70) can be solved in three special regimes:

- when  $k \gg k_J$ , eq. (2.70) becomes

$$\ddot{\delta} + 2H\dot{\delta} + \frac{c_s^2 k^2}{a^2} \delta = 0, \quad (2.71)$$

corresponding to the equation of a damped harmonic oscillator with solution  $\delta \propto e^{\pm i\omega t}$  with  $\omega = c_s k/a$ . This means that the solutions are oscillating with decreasing amplitude due to the Hubble friction term  $2H\dot{\delta}$ . One concludes that structures with  $k \ll k_J$  do not grow and can not explain large structures we observe today.

- For  $k \ll k_J$ , eq. (2.70), eq. (2.70) becomes

$$\ddot{\delta} + 2H\dot{\delta} - 4\pi G_N \rho_0 \delta = 0. \quad (2.72)$$

Recalling that  $a \propto t^{2/3}$  for non relativistic matter according to eq. (2.1), one obtains

$$\ddot{\delta} + \frac{4}{3t}\dot{\delta} - \frac{2}{3t^2}\delta = 0, \quad (2.73)$$

which solution is  $\delta \propto t^{2/3}$ . Notice that in this case, in a matter dominated epoch, the perturbations can grow, differently from the first case. However, using the outcome of numerical simulations one finds that the cosmic structure observed today can not be explained by the photon-baryon fluid alone.

If one considers the radiation epoch, eq. (2.72) reduces to

$$\ddot{\delta} + \frac{1}{t}\dot{\delta} = 0, \quad (2.74)$$

because the evolution is  $a \propto t^{1/2}$ , as shown in eq. (2.1). The solution of the above equation is

$$\delta \propto A + B \log(t) \quad (2.75)$$

In this case the the growth of density perturbations is much weaker than for non-relativistic matter due to the presence of  $\log(t)$ .

- when  $k \ll a/a_0 H$  corresponding to perturbations larger than Hubble scale; the Newtonian treatment is not longer possible and from General Relativity one finds the following scaling

$$\delta = \left(\frac{a}{a_0}\right)^2 \delta_0. \quad (2.76)$$

The growth is a function of the scale parameter for non-relativistic and relativistic matter. This equation predicts the formation of large structures starting with relativistic matter. On the other hands, radiation pressure in the photon-baryon fluid prevents the growth of small baryonic structures but small baryon-acoustic oscillations, as those predicted by  $k \gg k_J$  case, can be observed. Large structures in the radiation dominated epoch expand rapidly and non relativistic structures can explain the matter density measured at the CMB epoch with numerical simulations. However, it is necessary to consider an additional component for the matter.

This additional component is usually called dark matter. Its only properties that we can derive from this discussion is that it should contribute to the gravitational potential so it has to be massive, it has to be non relativistic and its pressure should be zero. The necessity for dark matter comes not only as an explanation of structure formation: in the next section we will illustrate other observable evidences.

## 2.4 Dark matter evidences

There are many astrophysical evidences for the dark matter existence. As we have seen in previous section, it is required for the correct reproduction of structure formations. In this section we will present other interesting motivation for dark matter.

### 2.4.1 Rotation curves of galaxies

The study of rotation curves has played a very important role in the evidence for dark matter. The rotation curve of a galaxy represents the evolution of the radial velocity  $v(r)$  of stars with respect to their distance from the galactic centre. The gravitational potential  $\phi(r)$  can be related to the matter density  $\rho(r)$  through the Poisson equation, assuming a spherical mass distribution inside the galaxy:

$$\nabla^2 \phi = 4\pi G_N \rho. \quad (2.77)$$

One can therefore deduce the expression of the radial velocity at a distance  $r$  from the centre

$$v(r) = \sqrt{\frac{G_N M(r)}{r}}, \quad (2.78)$$

where  $M(r)$  is the mass contained inside a sphere of radius  $r$  with density  $\rho$

$$M(r) = \int_0^r \rho(r') d^3 r'. \quad (2.79)$$

Assuming that almost all the mass of a galaxy is concentrated in a sphere of radius  $R$  defining its central core, one can write that  $M(r \gg R) \simeq M(R)$  and therefore one should expect a velocity decreasing with  $r$  according to

$$v(r \gg R) = \sqrt{\frac{G_N M(R)}{r}} \propto \frac{1}{\sqrt{r}}. \quad (2.80)$$

One of the first physicists to investigate rotation curves of galaxies was Horace Babcock. In 1939 he presented the measurement of the rotation curve of the M31 galaxy (i.e. the Andromeda galaxy) realising that radial velocities were not decreasing on large radii as expected. Moreover, he raised the problem that rotation curves tend to flatten on large

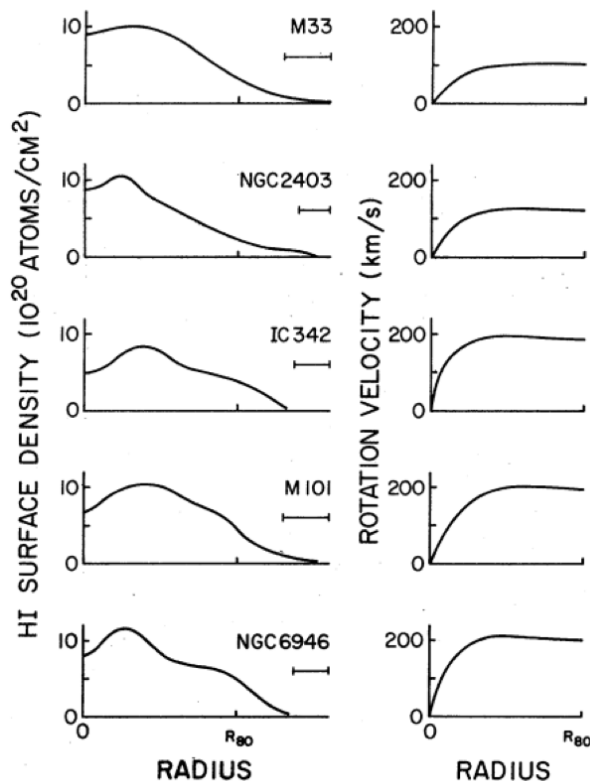


Figure 2.5: Hydrogen surface density profile (left) and the rotation curves (right) of five galaxies as obtained by Rogstad and Shostak in 1972. The bars under the galaxy names indicate the average radial beam diameter, i.e. the effective spatial resolution.  $R_{80}$  is the radius containing 80% of the observed HI. The figure is taken from [19].

radii, whose explanation can be attributed to the existence of a dark matter halo. To explain the flat behaviour of the velocity at large distances, the shape of the dark matter density profile should satisfy  $M(r) \propto r$  and moreover, because of eq. (2.79),  $\rho \propto r^{-2}$  at large  $r$ .

To measure the velocity distribution  $v(r)$  different techniques can be used. One of this method is the measurement of the 21 cm line of neutral hydrogen. It was discovered in 1951 by H. Ewen and E. Purcell and was suggested as a new way of observing the Universe and in particular, to measure rotation curves because of its low level of absorption in the interstellar medium. Figure 2.5 illustrates the results obtained from the analysis done by D. Rogstad and G. Shostak [18], more specifically the rotation curves of 5 different galaxies - M33, NGC 2403, IC 342, M101, NGC 6949 - obtained using the radio telescope at the Owens Valley Radio Observatory. They found that these rotation curves remain flat out to the largest radii observed, in contrast with eq. (4.16).

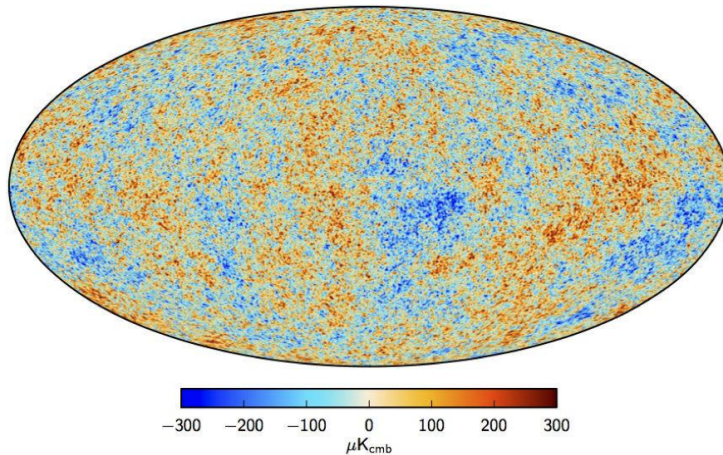


Figure 2.6: CMB temperature anisotropy map as measured by the Planck collaborations. The figure is taken from [21].

### 2.4.2 The Cosmic Microwave Background

The observation of the CMB is undoubtedly one of the strongest evidence of the presence of dark matter in our Universe. At the temperature around 1 eV the thermal photons have decoupled from the matter and, since then, they have been streaming freely in every direction in the Universe. These CMB photons are coming from the sphere's surface of last scattering, which has the observer in the centre. The temperature of the CMB photons has dropped with the expansion and the cooling of the Universe to the current measured value of  $T_{\text{CMB}} = 2.72548 \pm 0.00057 \text{ K}$  [20]. The CMB was detected accidentally on Earth for the first time by Penzias and Wilson in 1964, for which they got the Nobel prize. The CMB can be accurately described today by a black body spectrum and can be considered almost isotropic, when one subtracts the dipole effect responsible for anisotropies. Dipole effect indeed arises once one takes in account that the Solar system moves within our galaxy and the photons arriving on the Earth are then redshifted and blueshifted due to Doppler effect. After removing the dipole effect and some other astrophysical contributions, the CMB anisotropies on the surface of last scattering are of order  $\delta T/T \simeq 10^{-5}$ . Figure 2.6 shows the map of anisotropies measured by the Planck satellite [21]. Anisotropies can be explained by considering a non uniform matter distribution at the time of recombination i.e. formation of first atoms happened around  $T = 1 \text{ eV}$ .

The best way of analysing temperature anisotropies is to decompose the fluctuations into spherical harmonics considering angles  $\theta$  and  $\phi$  on the sphere of last scattering

$$\frac{\delta T(\theta, \phi)}{T_0} = \frac{T(\theta, \phi) - T_0}{T_0} = \sum_{l=0}^{\infty} \sum_{m=-l}^l a_{lm} Y_{lm}(\theta, \phi). \quad (2.81)$$

Assuming that the value of peak,  $T_0$ , is known, we want to find the width of peak. This can be done computing

$$\frac{1}{4\pi} \int d\Omega \left( \frac{\delta T(\phi, \theta)}{T} \right)^2 = \frac{1}{4} \sum_{lm} |a_{lm}|^2 \quad (2.82)$$

where we have used the orthonormality of the spherical harmonics. Equation (2.82) can be simplified considering that the surface of last scattering does not have any privileged direction and then is  $m$ -independent. It is common to define the power spectrum  $C_l$  as the average of  $|a_{lm}|^2$  over  $m$ .

$$C_l = \frac{1}{2l+1} \sum_{m=-l}^l |a_{lm}|^2. \quad (2.83)$$

By substituting the expression of the power spectrum of eq. 2.83 in eq. (2.82) we obtain

$$\frac{1}{4\pi} \int d\Omega \left( \frac{\delta T}{T} \right)^2 = \sum_{l=0}^{\infty} \frac{2l+1}{4\pi} C_l. \quad (2.84)$$

Moreover, it can be shown that the  $C_l$  give information about angular distances which contribute to the temperature fluctuations. Figure 2.7 shows the measurement of the power spectrum using experimental data collected by the Planck satellite. The spectrum basically consists in a set of peaks, which represent a set of angular scales at which a strong correlation in temperature is present. These peaks are results of acoustic oscillations and of the Sachs-Wolfe effect. Acoustic oscillations are due to the competition between two processes in the early tightly coupled baryon-photon plasma: the pressure of the photons tends to erase anisotropies, whereas the gravitational attraction of the baryons, moving at speeds much slower than light, makes them tend to collapse to form overdensities. These two effects compete to create acoustic oscillations, which give to the CMB its characteristic peak structure. The Sachs-Wolfe describes the impact of gravity on CMB photons.

The peak positions provide important information: the position of the first peak confirms the Universe flatness, the even-numbered peaks are associated with how far the baryon-photon fluid compresses due to gravitational potential while odd-numbered peaks indicate the rarefaction effect of radiative pressure.

The dark matter does not cause radiative pressure but contributes to the gravitational wells enhancing the compression peaks (even-numbered) with respect to the rarefaction peaks (odd-numbered). Therefore, the presence of dark matter can justify the described structure needed to match the observations.

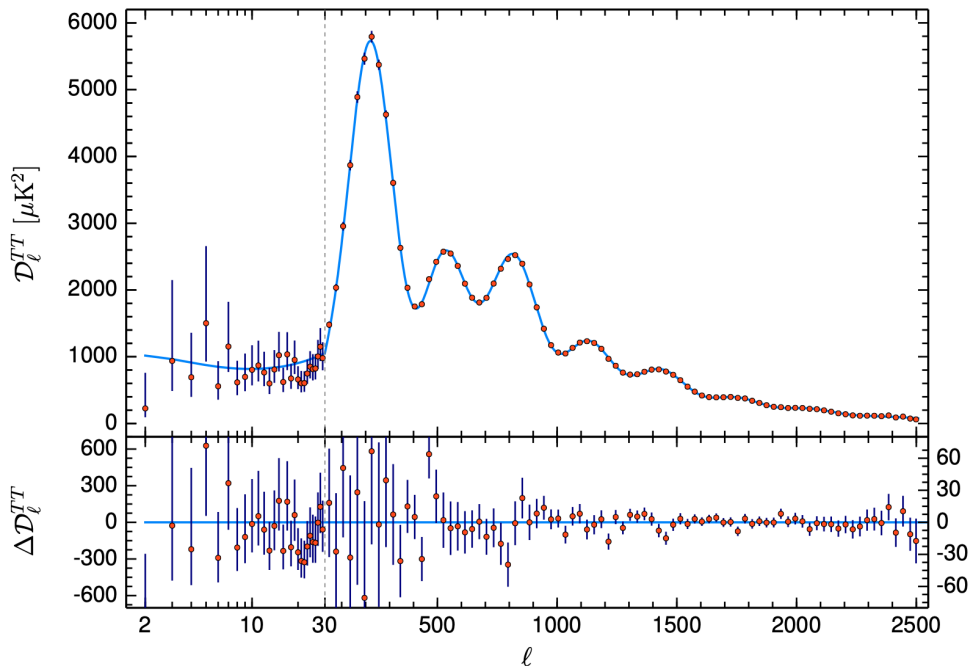


Figure 2.7: Power spectrum of the CMB temperature anisotropies. Experimental data from the Planck satellite are compared with the solid line, which is the best fit. The figure taken from [1]

### 2.4.3 Gravitational lensing

According to General Relativity, in presence of a gravitational potential the light can be deflected by it and as a consequence not propagate in a straight line. In other words the matter has the power to curve space-time and therefore light propagates along the geodesics of the space-time manifold. This deflection is proportional to the mass  $M$  of the object generating the gravitational potential

$$\delta\phi \simeq \frac{4G_N M}{b}, \quad (2.85)$$

where  $b$  is the impact parameter of the propagating photon. With the measurement of the deflection angle of the incoming photons it is possible to deduce the mass parameter.

One can distinguish between strong lensing and weak lensing. The first one happens when a very dense region is present between the source and the observer. The light emitted from the source can follow different geodesics while it propagates to the observer and results in multiple images of the same source in the field of view. Weak lensing corresponds to distortions of the apparent shape of luminous objects by the gravitational potential of a massive source located near the line of sight, between the observer and

luminous source. The result is a magnification (convergence) or a shear of the source image.

One of evidences for dark matter is derived from the weak lensing mass contour of the Bullet cluster. The Bullet cluster is a system of two colliding clusters. The major components of the cluster pair are stars, gas and dark matter.

The dark matter was indirectly detected using gravitational lensing. The total cluster mass distribution coincide with the location of the galaxies, displaying spherical shapes indicating that most of the mass contribution did not interact during the collision of the clusters showing that the dark matter is collisionless.

Being the presence of dark matter well motivated, the next step is the illustration of dark matter candidates and detection methods for its studies.

# Chapter 3

## Dark matter

In previous chapter we have introduced the concept of dark matter, as an additional source of collisionless and gravitationally interacting matter which can explain plethora of astrophysical and cosmological observations.

However, understanding the nature of dark matter is one of the most challenging problems in physics. Despite decades of searching, the origin and the nature of dark matter still remains unknown. For over 80 years, astrophysical and cosmological observations have indirectly indicated its existence.

If the dark matter is assumed to be a particle species, several Beyond the Standard Model (BSM) models predict valid candidates with very different characteristics: the range of dark matter mass can go from  $10^{-15}$  GeV to  $10^{15}$  GeV producing scattering cross section from around  $10^{-35}$  pb to 1 pb. All these candidates share some common properties: dark matter particles are expected to be stable or with a life-time at least of the order of the age of the Universe, neutral under electric charge and color charge and be consistent with a broad range of observations on astrophysical and cosmological scales.

The aim of this chapter is to approach the dark matter problem from a particle physics point of view and review the most known particle dark matter models. In sec. 3.1 we will do a first classification of dark matter as cold, warm and hot seeing the consequence on structure formation. In sec. 3.2 we will describe different candidates, concentrating mostly on Weakly Interacting Massive Particles. In sec. 3.3 we will describe different detection methods for dark matter searches and finally in sec. 3.4 we will provide an overview of the different experiments.

### 3.1 A first classification

In early Universe, as we have seen in sec. 2.2.1, particles were in thermal equilibrium thanks to mechanisms like pair production or collisions/interactions with other particles.

In other words, heavy particles were converted in light one and vice versa and both processes had the same rate. As the Universe expanded and cooled two phenomena occurred:

- lightest particles did not have enough kinetic energy to produce heavier particles through interactions;
- the Universe's expansion diluted the number of particles such that interactions did not occurred as frequently as before.

At a certain point, the density of heavier particles became too low to support the thermal equilibrium and that species decoupled; particles were said to "freeze-out" and their comoving number density remained constant [22].

A simple first classification of dark matter particles can be done considering the velocity they had at freeze-out:

- Cold dark matter (CDM): decoupled from radiation after becoming non relativistic;
- Hot dark matter (HDM): decoupled from radiation while they were still relativistic;
- Warm dark matter (WDM): an intermediate case between CDM and HDM.

The previous classification has an important impact on structure formation described in sec. 2.3. In fact, even if the pressure of dark matter is negligible, its perturbation can not collapse towards arbitrary small scales because of the non-zero velocity dispersion. Indeed, being dark matter collisionless, its speed can not be defined as the sound speed i.e.  $c_s = \sqrt{\partial P / \partial \rho}$ , but rather in terms of its thermal velocity, i.e. the thermal motion of particles that make up the matter. The thermal velocity has fundamental implication on structure formation because they can delete perturbations below a certain scale [23]. This scale depends on the mass of the dark matter particles. As soon as the velocity of dark matter particles exceeds the escape velocity of a density perturbation, they stream away before getting gravitationally bound. This phenomenon is called free streaming.

Let's consider again eq. (2.70)

$$\ddot{\delta} + 2H\dot{\delta} = \delta \left[ 4\pi G\rho_0 - \left( c_s^{\text{eff}} \frac{k}{a} \right)^2 \right], \quad (3.1)$$

which has been rewritten by defining an effective speed, which exact expression depends on the considered dark matter candidate. The ansatz for  $c_s^{\text{eff}}$  can be done for the 3 kinds of dark matter we introduced above:

- CDM is non-relativistic, therefore  $c_s^{\text{eff}} \ll c_s$ ; in this case one has the formation of halo structures. In this case one has a "bottom up" scenario for structure formation: galaxies form first and merge into clusters after.

- HDM is relativistic and can escape from small density fluctuations being  $c_s^{\text{eff}} \gg c_s$ . Then, the mass is removed from the fluctuations and essentially smooths out any fluctuation. HDM predicts the "top-down" approach: firstly large structures are created and after they undergo a fragmentation.
- WDM has an effective speed of sound which is a function of the temperature and mass according to  $c_s^{\text{eff}} = T/m$ . This type of candidate predicts both previous scenarios: "top-down" is obtained for smaller structures while "bottom-up" appears to be common for larger ones.

From N-body cosmological numerical simulations of these scenarios for large scale structure formation in our Universe and their comparison with experimental observations, "bottom-up" scenario is favoured. This underlines why we believe it is more plausible that the Universe is dominated gravitationally by cold dark matter [24].

### 3.1.1 The standard $\Lambda$ CDM model

The  $\Lambda$ CDM model represents the cosmological model used nowadays to describe our Universe from the Big Bang to our days, and which is consistent with all observations. It assumes that the Universe contains three major components: (i) a cosmological constant, denoted by  $\Lambda$  associated with the Dark Energy; (ii) cold dark matter, motivated in the previous section and (iii) the ordinary baryonic matter. Radiation contribution to the total amount is very small, as compared to the other components. The free parameters of the  $\Lambda$ CDM model, which are for instance the densities of different components, can be fixed with the data collected by observations of the CMB spectrum.

The three major components nowadays have the following values:

- Dark Energy:  $\Omega_\Lambda = 0.6889 \pm 0.0056$ ;
- Matter:  $\Omega_m = 0.3111 \pm 0.0056$ ;
- Hubble constant:  $67.66 \pm 0.42$ ;
- Radiation:  $\Omega_r = 5 \cdot 10^{-5}$ .

These measurements point out that the dark matter component in the matter energy budget of the Universe is near 85% and around 25% of the total energy density.

## 3.2 Overview of dark matter candidates

The identification of dark matter is a question of central importance in both astrophysics and particle physics.

In astrophysics the properties of dark matter show how structures form and impact the past and the future evolution of the Universe. Moreover it also gives relevant hints on how galaxies and galaxy clusters are gravitationally bound, being present dark matter halos.

In particle physics dark matter can be the empirical evidence for new particles, solving different puzzles in quantum field theory [25]. An example can be hierarchy problem that can be solved considering supersymmetry (SUSY) [3]; moreover SUSY offers dark matter candidates as we will see in sec. 3.2.2.

Figure 3.1 shows some of the most popular dark matter candidates, which are denoted by different masses. However they share some common properties as neutrality and stability on cosmological timescales.

Notice that the dark matter mass is not completely unbounded: the lower limit is  $10^{-22}$  eV. It comes from small structure observation of the Universe: if dark matter was lighter than this limiting value, then its de Broglie wavelength would be large enough to suppress them.

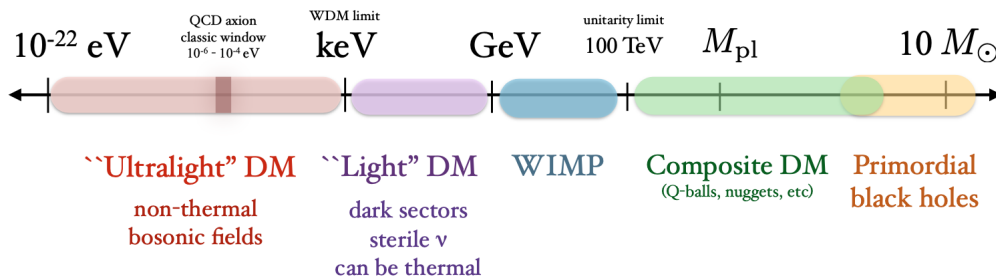


Figure 3.1: Schematic representation of the mass range of allowed dark matter candidates with both particle candidates and primordial black holes. Mass ranges are approximate and are indicated simply to compare the order of magnitude. The illustration is taken from [26].

We begin with the review of more historical dark matter candidates: relic neutrinos and axions, showing that neither of them can satisfy the astrophysical requirements for dark matter candidates. After we will consider sterile neutrinos and composite dark matter candidates such as quark nuggets and macros. We will then introduce few concepts of SUSY and Weakly Interacting Massive Particles (WIMPs), which will be the archetype of dark matter candidates considered further in this thesis.

### 3.2.1 Non-WIMP candidates

#### Relic neutrinos

Among the particle species contained within the Standard Model, neutrinos are the only example of stable, electrically neutral and not strongly interacting particles. Therefore they are the only known particles that can be viewed as potentially viable candidates for dark matter. Actually one considers relic neutrinos: they are called "relic" because they decoupled from radiation and formed what nowadays is called cosmic neutrino background [27].

First of all, one needs to verify if neutrinos can reproduce the correct relic density expected for dark matter. Neutrinos were coupled to the thermal bath via weak interaction processes like

$$\begin{aligned} \nu_e + \bar{\nu}_e &\leftrightarrow e^+ + e^-, \\ e^- + \bar{\nu}_e &\leftrightarrow e^- + \bar{\nu}_e. \end{aligned} \tag{3.2}$$

The cross section for these interactions was proportional to  $\sigma \propto G_F^2 T^2$  where  $G_F$  is Fermi constant. As the temperature decreases, the interaction rate drops, leading to neutrino decoupling. Indeed, at the time of decoupling, neutrinos decoupled from electrons and photons losing as well the ability of annihilation among themselves. To compute the decoupling temperature one needs to take into account all relevant degrees of freedom of the thermal bath: electrons, photons and neutrinos. Solving the Boltzmann equation shown in sec. 2.2.3, one finds that the decoupling temperature of neutrinos is  $T_{\text{dec}} = 1 \text{ MeV}$ , below the electron mass. Notice that neutrinos decoupled being relativistic; now they are non relativistic because of their non zero mass.

Despite this decoupling, neutrinos and photons remained at the same temperature as the Universe expanded. Photon temperature changed when electrons became non relativistic causing an enhancement of the temperature:

$$T_\nu = T_\gamma \quad \rightarrow \quad T_\gamma = \left(\frac{11}{4}\right)^{1/3} T_\nu, \tag{3.3}$$

proportional to relevant degrees of freedom. Knowing the  $T_{0,\gamma}$  which is the radiation temperature measured today, one can compute  $T_{0,\nu}$  as well as number density. Computing the neutrino density, one can estimate

$$\Omega h^2 = \frac{\sum_i m_i^2}{94 \text{ eV}}. \tag{3.4}$$

The sum of neutrino masses has cosmological bound of around 0.6 eV and then the relic density of neutrinos is

$$\Omega h^2 < 0.006, \tag{3.5}$$

that is too low to account for dark matter relic density. This means that Standard Model neutrinos can not be a good dark matter candidate. Another problem is that, being neutrinos almost massless, they are HDM and as described in sec. 3.1 leading to problems with structure formation.

### Axions

Axions are one of the earliest suggestions of viable dark matter. They were introduced in the Quantum Chromo Dynamics (QCD) to solve the strong charge-parity (CP) problem. Indeed, the following term can be embedded into the QCD Lagrangian

$$\mathcal{L}_{\text{QCD}} = \theta \frac{g_s^2}{21\pi^2} G_{\mu\nu}^a \tilde{G}_a^{\mu\nu}, \quad (3.6)$$

where  $g_s$  is the strong interaction coupling,  $G_{\mu\nu}^a$  is the gluon field strength and  $\tilde{G}_{\mu\nu}^a$  is its dual tensor. Equation (3.6) introduces CP violation and this creates tension with the experimental results for instance of the electric dipole moment of neutron. To keep the contribution of eq. (3.6) small,  $\theta$  should be close to zero. The solution to this problem was proposed by Roberto Peccei and Helen Quinn in 1977 [28]. They introduced a new U(1) global symmetry, which is broken by the spontaneous symmetry breaking mechanism. According to the Goldstone theorem, there should be a massless Goldstone boson. This boson was identified with the pseudoscalar axion. The axion interaction term can then be written as

$$\mathcal{L}_a = -\frac{g_s^2}{32\pi^2} \frac{a}{f_a} \epsilon^{\mu\nu\rho\sigma} \tilde{G}_{\mu\nu}^a G_{\rho\sigma}^a, \quad (3.7)$$

where  $f_a$  is the scale at which the symmetry is broken and contributes to the axion mass. At cosmological level, the axion mass needed to solve the CP problem can not properly solves the dark matter problem for a small range of masses. In particular, the axion mass can be expressed as

$$m_a = 0.62 \text{ eV} \left( \frac{10^7 \text{ GeV}}{f_a} \right). \quad (3.8)$$

A naive expectation from Grand Unified Theories (GUT) is that  $f_a$  is related to the unification scale  $\sim 10^{16}$  GeV; this drives the axion mass in the range of  $m_a \sim \mu\text{eV}$ . However such a light axion produces an overclose Universe [2]. A more massive axion can be obtained considering the Spontaneous Breaking of PQ symmetry happened before inflation; as the consequence the axion mass is in range  $m_a \sim \text{meV}$ .

On the other hand, being cold dark matter, axion-like particles can reproduce the correct structure formation.

### Sterile neutrinos

Another candidate for dark matter is the sterile neutrino. Sterile neutrinos are hypothetical particles which are connected and can mix with the known active neutrinos. From the Standard Model point of view, sterile neutrinos are right-handed fermions with zero hypercharge and no color: in other words, they are singlets under the Standard Model gauge group and thus perfectly neutral. The only two ways in which they can interact are gravitationally and mixing with Standard Model particles. Due to the lack of electric charge, hypercharge and color charge, sterile neutrinos would not interact electromagnetically, weakly, or strongly, making them extremely difficult to detect. However, these properties allow sterile neutrinos to have a mass that does not depend on the Higgs mechanism. This so-called Majorana mass can exist independently of electroweak symmetry breaking. Usually one considers the mass of sterile neutrino in the range of keV for 2 reasons both arising from astrophysical and cosmological considerations. Strong astrophysical bound comes from the non-observation of the monoenergetic X-rays induced by the decay of sterile neutrinos; the second motivation is the entanglement between the type of dark matter (particularly its velocity) and the formation of structures in the Universe [4]. Another problem is linked to the freeze-out of sterile neutrinos which can happen leading to the possibility of cold, warm and even hot scenarios, depending on the velocity and mass of axions, which are still debated.

### Macro dark matter

Macros represent a general class of composite dark matter candidates with masses and interaction cross sections characterized in units of grams and  $\text{cm}^2$ . The idea behind Macros is that they can be effectively or better naturally weakly interacting because of their huge mass. The interaction rate is proportional to the density and velocity of particles i.e.  $\Gamma \propto n_X \sigma_X v$ , with  $n_X$  and  $\sigma_X$  being their density and interaction cross section respectively. In other words, one can consider that  $n_X \propto \rho_X M_X^{-1}$  and being  $\rho_X$  fixed for any dark matter scenario, the event rate is proportional to  $\sigma_X M_X^{-1}$ . Conventionally dark matter is weakly interacting because  $\sigma_X$  is small; however, one can have the other case in which  $M_X$  is huge; this is the reason why Macros are considered [29]. Another advantage is that these objects can be assembled out of Standard Model particles and no BSM physics is potentially required.

Earth-based experiments, cosmological and astrophysical observations constrain the Macro parameter space, leaving as allowed region the mass range in between  $55 - 10^{17}$  g and  $2 \cdot 10^{20} - 4 \cdot 10^{24}$  g [29].

### Quark nuggets

Quark nuggets are examples of macroscopic dark matter candidates and were proposed originally by Witten [30]. These particles can be produced in the early Universe at the

epoch of quark confinement for a wide range of confining theories as QCD-like gauge theories.

There are two necessary conditions for quark nuggets: a non zero baryon number asymmetry i.e. a cosmological excess of matter over antimatter and a first order phase transition i.e. a transition with at least two phases with different energies.

The original Witten's proposal was the formation of quark nuggets with the first order QCD phase transition, which guarantees an interface between two region of the Universe in different phases. In the region with high temperatures phase baryons were trapped forming stable nuggets. However, lattice QCD calculations have shown that this mechanism is inapplicable within the well known QCD [31].

Alternative mechanisms can be considered following the same idea. For example the spontaneous symmetry breaking of a  $Z(3)$  symmetry in high temperature phase space, i.e. the quark-gluon phase and vacuum expectation value act as order parameters for a first order phase transition.

Quark nuggets can be imagined as macroscopic nucleons with a very large baryon number,  $N_B > 10^{30}$ . Their properties depend on the confining scale. For confinement scales from 10 keV to 100 TeV, quark nuggets have a mass in the range  $10^{23}$  g -  $10^{-7}$  g, with a radius in the range  $10^8$  cm -  $10^{-15}$  cm [32].

### 3.2.2 WIMP candidates

WIMPs are very common dark matter candidates. These particles, if they exist, have been created thermally in the early Universe, with a weak interaction cross section and a mass in the range 1 GeV – 100 TeV. The main motivation for WIMPs, beside their natural way of being weakly interacting, is that they can guarantee correct relic density, in agreement with data. This prediction is known as the "WIMP miracle" [15].

The main WIMP candidates arise once one considers BSM extensions. Among the most studied BSM models there are SUSY, Extra Dimensions [33] and Little Higgs theories [34]. In each of these extensions, the WIMP candidates are stable because they are protected by a conserved quantum number:  $R$ -parity,  $K$ -parity and  $T$ -parity respectively. Here we briefly discuss the supersymmetric case of WIMP, the neutralino. In this thesis we will consider dark matter candidate within the WIMP paradigm.

#### Supersymmetric particles

SUSY is a type of space time symmetry which introduces a superpartner for all the Standard Model particles, associating to each fermion a boson and vice versa.

SUSY can be considered an elegant solution to many current problems in particle physics such as hierarchy problem and the gauge coupling unification, being as well a necessary condition for string theory [3, 35].

Minimal Supersymmetric Standard Model		
Interaction eigenstates		Mass Eigenstates
$\tilde{q}_L, \tilde{q}_R$	squark	$\tilde{q}_1, \tilde{q}_2$
$\tilde{l}_L, \tilde{l}_R$	slepton	$\tilde{l}_1, \tilde{l}_2$
$\tilde{\nu}_L$	sneutrino	$\tilde{\nu}_L$
$\tilde{g}$	gluino	$\tilde{g}$
$\tilde{W}^\pm$	wino	$\tilde{\chi}_{1,2}^\pm$
$\tilde{H}^\pm$	higgsino	charginos
$\tilde{B}$	bino	$\tilde{\chi}_{1,2,3,4}^0$ neutralinos
$\tilde{W}^3$	wino	
$\tilde{H}_u^0$	higgsino	
$\tilde{H}_d^0$	higgsino	

Figure 3.2: Superpartners (usually indicated with a tilde) content of the Minimal Supersymmetric Standard Model: both the interaction and mass eigenstates are presented.

The Minimal Supersymmetric Standard Model (MSSM) is the minimal extension of the Standard Model including SUSY. The particle content of Standard Model is doubled introducing a spin-0 particle for each fermion and a spin-1/2 partner for each gauge boson. For this Higgs boson another doublet is introduced to avoid gauge anomalies. All the new SUSY particles are listed in fig. (3.2).

According to SUSY, the particles and their superpartners must have the same mass. However, no experimental observations have been found for their existence. If they exist, superpartners are forced to be heavier and for this reason SUSY is expected to be a broken symmetry. More details can be found in [3].

Considering the superpotential  $W_{MSSM}$ , which is a holomorphic function constructed with all gauge invariant and renormalizable terms, one obtains a theory that violates both baryon number  $B$  and lepton number  $L$ . This would predict the proton decay, in contrast with the experimental data. This problem can be avoided by requiring a new discrete symmetry called " $R$ -parity"

$$P_R = (-1)^{3(B-L)+2s}, \quad (3.9)$$

where  $s$  is the spin of the particle. For all the Standard Model particles  $R = 1$  while for superpartners  $R = -1$ . With  $R$  parity, the decay of proton is forbidden. Moreover, there is an extremely important phenomenological consequences of  $R$ -parity: the lightest sparticle is called the lightest supersymmetric particle (LSP) and it must be absolutely stable. If the LSP is electrically neutral, it interacts only weakly with ordinary matter, and so can make an attractive candidate for the non-baryonic dark matter.

In most of the SUSY models, the LSP is the lightest neutralino,  $\tilde{\chi}_1^0$ . There are four neutralinos, which are given by the linear combination of the bino  $\tilde{B}$ , supersymmetric partner of the photon, the neutral wino  $\tilde{W}^3$ , superpartner of  $W$  boson, and the two

Higgsinos  $\tilde{H}_d^0$  and  $\tilde{H}_u^0$ , superpartners of the Higgs.

$$\tilde{\chi}_i^0 = a_1^{(i)} \tilde{B} + a_2^{(i)} \tilde{W}^3 + a_3^{(i)} \tilde{H}_d^0 + a_4^{(i)} \tilde{H}_u^0 \quad i = 1, \dots, 4. \quad (3.10)$$

Neutralinos are the mass eigenstates of the following mass matrix

$$M_{\tilde{\chi}^0} = \begin{pmatrix} M_1 & 0 & -m_Z c_\beta s_{\theta_W} & m_Z s_\beta s_{\theta_W} \\ 0 & M_2 & m_Z c_\beta c_{\theta_W} & -m_Z s_\beta c_{\theta_W} \\ -m_Z c_\beta s_{\theta_W} & m_Z c_\beta c_{\theta_W} & 0 & -\mu \\ m_Z s_\beta s_{\theta_W} & -m_Z s_\beta c_{\theta_W} & -\mu & 0 \end{pmatrix}, \quad (3.11)$$

where for convenience we have set  $c_\phi = \cos(\phi)$  and  $s_\phi = \sin(\phi)$  with  $\phi = \beta, \theta_W$ .  $\beta$  is defined as the ratio of two Higgs vacuum expectation values

$$\tan \beta = \langle H_u^0 \rangle / \langle H_d^0 \rangle = v_u / v_d, \quad (3.12)$$

and  $\theta_W$  is the Weinberg angle. The  $\mu$  parameter comes from the Higgs mixing mass term in the superpotential

$$W_{\text{MSSM}} \supset \mu (H_u)_\alpha (H_d)_\beta \epsilon^{\alpha\beta} = \mu (H_u^+ H_d^- - H_u^0 H_d^0). \quad (3.13)$$

$M_1$  and  $M_2$  are the bino  $\tilde{B}$  and winos  $\tilde{W}^i$  mass terms present in the SUSY soft breaking Lagrangian

$$\mathcal{L}_{\text{MSSM}}^{\text{soft}} \supset -\frac{1}{2} (M_1 \tilde{B} \tilde{B} + M_2 \tilde{W}^i \tilde{W}^i + \dots). \quad (3.14)$$

If  $M_1, M_2$  and  $\mu$  term are greater than the EW scale, i.e.  $M_1, M_2, \mu \gg m_Z$ , the neutralino eigenstates can be expressed as

$$\tilde{\chi}_i^0 \simeq \left\{ \tilde{B}, \tilde{W}^3, \frac{1}{\sqrt{2}} (\tilde{H}_d^0 - \tilde{H}_u^0), \frac{1}{\sqrt{2}} (\tilde{H}_d^0 + \tilde{H}_u^0) \right\}, \quad (3.15)$$

with the mass values

$$m_{\tilde{\chi}^0} \simeq \{M_1, M_2, |\mu|, |\mu|\}. \quad (3.16)$$

Approximately, for large values of  $M_1$  and  $M_2$ , the LSP neutralino  $\tilde{\chi}^0$  is "higgsino"-like with the mass depending mainly on  $\mu$ , roughly speaking  $m_{\tilde{\chi}^0} \simeq \mu$ . For large value of  $\mu$ , the LSP neutralino is "bino-like" and  $m_{\tilde{\chi}^0} \simeq M_1$ .

### 3.3 Detection methods

There exist several ways of searching for dark matter with Earth-based experiments and satellites. All the detection methods assume that the dark matter interacts with ordinary matter not only gravitationally. Therefore searches for dark matter are done by looking at its interactions with other particles.

There are 3 main dark matter detection methods:

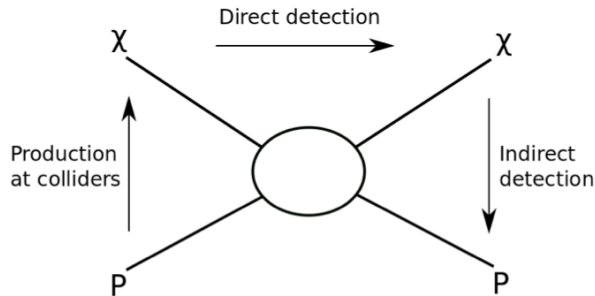


Figure 3.3: Schematic representation of the three main dark matter detection methods. Indirect detection is obtained via the process  $\chi\chi \rightarrow pp$ , direct detection is characterised by the process  $p\chi \rightarrow p\chi$ , and finally collider searches are interested in the process  $pp \rightarrow \chi\chi$ .

- Indirect detection: intends to detect the products of dark matter annihilation or decay in galactic halos;
- Direct detection: intends to study the elastic scattering between dark matter and Standard Model particles in underground detectors;
- Collider searches: intend to produce dark matter particles via the scattering of Standard Model particles in a collider.

Figure 3.3 shows a schematic representation for the three different detection methods. We focus mostly on indirect detection, as this method has been largely used in our analysis. From now on we will use  $\chi$  for dark matter particles and  $\bar{\chi}$  for dark matter antiparticles. In this section we review the main peculiarities of these methods.

### 3.3.1 Indirect detection

Indirect detection focuses on searching for Standard Model particles produced by the annihilation or decay of dark matter particles or their secondary effects.

Indirect detection faces challenges because dark matter is known to interact only weakly with the Standard Model so the rate of produced particles is expected to be small and many possible detection channels have large backgrounds from astrophysical particle production.

Dark matter is concentrated in structures called halos, where its density is largely enhanced, so that the annihilation processes can be significant and detectable signals can be produced.

In halos, dark matter particles are considered nearly at rest being their kinetic energy very small, because the typical velocities in galactic halos are of the order  $v \sim 10^{-3}c$ .

The centre-of-mass energy of the dark matter annihilation is then  $s = 4m_\chi^2$ , where  $m_\chi$  is the mass of the dark matter particle. The annihilation of dark matter particles can produce a pair of all possible kinematically allowed particles. These final state particles can be stable, as for example neutrinos, metastable and even BSM particles, subsequently decaying into Standard Model particles. These products can undergo hadronisation and decay unless or until stable products are realized. We can consider the following example for a dark matter annihilation process

$$\chi\bar{\chi} \rightarrow q\bar{q} \rightarrow p\bar{p} + X, \quad (3.17)$$

where two dark matter particles annihilate into a pair of quarks. These quarks then hadronize producing different unstable products, which subsequently decay in stable particles which are in this example a proton and an antiproton. All the other products are indicated with  $X$ .

More in general, one can consider  $\chi\bar{\chi} \rightarrow e^+e^-, \mu^+\mu^-, \tau^+\tau^-, \nu_l\bar{\nu}_l, q\bar{q}, c\bar{c}, b\bar{b}, t\bar{t}, W^+W^-, ZZ, gg, \gamma\gamma, hh$  as annihilation products.

Almost all of the above annihilation products are unstable and suffer hadronization, showering, Bremsstrahlung and decay into lighter stable particles. The final results generate what we identify with secondary channels. Stable particles, arising after different physical processes listed above, are: positrons  $e^+$ , antiprotons  $\bar{p}$ , gamma rays  $\gamma$ , antideuterium  $\bar{d}$ , electron neutrino  $\nu_e$ , muon neutrino  $\nu_\mu$  and tau neutrino  $\nu_\tau$ . Notice that we usually consider anti-matter (positrons, antiprotons, antideuterium) because it is easier to detect with respect to matter (electrons, protons and deuterium), which are typically produced in large number as consequence of different astrophysical events. Of particular interest are photon and neutrino final states because these particles are not affected by the electromagnetic fields of the galaxy and interstellar medium on their way of propagation to reach the Earth, and travel unaffected in astrophysical environment. Therefore they point directly back to the location they were produced, giving precious information on dark matter sources. It is convenient to focus the search on regions of the Universe where we suppose the dark matter concentration is larger, to maximize the expected flux of particles.

The observable which is considered in indirect detection is the flux of particles,  $\Phi$ . Considering a generic dark matter candidate that annihilates into the SM species  $i$  with branching ration  $B_i$ , the flux is given by

$$\Phi(E, \psi) = \frac{\langle\sigma v\rangle}{2m_\chi} \sum_i \frac{dN}{dE} \frac{1}{4\pi} \int_\psi \frac{d\Omega}{\Delta\psi} \int_{\text{l.o.s.}} \rho^2(\psi, l) dl, \quad (3.18)$$

where we have considered dark matter annihilation from the direction  $\psi$  in the sky averaged over an opening angle  $\Delta\psi$  [7]. Here redshift or absorption effects are neglected. The above expression encapsulates three important aspects for the dark matter

- $\langle\sigma v\rangle$  represents the velocity averaged annihilation cross section of the dark matter; in case of decaying dark matter this quantity is replaced with the decay width  $\Gamma = 1/\tau$ , where  $\tau$  is the dark matter lifetime.
- $dN/dE$  is the energy spectrum of the final state stable particles arising from the annihilating or decaying dark matter particle. Depending on dark matter mass, different amounts of energy can be imparted to the products. Depending on the particle species, the energy spectrum can be very different.
- The last part of (3.18) arises from astrophysics and is related to the dark matter density. Usually this is defined as  $J$  factor, which contains the information about the chosen dark matter density profile in the system of interest. Notice that for decay processes one should consider  $\rho$  instead of  $\rho^2$  in the integral. From now we consider only annihilation processes for dark matter and do not discuss further the case of decaying dark matter.

The distribution of dark matter is a key input for indirect detection. There exist several standard density profiles. Here we list the most used ones, which for simplicity consider  $\rho$  as a spherically-symmetric distribution depending only on the radial part i.e.  $\rho(\vec{r}) = \rho(r)$

- The Navarro-Frenk-White (NFW) profile is given by [36]

$$\rho_{\text{NFW}} = \rho_0 \left(\frac{r}{r_s}\right)^{-\gamma} \left(1 + \frac{r}{r_s}\right)^{\gamma-3}, \quad (3.19)$$

where  $r_s$  is the scale radius and  $r$  is the distance from the galactic center. This is an example of a cuspy profile.

- Einasto profile [37]

$$\rho_{\text{Ein}}(r) = \rho_0 \exp\left\{-\frac{2}{\alpha} \left[\left(\frac{r}{r_s}\right)^\alpha - 1\right]\right\}, \quad (3.20)$$

where  $r_s$  is the scale radius and  $\alpha$  controls the parameter of the curvature of the profile. It is an exponential profile.

- Burkert profile [38]

$$\rho_{\text{Bur}}(r) = \rho_0 \left(1 + \frac{r}{r_s}\right)^{-1} \left(1 + \frac{r^2}{r_s^2}\right)^{-1}. \quad (3.21)$$

This last density profile is characterised by a flatter density behaviour at small  $r$ , because it has a constant density inside the radius  $R$ . It is an example of cored profile.

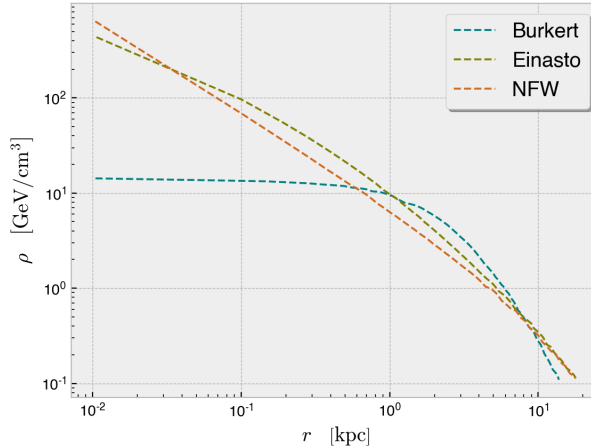


Figure 3.4: dark matter galactic density halo profile as a function of the distance from the centre of the galaxy  $r$ , comparing Burkert, Einasto and NFW profiles. Data are taken from [15]

These density profiles are illustrated in fig. 3.4: one can notice that while NFW and Einasto profiles present a similar behaviour, Burkert profile presents different orders of magnitude smaller density profile in the vicinity of the galactic centre. The  $J$  factor plays an important role because the flux  $\Phi$  is proportional to this astrophysical factor: this means that a strong signal corresponds to a huge dark matter density. One of the main target for dark matter searches is the Milky-Way galactic centre, which additionally holds different large substructures. Other promising dark matter targets are the dense satellites of the Milky Way called dwarf spheroidal galaxies. In our analysis we will consider the indirect detection bounds coming from the latter targets.

A convincing explanation of dark matter detection based on measurement of  $\Phi$ , which is not clearly distinguishable from astrophysical background, appears particularly challenging [39]. For this reason, it is often much better to focus on the pronounced spectral features that are expected in many dark matter models. In other words, dark matter annihilations can lead to sharp spectral features which can be easily distinguished from the background and can be considered as smoking gun signatures for discoveries. Such spectral features can be classified into two categories: (i) monochromatic lines and (ii) box-shaped spectra.

The first one arises in the annihilation directly into pairs of neutrinos or photons. Box-shaped spectra appear when dark matter annihilates into BSM mediators, which subsequently decay into neutrinos or photons. All these kinds of signatures are characteristic with respect to featureless soft background [40]. Let's describe the main features

of these two kind of characteristic signatures.

### Monochromatic lines

The direct annihilation of dark matter pairs into a pair of photons or neutrinos leads to monochromatic signatures, which are extremely difficult to explain with astrophysical contributions. However, these signatures are often loop-suppressed and can arise only in specific models. Comparing  $\gamma$  and  $\nu$  lines, the experimental sensitivities reported for photons are orders of magnitude better than for neutrinos. For instance, for  $m_\chi = 100$  GeV (10 TeV) the upper bounds provided by IceCube, a neutrino telescope, are  $\langle\sigma v\rangle \simeq 0.5 \cdot 10^{-23}$  cm<sup>3</sup>/s ( $4 \cdot 10^{-23}$  cm<sup>3</sup>/s) [41], orders of magnitude weaker than those given for monochromatic photons,  $\langle\sigma v\rangle_{\gamma\gamma} \simeq 2 \cdot 10^{-28}$  cm<sup>3</sup>/s by the Fermi-LAT satellite [42]. However, this should not discourage the search for neutrino-line signals: it means that one must look into specific models where the production of monochromatic photons is suppressed with respect to neutrinos. This kind of model is for example one with suppressed quark production and with heavy dark matter candidates. For our work, as we will see in the next chapter, we have considered a leptophilic model. In this case direct annihilation into  $\gamma\gamma$  is always at 1-loop level [5], while neutrino lines arise at tree level. Additionally, notice that the next generation of neutrino telescopes are expected to largely improve their sensitivity to the flux of monochromatic neutrinos produced by dark matter in our galaxy.

Considering the monochromatic neutrino line signal, in general the total cross section is the sum over all the neutrino flavor final states

$$\sigma v = \sum_{\alpha,\beta=e,\mu,\tau} \sigma v_{\nu_\alpha \bar{\nu}_\beta}. \quad (3.22)$$

This definition is convenient because it is independent on how neutrinos oscillate. Neutrino oscillations are described by the three flavour leptonic mixing matrix, UPMNS, as in [43]. If one assume an equal production of  $\nu_e$ ,  $\nu_\mu$  and  $\nu_\tau$ , in the case of dark matter annihilation in the galactic centre, the distance travelled by neutrinos to reach the detector on Earth is very huge, hence the neutrino flavor final state can be approximated with  $\nu_e : \nu_\mu : \nu_\tau = 1 : 1 : 1$  [7], no matter what is the initial state. Namely even if only electron neutrino are produced at source, those oscillate and populate the other flavours with equal probability.

For  $\chi\bar{\chi} \rightarrow \nu\bar{\nu}$ , which has a two-body final state with two monochromatic neutrinos, we have

$$\frac{dN}{dE_\nu} = \delta\left(E_\nu - \frac{m_\chi}{2}\right). \quad (3.23)$$

The line picks at  $m_\chi$ . However, the delta function is smeared out by the velocity distribution and detector resolution. The line usually appears as a gaussian rather than a line.

The galactic center and the Sun are preferred targets of observation for neutrino telescopes.

### Box-shaped spectra

To discuss this kind of signature, let's consider a simple example in which we have the annihilation of dark matter pair into massive bosons  $\chi\bar{\chi} \rightarrow Z'Z'$  which subsequently decay into two neutrinos, namely  $Z' \rightarrow \nu\bar{\nu}$ . We want to investigate the resulting neutrino spectrum, which is box-shaped and depends only on the polarization of the massive boson. In our case we have considered an unpolarized boson. In the dark matter centre of mass frame, the energy of the neutrino can be expressed as

$$E_\nu = \frac{m_{Z'}^2}{2m_\chi} \left( 1 - \cos\theta \sqrt{1 - \frac{m_{Z'}^2}{m_\chi^2}} \right)^{-1}, \quad (3.24)$$

where the  $\cos\theta$  is the angle between the outgoing neutrino and its parent boson. The spectrum has sharp ends depending on  $m_\chi$  and  $m_{Z'}$ . Being the considered boson unpolarized, the emission of the neutrinos is isotropic. The box then is

$$\frac{dN_\nu}{dE_\nu} = \frac{4}{\Delta E} \Theta(E - E_-) \Theta(E_+ - E), \quad (3.25)$$

where  $\Theta$  is the Heaviside function,  $\Delta E = \sqrt{m_\chi^2 - m_{Z'}^2}$  is the box width and  $E_\pm = m_\chi/2 \left( 1 \pm \sqrt{1 - m_{Z'}^2/m_\chi^2} \right)$  represents the box edges. Our results agree with [40, 44]. If the masses of  $\chi$  and  $Z'$  are comparable, the box is indistinguishable from a line while if  $m_\chi \ll m_{Z'}$ , the box is very wide.

We can calculate the total neutrino flux from dark matter annihilation as

$$\Phi_\nu = \frac{\langle\sigma v\rangle}{8\pi m_\chi^2} \frac{dN_\nu}{dE_\nu} \frac{1}{\Delta\Omega} \int_{\Delta\Omega} d\Omega \int_{1.o.s} ds \rho_{DM}^2, \quad (3.26)$$

where  $\langle\sigma v\rangle$  is the thermal annihilation cross section,  $\rho_{DM}$  is the dark matter density and  $s$  is the distance along the line of sight.

If the boson  $Z'$  were polarized the box would be deformed into different shapes which are determined by the initial polarization: for longitudinally polarized bosons, one would have a concave shape around the center of the box while for transverse it would lead to convex spectrum [40].

### Electroweak corrections

When dark matter annihilates into a pair of highly energetic Standard Model particle-antiparticle states, it is possible to radiate Electroweak boson, besides the usual photons

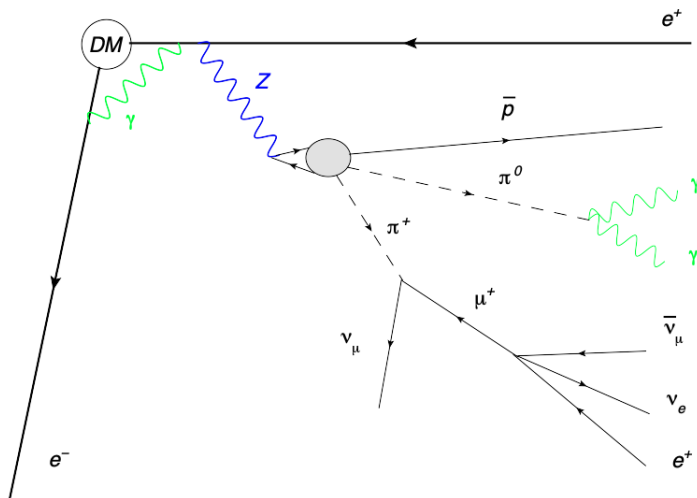


Figure 3.5: Feynman diagram for hard positron and electron production in dark matter annihilation. The resulting spectrum is altered by both virtual emissions as green photon lines and real  $Z$  via their subsequent decays [45].

and gluons. All these radiated particles are usually unstable, therefore decay and modify significantly the shape of the secondary energy spectra and can even modify its composition because of production of new final states. Taking for example a neutrino final states, including Electroweak corrections, one has all spectra of stable particles, contrary to the case when they are not considered.

For electroweak radiation, the fundamental requirement is that the dark matter mass  $m_\chi$  should be larger than the electroweak scale. In fact, at such energies, soft electroweak gauge bosons are copiously radiated from high energy products of annihilation [45]. What happens can be understood using standard collider physics argument. At energies much larger than the electroweak scale, soft electroweak gauge bosons are copiously radiated from hard final states because  $W^\pm$  and  $Z$  are basically massless at those energies, similarly to the QED and QCD radiation. This is illustrated in fig. 3.5, where the  $e^+e^-$  final state is considered as example. The hard positron spectrum is slightly altered by the emission of real and virtual bosons ( $\gamma$  and  $Z$ ) and new hadronic channels are opened: for instance, looking at the diagram, one immediately understands that antiprotons are produced, while those would not be present without those radiative corrections. Moreover, a large number of pions are produced, subsequently decaying into photons and low energy positrons according to e.g.  $\pi^0 \rightarrow \gamma\gamma$ , and  $\pi^+ \rightarrow \mu^+ + X \rightarrow e^+ + X$  respectively.

The exchange of real and virtual bosons lead to the appearance in the final spectrum of all the stable particles and not only the ones initially emitted by the dark matter

annihilation when one considers  $e^-$ ,  $\nu$  and  $\mu$ .

### 3.3.2 Direct detection

The direct detection strategy is based on measuring the recoil of a nucleus, after this one has scattered with a dark matter particle. Dark matter particles scatter off the atom nucleus and the transferred momentum gives rise to a nuclear recoil which might be detectable. The direct detection detectors are usually set up underground in order to isolate them from the most important backgrounds as natural radioactivity and cosmic radiation.

Additional to the measurement of the nuclear recoil, directional information is important because it could lead to more precise measurements of intrinsic particle properties of dark matter as well as astrophysical information (for example dark matter velocity distribution and irreducible neutrino background), but we will not consider this case further.

The expected event rate of dark matter scattering off a target nucleus of mass  $m_N$  is given by

$$\frac{dR}{dE_{\text{nr}}} = \frac{\rho_{\odot} M}{m_N m_{\chi}} \int_{v_{\text{min}}}^{v_{\text{esc}}} v f(v) \frac{d\sigma}{dE_{\text{nr}}} dv, \quad (3.27)$$

where  $\rho_{\odot}$  is the dark matter density,  $E_{\text{nr}}$  is the nuclear recoil energy,  $m_{\chi}$  is the dark matter mass,  $M$  is the target mass of the detector,  $\sigma$  is the scattering cross section,  $f(v)$  is the normalized dark matter velocity distribution and  $\rho_0$  is the local dark matter density [46]. The velocity  $v_{\text{esc}} \simeq 544 \text{ km} \cdot \text{s}^{-1}$  [47] represents the escape velocity of dark matter particles from the galactic halo at the Sun position. The minimal velocity required for a dark matter particle to induce a nuclear recoil of energy  $E_{\text{nr}}$  is

$$v_{\text{min}} = \sqrt{\frac{E_{\text{nr}} m_N}{2\mu_N^2}}, \quad (3.28)$$

where  $\mu_N$  is the reduced nucleon-dark matter mass

$$\mu_N = \frac{m_{\chi} m_N}{m_{\chi} + m_N}. \quad (3.29)$$

Because of its large de Broglie wavelength, being the dark matter non relativistic, the dark matter particles interact with the nucleons in the target. The eq. (3.27) is both velocity and recoil-energy dependent and is given by [46]

$$\frac{d\sigma}{dE_{\text{nr}}} = \frac{m_N}{2v^2 \mu_N^2} (\sigma_{SI}^0 F_{SI}^2(E_{\text{nr}}) + \sigma_{SD}^0 F_{SD}^2(E_{\text{nr}})), \quad (3.30)$$

or in other word it can be written as a sum of spin independent (SI) and spin dependent (SD) contribution, each of which is weighted by its form factor  $F$ . Since the interaction

of dark matter with the baryonic matter is a priori unknown, different Lagrangians can produce the same effective interaction. For instance with a scalar  $\mathcal{L}_S \sim \bar{\chi}\chi\bar{N}N$  or a vector  $\mathcal{L}_V \sim \bar{\chi}\gamma^\mu\chi\bar{N}\gamma^\mu N$ , give rise to the same spin independent cross section. On the other hand, the axial vector  $\mathcal{L} = \bar{\chi}\gamma^\mu\gamma^5\chi\bar{N}\gamma^\mu\gamma^5 N$  produces the spin dependent interaction.

In the spin independent case, the cross section is expressed as

$$\sigma_{SI}^0 = \frac{\mu^2}{\mu_N^2} \frac{(f_p Z + f_n (A - Z))^2}{f_n^2}, \quad (3.31)$$

where  $\mu_N$  is the dark matter-nucleus reduced mass,  $A$  is the mass number and  $Z$  is the atomic number;  $f_p$  and  $f_n$  describe the effective dark matter coupling strength to protons and neutrons respectively. The interaction is called spin independent because the dark matter see the nucleus as a whole and it is proportional to  $A^2$ , hence it is larger for heavier nuclei. For spin dependent interactions, the dark matter particle with spin different from zero interacts with the spin of the nucleus (namely given by the unpaired nucleon). Adopting the result in [48], the cross section is

$$\sigma_0^{SD} = \frac{32}{\pi} \mu_A^2 G_F^2 [a_p \langle S^p \rangle + a_n \langle S^n \rangle]^2 \frac{J+1}{J} \quad (3.32)$$

where  $J$  is the total nuclear spin and  $a_{p,n}$  are effective proton and neutron couplings.  $\langle S^{p,n} \rangle$  are expectation value of the nuclear spin content due to the proton and neutron.

### 3.3.3 Collider searches

Collider searches for dark matter require basically two conditions: first, the dark matter particles are coupled to the Standard Model, directly to colliding quarks and leptons or indirectly through a mediator. Second, the existence of a detector able to detect missing energy associated with weakly interacting particles, similarly to the neutrinos case.

Collider searches have several advantages. Most of the collider detectors are so-called multi-purpose detectors able to measure a large number of observables: they will be able to detect the kinematic configurations of dark matter production processes. Moreover, the large number of collisions can give more events with missing energy, which can be associate to new BSM physics. The main advantage is that all background processes and all systematic uncertainties can be studied, understood and simulated with great precision. These properties makes the collider searches very promising. There are two different colliders: electron colliders and hadron colliders.

#### Electron collider

In an electron collider,  $e^+$  and  $e^-$  are the colliding particles. Production of dark matter particles can happen in several ways. In this collider we control the initial 4-momenta

and the value of the centre-of-mass energy. A pair of dark matter particles of mass  $m_\chi$  can be produced only if  $\sqrt{s} \geq 2m_\chi$ : this signal however is difficult to detect because being dark matter particles stable, they elude the detector. One then can consider the dark matter production along with another particle as for example a photon, with sufficiently large transverse momentum. This photon is assumed to be radiated by the initial state: this is called initial state radiation. Experimentally this photon recoils against the two dark matter candidates. The experimental signature of this process is often called  $\gamma$  plus missing momentum.

The disadvantage of lepton colliders in the past years was the fact that they can not reach high centre-of-mass energy. Considering the Large Electron Positron collider (LEP) [49], its maximum centre-of-mass energy was near 200 GeV and consequently heavy dark matter particles such as WIMPs could not be produced. Nevertheless, lepton colliders contributed to constrain different regions of parameter space of dark matter particle masses.

High energy lepton colliders with a centre-of-mass energy in the multi-TeV range could be constructed in the future. An example of such a collider is the proposed muon collider, which would feature a clean environment with respect to an hadron collider, high luminosity in the range of  $L = 10^{35} \text{ cm}^{-2}\cdot\text{s}^{-1}$  and up to several TeV centre-of-mass energy [50]. A collider with the above characteristics would open prospects for precision measurements for Standard Model and Standard Model Effective Field Theory (EFT) frameworks as the Higgs's self coupling and the top quark's EW couplings, as well as for new physics, such as the simplified extensions of the Standard Model.

### Hadron colliders

Hadron colliders are characterized by high centre-of-mass energies but have a more complicated experimental environment due to the QCD background. Moreover, when we search for dark matter particles at hadron colliders, we do not have information on initial state kinematics. Hadron colliders as the Large Hadron Collider (LHC) [51] are able to collide protons beams with the energy of 7 GeV each. At these energies, we do not consider protons but their internal constituents which are quarks and gluons. Their energy distribution depends on the parton distribution functions (PDFs) [52] which can be determined only through experiments.

Without the possibility of computing the 4 momenta of the created dark matter particles, a useful variable for our purpose is the missing transverse momentum. The transverse momentum of a particle is defined as

$$\vec{p}_{T,i} = \vec{p}_i \sin \theta, \quad (3.33)$$

where  $\vec{p}_i$  is the momentum of a particle  $i$  and  $\sin \theta$  is its outgoing angle. The missing

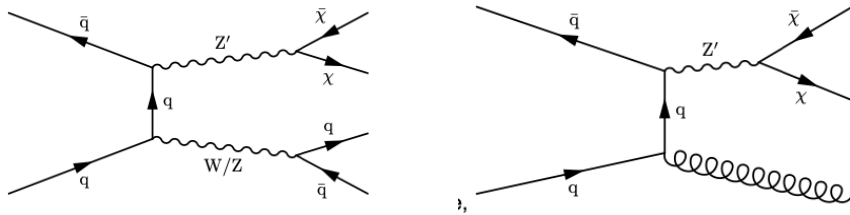


Figure 3.6: Feynman diagrams representing examples of processes for dark matter particle production using a hadron collider. The left panel represents the pair production starting with a BSM particle  $Z'$  and a weak gauge boson; the right panel represents the production associated with the gluon, called mono-jet event.

transverse momentum is defined as

$$\vec{p}_T^{\text{miss}} = - \sum_i \vec{p}_{T,i}. \quad (3.34)$$

A missing transverse momentum different from zero can be a signal of a new invisible particle.

In this case, as in the lepton collider search, one looks for dark matter pair production plus the initial state radiation composed by gluon, photon or weak gauge boson  $W^\pm$  and  $Z$ , as depicted in fig. 3.6. The monojet channel (right plot) is expected to give the strongest contribution due to the gluon emission [53].

However, several experimental problems can occur to mask a potential dark matter signal: for example there will always be particles which are not observed in the calorimeters, hadronic jets are not fully reconstructed leading to fake missing energy in the direction of this jet, mis-measurements of the momenta or a systematic bias cause non-functional parts of the detector.

## 3.4 Experimental constrains

The aim of this section is a brief review of the main experiments currently running, for the dark matter searches presented in sec. 3.3, and the status of the current constraints to the dark matter annihilation or scattering cross section.

### 3.4.1 Indirect detection experiments

The indirect detection as described in sec. 3.3.1 looks for photons, charged cosmic rays and neutrinos, which offer a promising means for dark matter identification.

For the detection of  $\gamma$  rays, currently there are the data provided by the Fermi-LAT and the HESS collaborations [42, 54], as well as HAWC [55], in the range of interests for WIMPs.

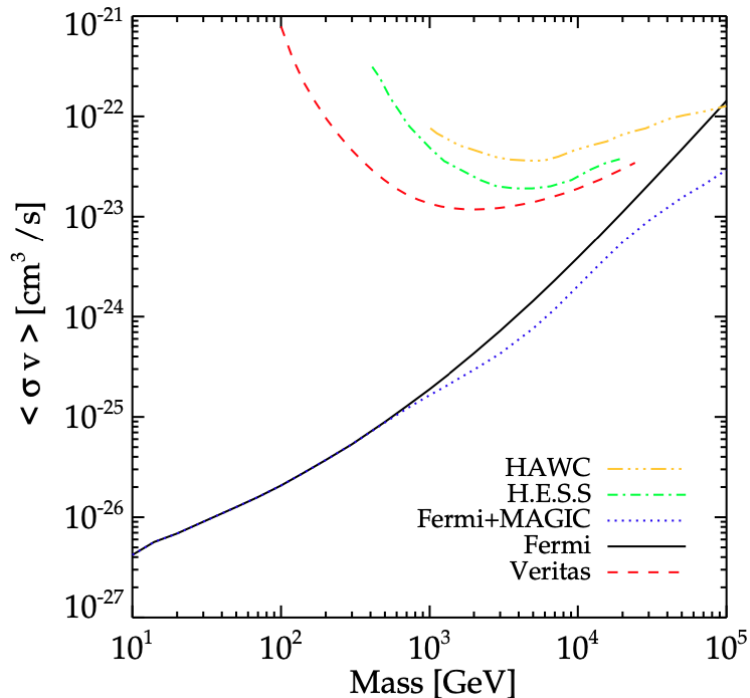


Figure 3.7: Summary plot for the comparison of upper limits on  $\langle\sigma v\rangle$  considering dark matter in  $b\bar{b}$  final states, obtained from Cherenkov observatories and telescopes, as labelled. The figure is taken from [56].

FERMI-LAT, acronym of Fermi Gamma-ray Large Area Space Telescope, is a space observatory. It is able to detect photons with energy from about 20 MeV to more than 1 TeV, measuring their arrival times, energies and directions thank to the large area telescope (LAT) which is its major component [8]. FERMI-LAT works similarly to high energy physics colliders: gamma rays incident on the detector are converted in a pair of  $e^+e^-$ .

HESS (High Energy Stereoscopic System) is an Earth based system of 5 telescopes located in Namibia. It is able to investigate gamma rays in the photon energy range of 3 MeV to 100 TeV using the Cherenkov light. The latter is created by the high energy  $\gamma$ -rays when they interact with the atmosphere producing an extensive electromagnetic shower [57].

For the detection of gamma rays, also promising is the High Altitude Water Cherenkov Observatory (HAWC). HAWC is a cosmic rays observatory located in Sierra Negra in Mexico [55]. It has a one-year sensitivity of 5% – 10% of the flux of the Crab Nebula and is designed to observe gamma rays and cosmic rays between 100 GeV and 100 TeV using Cherenkov light. Model independent values for upper limits on  $\langle\sigma v\rangle$  with 95% CL to the dark matter annihilation cross section can be found in [58].



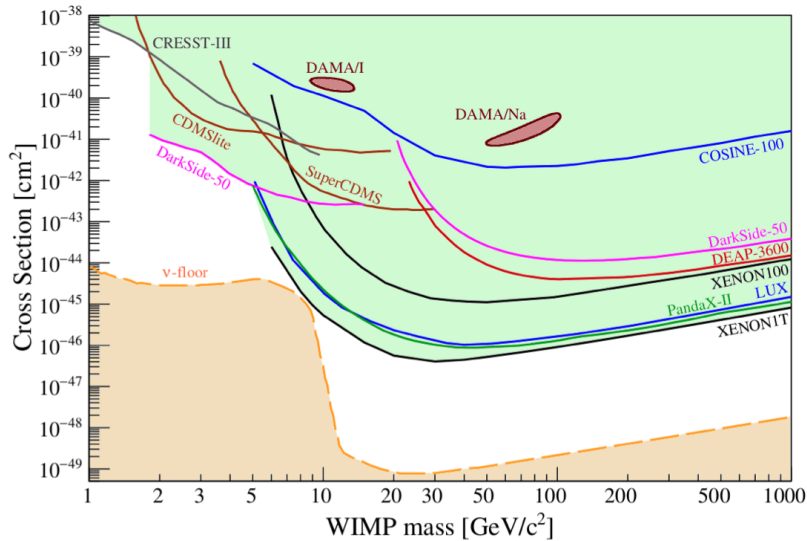


Figure 3.9: Current status of the experimental constraints for the spin independent WIMP-nucleon cross section. The space above the lines is excluded at 90% CL. The different experimental bounds are labelled in the figure, which is taken from [46].

full set up will have two configurations: ORCA (Oscillation Research with Cosmics in the Abyss) located close to Toulon and designed for conducting oscillation research with atmospheric neutrinos and ARCA (Astroparticle Research with Cosmics in the Abyss) situated close to Sicily and optimized for high energies. KM3NeT will instrument a total of  $1 \text{ km}^3$  of water, with 3 blocks of 115 lines each, in different geometries.

In fig. 3.8 are compared the upper limits on  $\langle\sigma v\rangle$  considering different experiments.

### 3.4.2 Direct detection experiments

As we have seen in sec. 3.3.2, the elastic scattering of a dark matter particle off a target material induces an energy transfer to the nuclei, which can be observed. Basically there are three different experimental techniques to detect the nuclear recoil: (i) production of heat (photons in a crystal), (ii) an excitation of the target nucleus which de-excites releasing scintillation photons, (iii) direct ionisation of the target atoms [48]. All the detectors must be constructed underground in order to minimize the background. There are different experiments for direct detection of dark matter.

The Large Underground Xenon (LUX) experiment [63] is installed at the Sanford underground laboratory in the US. This experiment uses a dual phase (liquid-gas) xenon (LXe) detector; events in the LXe target create direct scintillation light while electrons escaping recombination at the event site are drifted to the liquid surface and extracted into the gas phase with an electric fields, where they create electroluminescent light [64].

XENON1T detector [65] provides so far the strongest limits on spin-independent dark matter-nucleus interaction for dark matter mass up to  $10^4$  GeV. It is based on dual phase liquid gas xenon time-projecting chamber with an active target of 2 tonnes. It operates at the Laboratori Nazionali del Gran Sasso in Italy. SuperCDMS detector [66] is one of the experiments of the Cryogenic dark matter Search Collaboration. It is made of the germanium and silicon crystals and use superconducting technology [67]. More specifically, SuperCDMS detectors are designed with the primary function of detecting the minute crystal lattice vibrations and ionization generated after scattering. Being the energy deposited by the interaction  $\propto$  eV, the detector is maintained at a very low temperature.

We show in fig. 3.9 the different bounds on the WIMP-nucleon interaction cross section, considering not only experiments treated in this section but also DAMA [68], CRESST [69], DarkSide-50 [70], COSINE [71], DEAP [72] and CDMSlite [73]. The neutrino floor [74] is included as well. All the experiments provide model-independent upper limits at 90% CL (confidence level), as a function of the dark matter mass, except for the long-standing controversial DAMA result.

### 3.4.3 Experimental bounds from collider searches

As described in sec. 3.3.3, collider searches contribute to exclude different regions of the dark matter parameter space, in terms of interaction cross section and mass.

The most relevant collider nowadays is the LHC. It is the largest and highest-energy particles collider in the world: the total center-of-mass energy can reach  $\simeq 13$  TeV. The collider has four crossing points, around which are located 4 main detectors, each designed for certain kinds of research: (i) ATLAS and (ii) CMS are both general-purpose detectors; their main aims are the Higgs physics and search for signs of new physics; (iii) ALICE is specialized for quark-gluon plasma studies, trying to understand the origin of quark masses; (iv) LHCb investigates for instance CP violation.

With the missing energy measured with big precision by ATLAS and CMS it is possible to constrain the parameter space for dark matter production. In fig. 3.10 are shown the constrained regions in parameter space  $m_\chi$  and  $m_{Z'}$  considering different kinds of events linked to dark matter production. These limits are considered with 95% CL. Notice that, however, these limits are not model-independent: as we will see in the next section, it is necessary to assume an interaction Lagrangian to describe how the dark matter interacts with the Standard Model particles, with few free parameters, which are the dark matter and mediator masses and the coupling strengths. It is possible to keep all them as free parameters; however for simplicity one usually fixes two of them as in this case both coupling strengths, keeping as free parameters both masses.

### 3.4. EXPERIMENTAL CONSTRAINS

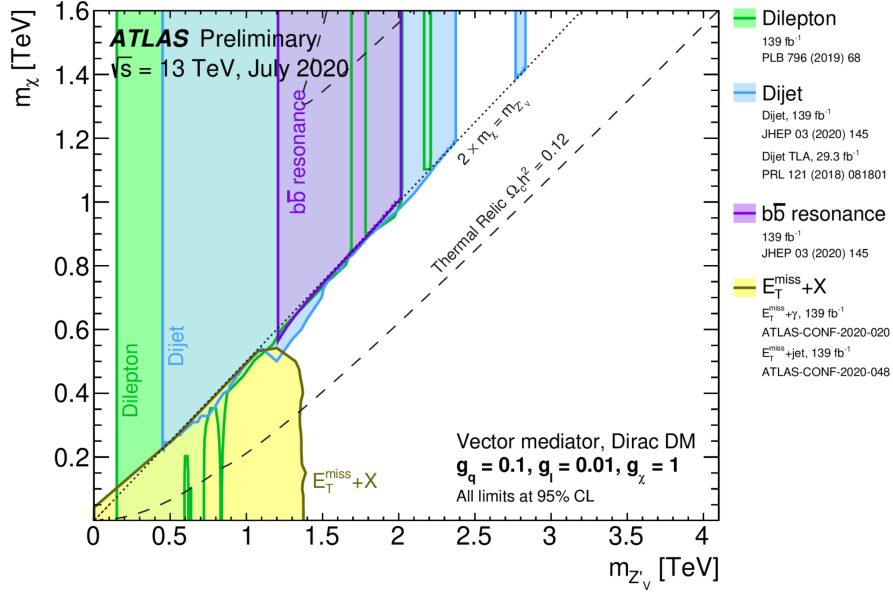


Figure 3.10: Parameter space of the dark matter and mediator masses in a  $s$ -channel simplified model, excluded by the ATLAS experiment considering different topologies, such as dilepton, dijet and  $b\bar{b}$  resonant production. The different excluded regions are labelled as in the figure. The figure is taken from [75].

# Chapter 4

## Simplified models

This chapter is the heart of the thesis. After having illustrated the necessity for dark matter in our Universe in chapter 2 and described its main features in chapter 3, we can discuss how to build viable dark matter models and compute observables to compare with the experimental data. Our main interest is towards assessing the reach of the future KM3NeT neutrino telescope on dark matter models, comparing it with other experimental constrains. In particular, we focus our attention on models where couplings with neutrinos and more in general with leptons are favoured with respect to the couplings to quarks, i.e., leptophilic models. In this case, neutrino telescopes become competitive with respect, for instance, to collider bounds, which rely on couplings to strongly interacting particles.

We introduce the idea of simplified models, a large class of models where the dark matter is a particle, and compare them to the EFT approach in sec. 4.1. We describe their main features in sec. 4.2 illustrating the philosophy and the advantages. In particular, we will discuss the Lagrangian of "spin 1-s-channel" leptophilic model in sec. 4.2 stressing its main features, such as the possibility for dark matter to annihilate into leptons and to lead to velocity independent  $\langle\sigma v\rangle$ . We analytically compute the annihilation cross-section in sec. 4.3. We then perform a numerical analysis using the MADDM package described in sec. 4.4.1 to predict the expected flux of neutrinos and gamma rays from the galactic center, a locally overdense region of dark matter, by performing scans in the model parameter space. In sec. 4.6 we discuss the results of the scans and how the current experimental data (both direct and indirect detection), described in sec. 4.5, constrain this model. Finally, we determine the reach of the future KM3NeT experiment.

In sec. 4.7 we introduce a special class of simplified models, the so-called secluded models characterized by a small coupling with the Standard Model particles. We explore two different ranges of mediator mass: first, considering its mass comparable with the dark matter mass (sec. 4.7.2) and, second, when its mass is much lighter (sec. 4.7.3). In the latter case we include Sommerfeld enhancement effects, as described in sec. 4.7.1.

In the last sec. 4.8, we discuss a consistent ultraviolet completion of the simplified

model, obtained by gauging the  $L_\mu - L_\tau$  symmetry and constrain its parameter space.

## 4.1 Simplified models vs EFT approach

Given the large number of dark matter models proposed and available in the literature, the main challenge is to identify scenarios that can produce detectable signals and be compatible with the all known constraints. The most natural dark matter candidate is a neutral and stable particle that was copiously produced in the early Universe and then decoupled from the SM thermal bath leaving a relic density compatible with measurements  $\Omega_{\text{DM}} \simeq 0.26$  [76].

There are different theoretical approaches to dark matter model building and phenomenological analyses. The EFT approach adds to the Standard Model a set of (higher-dimensional) operators, that parametrise the interaction of the dark matter particles with the Standard Model fields. In this case, the only relevant parameters are the dark matter mass,  $m_\chi$ , the strength of the couplings and the scale  $\Lambda$  to correctly normalise the higher dimensional operators [76]. The advantage of an EFT approach is its minimal model dependence (the only new state with respect to the Standard Model is the dark matter candidate). A possible downside is that having higher-dimensional operators leads to an intrinsic energy limitation, which has to be chosen  $E < \Lambda$ : at higher energies the contribution of higher dimensional operators to the scattering cross section becomes comparable to the lower order operators and the perturbative expansion is no longer valid.

Another approach to study BSM scenarios is represented by employing simplified dark matter models. These models are characterized by the introduction of two states, the dark matter candidate and a mediator that is responsible of the interaction between the dark matter sector and the Standard Model. These models are still somewhat minimal, but are typically (even though not always) characterised by a larger set of parameters with respect to an EFT. In general, simplified models are also predictive/flexible enough to provide detectable signals on the one hand, and to respect the known observational constraints.

Most of the simplified models considered in the literature can be understood as a minimal description of the lowest lying states of a more general and richer scenario, possibly with a larger spectrum of particles, and therefore can be embedded in a more fundamental theory. They also offer a generalisation of the EFT approach, as by requiring the mediator mass to be large, simplified models reduce to EFTs whose couplings are fully determined by the underlying simplified model parameters. In this respect, the two approaches are not really independent and can be also used at the same time. For instance, while resonances can be important in determining the annihilation cross section and relic density of the dark matter, resonances could be integrated out in direct detection predictions and directly use the corresponding EFT. It is worth noting,

however, that similarly to the EFT, also the simplified models might lead to unitarity violating behaviours at high energy and might need an ultraviolet completion. In any case, being easy to use and encompassing the EFT approach, they remain among the preferred choices to explore the reach of present of future experiments.

## 4.2 Model building and motivations

The starting point for constructing a simplified model is the Standard Model Lagrangian, complemented with a dark matter field and a mediator that couples to both the dark matter field and Standard Model fields through renormalizable interactions. Distinct types of simplified models can be built, considering different quantum numbers (spin, charges) for both the dark matter particles and the mediator particles and their couplings which are all free parameters associated with the model.

By studying the set of tree-level diagrams with all possible combinations of charged and flavour conserving renormalizable dimension-four operators compatible with Lorentz invariance, one is able to explore different types of dark matter models [6].

For the dark matter particle and the mediator any allowed combination of spin 0, 1/2 and 1 can be considered and the interactions can have the following general form

$$\mathcal{L}_s \supset (\overline{\text{DM}} \text{DM mediator}) + (\overline{\text{SM}} \text{SM mediator}), \quad (4.1)$$

$$\mathcal{L}_t \supset (\overline{\text{DM}} \text{SM mediator}) + h.c., \quad (4.2)$$

where DM and SM stay for dark matter and Standard Model particles respectively and two subscripts  $s$  and  $t$  label two different channels. Configurations as in eq. 4.1 arises in scenarios in which the dark matter stability is guaranteed by a  $\mathbb{Z}_2$  symmetry, a discrete symmetry under which all Standard Model fields and the mediator are even while the dark matter particle is odd [77]. In  $t$  channel case in eq. 4.2 the annihilation of dark matter particles occurs through the exchange of a charged mediator which is also even under the  $\mathbb{Z}_2$  symmetry; in this case the mediator mass is conventionally chosen to be higher than the dark matter mass, otherwise the mediator would become the dark matter itself.

Vertices describing the interactions, on the other hands, can be: (i) scalar  $\mathbf{1}$ , (ii) pseudoscalar  $\gamma^5$ , (iii) vector  $\gamma^\mu$  and (iv) axial vector  $\gamma^\mu \gamma^5$ . One needs then to understand which combination of spins and interactions are allowed by the observations.

For our purpose, we look at velocity averaged cross section  $\langle \sigma v \rangle$ : to bring it in an observable range, it is necessary to require that the dark matter is a thermal relic whose annihilation proceed largely through  $s$ -waves processes. Any other partial wave would be suppressed today and could not lead to any observable flux [5]. For  $s$ -waves,  $\langle \sigma v \rangle$  is velocity independent while in case of  $p$ -waves,  $\langle \sigma v \rangle$  suppression is proportional to  $v^2$ .

Which combinations of dark matter and mediator spins allow  $\langle\sigma v\rangle$  independent on  $v$  in the simplified models?

For the case of  $s$ -channel, it can be shown [5, 6] that unsuppressed terms are those with a Dirac fermion dark matter and scalar or vector mediators, with both vector and axial couplings in first case and only pseudoscalar for the second; notice that in these cases, if the mass of the mediator is less than that of the dark matter particles, annihilation could potentially be dominated by the production of mediator pairs rather than annihilation into Standard Model particles. With scalar dark matter, there can be only scalar and pseudoscalar interactions with Standard Model fermions as well as with vector dark matter.

For the  $t$ -channel there can be the following cases: Dirac fermion dark matter and a vector or scalar mediator, vector dark matter and Dirac fermion mediator.

Once we have specified the annihilation properties of the simplified models, it is possible to fix the interaction couplings with the Standard Model species, according to the study we want to perform. For instance the mediator can couple to all Standard Model fermions, or to leptons only (leptophilic models) or to quark only (leptophobic models).

All these models can be studied considering different combinations of masses and couplings, provided they produce viable dark matter scenarios. For each point in parameter space, it is possible to compare the theoretical predictions with the results of direct, indirect and collider searches.

### 4.3 Spin 1-s-channel mediator

In this thesis, we consider the simplified model "spin 1-s-channel mediator" where the dark matter is composed by a single species.

The dark matter particle  $\chi$  with mass  $m_\chi$  is a Dirac fermion, singlet under Standard Model gauge group  $SU_C(3) \times SU_L(2) \times U_Y(1)$ ; we consider its mass up to 10 TeV, comparable with the expected WIMP mass scale.

The mediator is a boson with spin 1, a  $Z'$ , belonging to a new group  $U'(1)$ . Its mass,  $m_{Z'}$ , is non zero. We do not discuss the mechanism through which the  $Z'$  acquires a mass. Nevertheless, let us mention that the  $Z'$  can become massive through the spontaneous breaking of the  $U'(1)$  symmetry with the introduction of a scalar field. We assume that this new scalar field is not relevant for our phenomenology, because it is very heavy. Another possibility to generate  $m_{Z'}$  is to leave the symmetry unbroken and introduce it via the Stueckelberg mechanism [78]. The "spin 1-s-channel mediator" model is one of the simplest possible extensions of the Standard Model featuring an additional gauge boson.

As we have seen in sec. 4.2, this kind of model leads to a velocity in dependent  $\langle\sigma v\rangle$ : the annihilation proceeds largely through  $s$ -waves. As mentioned earlier, in this

thesis we consider leptophilic models because we are interested in making predictions to assess the reach of the future KM3NeT neutrino telescope to leptonic annihilation signals, especially neutrino lines.

The Lagrangian of the model can be written as

$$\mathcal{L} = \mathcal{L}_{\text{SM}} + \mathcal{L}_{\text{DM}} + \mathcal{L}_{Z'}, \quad (4.3)$$

where the three terms are the Lagrangians of the Standard Model, of the dark matter and of the vector boson mediator respectively. Expliciting the Lagrangian in eq. (4.3) for the Dirac fermion  $\chi$  and the massive boson  $Z'$ , one obtains

$$\mathcal{L} = \mathcal{L}_{\text{SM}} - \frac{1}{4} F'^{\mu\nu} F'_{\mu\nu} + \frac{1}{2} m_{Z'}^2 Z'^{\mu} Z'_{\mu} + \bar{\chi}(i\not{\partial} - m_{\chi})\chi + J_{\text{DM}}^{\mu} Z'_{\mu} + J_{\text{SM}}^{\mu} Z'_{\mu}, \quad (4.4)$$

with the following definitions

$$F'_{\mu\nu} = \partial_{\mu} Z'_{\nu} - \partial_{\nu} Z'_{\mu}, \quad (4.5)$$

for the field strength tensor of the massive boson and

$$\begin{aligned} J_{\text{DM}}^{\mu} &= \bar{\chi} \gamma^{\mu} (g_{\text{DM}}^V + \gamma^5 g_{\text{DM}}^A) \chi, \\ J_{\text{SM}}^{\mu} &= \sum_i \bar{l}_i \gamma^{\mu} (g_{\text{SM}}^V + \gamma^5 g_{\text{SM}}^A) l_i, \end{aligned} \quad (4.6)$$

for the interaction terms; the index  $i$  runs over the sum of all the Standard Model leptons. This Lagrangian can be extended to quarks in a similar manner; however, being interested in leptophilic scenarios, we refrain from adding interactions with quarks.

Notice that the  $Z'$  is treated analogously to the  $Z$  gauge boson of the Standard Model: we are using a generalisation of universality of weak interactions, considering all leptons coupled with the same coupling strength, i.e. coupling  $g_{\text{SM}}$  is generation independent. Indeed, if we had used a Yukawa-like coupling and a scalar mediator we would have obtained the dependence on the type of particles, being the coupling different for the various flavours.

Considering vector and axial-vector models, if the interaction mediated via  $Z'$  does not respect the gauge invariance perturbative unitarity may be violated. In particular, if the couplings to the two components of a doublet of Standard Model leptons are different,  $SU_L(2)$  gauge symmetry is not respected. To restore the unitarity, the  $Z'$  then has to be embedded in a new  $U'(1)$  gauge group. To break this gauge group and give a mass to the  $Z'$  one should introduce a dark Higgs singlet  $S$  [79]. The Lagrangian then has a new term  $\mathcal{L}_S$  which represents the extended Higgs sector. However, our intention here is not to fit the parameters of a complete model, but rather to study the minimal set leading to an interesting phenomenology.

One then can consider pure vector interactions i.e.  $g_i^A = 0$  ( $i = \text{DM, SM}$ ); however, in this case the branching ratio of particles is not equal for all the leptons. Indeed, if  $g^A = 0$ , then right-handed charged leptons are considered as well

$$\mathcal{L} \supset g_{\text{SM}} Z'_\mu [q_L \bar{l}_{i,L} \gamma^\mu l_{i,L} + q_R \bar{l}_{i,R} \gamma^\mu l_{i,R}] \quad i = 1, 2, 3, \quad (4.7)$$

with  $l_i$  lepton doublet. This behaviour might be a problem for our purposes as we are looking for scenarios where the cross section for neutrinos is enhanced. To obtain the same branching ratio for annihilation into charged leptons or neutrinos, the couplings must be both vector and axial. We can redefine the couplings in following way

$$g_{\text{SM}}^V = \frac{1}{2} g_{\text{SM}} (q_R + q_L), \quad g_{\text{SM}}^A = \frac{1}{2} g_{\text{SM}} (q_R - q_L). \quad (4.8)$$

Choosing then  $q_R = q_L$ , we have the same branching ratios, and all the contributions are written in a vector like form. From now on, we consider  $g_{\text{SM}}^V = g_{\text{SM}}$ .

It should be noted that the model allows for the following term

$$\mathcal{L} = -\frac{1}{2} \sin \epsilon F'^{\mu\nu} B_{\mu\nu}, \quad (4.9)$$

which generates a kinetic mixing between the  $Z'$  and  $B$  hypercharge gauge boson of the Standard Model [79]. Even if at the tree level the kinetic mixing is assumed to be negligible, this mixing term is necessarily generated at the one-loop level and might induce relevant effects in the phenomenology of the model, as we show later.

Considering the Lagrangian in eq. (4.4), we can have two different annihilation processes for the dark matter particles, represented via the Feynman diagrams in fig. 4.1. While the process associated to the left-hand side Feynman diagram is always possible because the boson is virtual, the Feynman diagram on the right-hand side represents the annihilation of the dark matter particle in two bosons which, being metastable, will further decay into Standard Model particles. The dominant contribution comes when the process is kinematically allowed, i.e. when  $m_\chi \geq m_{Z'}$ .

We now compute the total velocity averaged cross section. To obtain it, we firstly compute the annihilation cross section for both the processes and after we multiply the obtained result by  $v$ . Notice that for our purpose we consider all the leptons massless because we are working at much higher energies with respect to their mass scale. This assumption is kept all along our analysis, except for the case when the  $Z'$  is considered very light.

In the non-relativistic limit, the velocity of a particle with momentum  $\vec{k}$  and energy  $k_0$  is

$$v_k = \frac{|\vec{k}|}{k_0} \approx \frac{|\vec{k}|}{m_\chi} \ll 1. \quad (4.10)$$

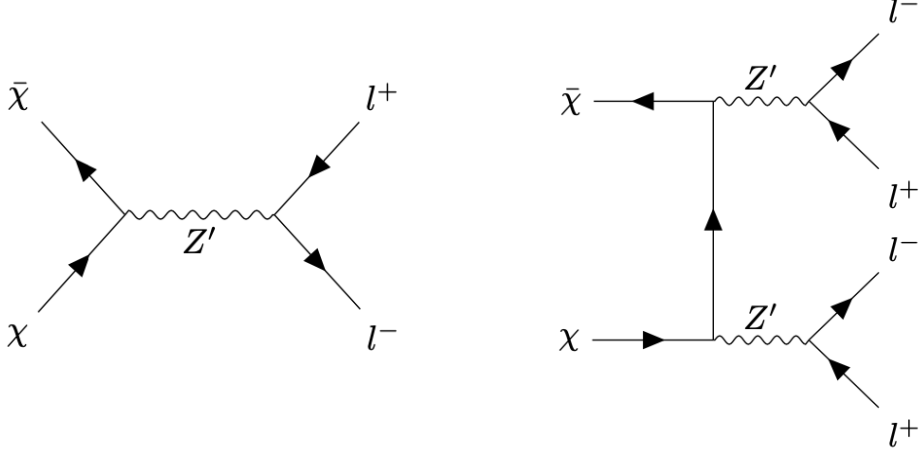


Figure 4.1: Tree-level Feynman diagrams describing the dark matter annihilation into Standard Model leptons through a  $Z'$  vector boson mediator. The left one has two lepton final states while the right one represents the annihilation of dark matter into intermediate bosons which decay subsequently into Standard Model particles.

The external momenta of the two fermions can be written as

$$k^2 = k_0^2 - \vec{k}^2 = k_0^2 - (m_\chi v_k)^2 \iff k_0 = \sqrt{m_\chi^2 + m_\chi^2 v_k^2} \approx m_\chi \left(1 + \frac{v_k^2}{2}\right). \quad (4.11)$$

For a  $2 \rightarrow 2$  process we need to distinguish between the velocities of individual particles and their relative velocity  $v$ . The energy of the initial state is  $s = (p_1 + p_2)$ . For incoming particles with the same mass, one obtains

$$s = (p_1 + p_2)^2 = 4m_\chi^2(1 + v_1^2), \quad (4.12)$$

and

$$m_\chi^2 v^2 = 4m_\chi^2 v_1^2 = s - 4m_\chi^2. \quad (4.13)$$

The relative velocity of the two incoming particles in the non-relativistic limit is

$$v = \left| \frac{\vec{k}_1}{k_1^0} - \frac{\vec{k}_2}{k_2^0} \right|, \quad (4.14)$$

that in centre-of-mass reference frame is just

$$v = 2v_1 \iff m_\chi^2 v^2 = 4m_\chi^2 v_1^2 = s - 4m_\chi^2. \quad (4.15)$$

Finally

$$v = 2v_1 = 2\sqrt{\frac{s}{4m_\chi^2} - 1}. \quad (4.16)$$

We can expand the averaged annihilation cross section as

$$\langle \sigma_{\chi\chi} v \rangle = \sigma_{\chi\chi} v + \mathcal{O}(v^2) \quad (4.17)$$

The velocity averaged cross section for the left diagram of fig. 4.1 is

$$\langle \sigma v \rangle (\chi\bar{\chi} \rightarrow l\bar{l}) = \frac{g_{\text{SM}}^2 g_{\text{DM}}^2}{\pi} \frac{m_\chi^2}{(4m_\chi^2 - m_{Z'}^2)^2 + m_{Z'}^2 \Gamma^2}. \quad (4.18)$$

The decay width  $\Gamma$  of the  $Z'$  is

$$\Gamma = \frac{m_{Z'} g_{\text{SM}}^2}{12\pi} \left(1 - \frac{4m_l^2}{m_{Z'}^2}\right)^{1/2} \left(1 + \frac{2m_l^2}{m_{Z'}^2}\right) + \frac{m_{Z'} g_{\text{DM}}^2}{12\pi} \left(1 - \frac{4m_\chi^2}{m_{Z'}^2}\right)^{1/2} \left(1 + \frac{2m_\chi^2}{m_{Z'}^2}\right). \quad (4.19)$$

Repeating the same steps for the right-hand side Feynman diagram of fig. 4.1, one obtains as leading contribution

$$\langle \sigma v \rangle (\chi\bar{\chi} \rightarrow Z'Z') \simeq \frac{g_{\text{DM}}^4}{32\pi} \frac{(m_\chi^2 - m_{Z'}^2)^{3/2}}{m_\chi (2m_\chi^2 - m_{Z'}^2)^2}. \quad (4.20)$$

Notice that the last result is independent from  $g_{\text{SM}}$ : as we will see in sec. 4.7 this kind of model is called secluded. It is secluded because the coupling with the Standard Model can be taken to be very small while the relic density of the dark matter is governed by the coupling strength  $g_{\text{DM}}$ , which can have sizeable values. Notice that both of annihilation cross sections are velocity independent, as we pointed out in sec. 4.3.

These results have been cross-checked with MATHEMATICA using the FEYNARTS [80] and FEYNCALC [81] packages. These results are additionally in agreement with the findings of refs. [82, 83].

## 4.4 Numerical tools

The aim of this section is a brief illustration of the numerical tools we used for this thesis. To compute  $\langle \sigma v \rangle$ , do analysis of energy spectra and find the Fermi limits on the velocity averaged cross section, we have used MADDM.

As we have seen in sec. 4.3, our model is leptophilic, i.e. it does not have coupling with quarks and no tree level processes are allowed. However, being MADDM currently unable to handle loop processes, for the dark matter-Nucleon cross section we have used RUNDM in order to find the interaction spin-independent cross section.

### 4.4.1 MadDM

In the last decade, several tools and frameworks have been proposed and developed with the purpose of computing dark matter model predictions for relic density, direct and indirect detection observables: MICROMEGAS [84], DARKSUSY [85] just to cite some of them. In this work we have used for numerical simulations MADDM.

MADDM [7] is a numerical tool to compute dark matter observables within generic Universal FEYNRULES Output (UFO) models. UFO models for dark matter can be obtained using the FEYNRULES package [86], which computes the Feynman rules for generic physics models. It is enough to load in the package two separate documents in the .fr format, one describing the Standard Model Lagrangian and one for dark matter Lagrangian. The latter contains the description of the new fields, new couplings and new interaction terms. FEYNRULES merges the two files, computes the Feynman rules and provides them in the complete UFO output that is suitable for various high energy tools: one of this is MADDM. Model files, including different models for dark matter studies, can be downloaded from the FEYNRULES website.

MADDM provides a simple, user-friendly and all-in-one dark matter phenomenology framework. It can be used by experimentalists and theorists to calculate accurate signatures of generic dark matter models for indirect, direct and collider searches.

Its first release [87] provided the possibility to compute the relic density, considering a certain dark matter model. In its second release [88] the computation of dark matter-nucleon cross section for direct detection was added. The last version [7] implements indirect detection module, which allows the computation of several observables for indirect detection. In addition, it is possible to have theoretical predictions for the velocity averaged cross section at present time, generate energy spectra from dark matter annihilation and compute fluxes at source. Being a plug in of MG5AMC [89], MADDM inherits most of its architecture, including its matrix element generator which allows to compute automatically the energy spectra for dark matter annihilation into generic  $n$  final states [7]. For the computation of  $\langle\sigma v\rangle$ , MADDM uses the MG5AMC's event generator MADEVENT [90]. The energy spectra of gamma rays, positrons, antiprotons and neutrinos coming from dark matter annihilation can be determined via the parton level event generation and then passing these events through PYTHIA8 [91] for showering and hadronization; this is called the 'precise running mode' of MADDM. There is as well a 'fast mode' downloading PPPC4DMID [92] numerical tables and then the energy spectra of the model are interpolated using those tables.

Moreover, MADDM incorporates a simplified functionality for testing model points against experimental constraints for direct and indirect experimental constraints. For indirect detection, MADDM has implemented Fermi-LAT likelihood for prompt  $\gamma$ -rays while, for what concerns direct detection, for direct detection MADDM considers the following limits: XENON1T [9] and LUX [93] for spin-independent dark matter-Nucleon interaction and LUX [94] and Pico60 [95] for spin dependent cross section.

Notice that MADDM can compute annihilation cross section for direct detection and velocity averaged cross section for indirect detection only at the tree level.

### 4.4.2 runDM

As our model does not have any coupling to quarks, it is not possible to have any process contributing to the scattering cross-section between dark matter particles and the nucleons. However, this interaction is possible at loop-level, once one considers the mixing terms between the  $Z'$  and the neutral Standard Model gauge bosons  $\gamma$  and  $Z$  or an EFT approach.

The connection between simplified model valid at high energy with its non relativistic manifestation at the nuclear level is non trivial. Such a scale connection can be achieved by employing techniques from an EFT framework, performing a Renormalization Group Evolution (RGE) of the dark matter interactions [96].

The RGE introduces mixing between different dark matter-Standard Model interactions, affecting the size of the couplings or even introducing new coupling arising via Standard Model loops.

At two different scales, the theory looks quite different and the connection between simplified models and EFT at low energies can be achieved in two steps: integrating out the mediator and doing RGE down to the nuclear scale. The mediator is integrated out because its mass usually is significantly larger than the momentum exchanged in direct detection processes. Moreover, the interaction between the dark matter and Standard Model can be described in terms of a dimension 6 operator

$$\mathcal{L}_{\text{EFT}} = -\frac{J_{\mu\text{DM}}J_{\text{SM}}^{\mu}}{m_{Z'}^2}, \quad (4.21)$$

where the currents are those specified in eq. (4.6). The couplings obtained from eq. (4.21) are defined at the energy scale  $m_{Z'}$  and have to be evolved down to the nuclear scale. Through this procedure one obtains the description of the interactions between quarks and dark matter. Finally one has to embed the dark matter interactions with quarks at the nuclear level. The effective Lagrangian for the nucleon field is

$$\mathcal{L}_N = -\frac{J_{\text{DM}}^{\mu}}{m_{Z'}^2} [\mathcal{C}_V \bar{N} \gamma^{\mu} N + \mathcal{C}_A \bar{N} \gamma^{\mu} \gamma^5 N], \quad (4.22)$$

where  $N$  stands for nucleon, proton ( $p$ ) or neutron ( $n$ ). The coefficients have the following form

$$\begin{aligned} \mathcal{C}_V^{(p)} &= 2\mathcal{C}_V^{(u)} + \mathcal{C}_V^{(d)}, \\ \mathcal{C}_V^{(n)} &= \mathcal{C}_V^{(u)} + 2\mathcal{C}_V^{(d)}. \end{aligned} \quad (4.23)$$

The total dark matter-nucleon cross section for the Lagrangian in eq. (4.22), for both spin dependent (SD) and spin independent (SI) interactions [96], is

$$\sigma_{\text{SI}}^N = \frac{\mu_N^2}{\pi} \frac{(c_{\chi V} \mathcal{C}_V^N)^2}{m_{Z'}^4}, \quad (4.24)$$

$$\sigma_{\text{SD}}^N = \frac{3\mu_N^2}{\pi} \frac{(c_{\chi A} \mathcal{C}_A^N)^2}{m_{Z'}^4}, \quad (4.25)$$

where  $\mu_N$  is the dark matter-nucleon reduced mass i.e.  $\mu_N = m_\chi m_N / (m_\chi + m_N)$ .

Equation (4.23) can be computed with the RUNDM [97, 98, 96] function called DD-CouplingsQuarks. After specification of the couplings for the interactions, the running is performed down to the nuclear energy scale of 1 GeV and this function returns a vector of the low-energy coupling to light quarks  $u, d$  and  $s$ . These couplings are namely

$$\mathcal{C}_q = \left( C_V^{(u)}, C_V^{(d)}, C_A^{(u)}, C_A^{(d)}, C_A^{(s)} \right). \quad (4.26)$$

Taking the first two element of the above array evaluated for each value of mediator mass and plugging them into eq. (4.23), we finally obtain eq. (4.24) and eq. (4.25).

For our purpose we have considered only spin independent cross section and we will compare it to the experimental bounds of XENON1T. We considered only spin-independent cross section because we are considering a pure vector model; as we have shown in sec. 3.3.2, spin dependent cross section arises only once axial-vector current is considered as well.

## 4.5 State of the art of the experimental constraints

The aim of this section is the introduction of experimental bounds that we have considered for both indirect and direct detection.

For the indirect detection we used three different constrains: Fermi-LAT data, future KM3NeT from [12] which we label as KM3NET(1), KM3NET limits described in [11] which is indicated by KM3NET(2) and for the direct detection we used XENON1T data.

For the first constrain we have used MADDM which provide likelihood for diffuse gamma rays from dSPhs which are optimal targets to test the hypothesis of annihilating dark matter in galactic halo. The analysis implemented in MADDM is based on the public data released by Fermi-LAT collaboration [99]. MADDM finds the 95% CL cross section upper limit for a given model point. Its likelihood method to compare theoretical predictions with the Fermi-LAT data is very generic and can constrain any dark matter model [7].

KM3NeT (2) are obtained considering 11 years of data taken with the ANTARES neutrino telescope. Computing the test statistic of the data after having re-assigned

the real coordinates to each event in [12] was obtained an upper limit on  $\langle\sigma v\rangle$  with a sensitivity defined as the 90% CL. In particular, for our analysis we have considered sensitivities of a first sub-block of KM3NeT-ARCA with 2 blocks of 115 lines for NFW profile with 1 year of effective lifetime.

KM3NeT (2) are obtained considering angular power spectrum (APS) of simulated neutrino sky maps for the neutrino telescope adopting NFW profile. For our purpose we have considered upper limits with 90% CL.

XENON1T exclusion limit on the spin-independent dark matter-nucleon interaction with a 90% CL are taken from [9].

## 4.6 Spin 1-s-channel results

In sec. 4.3 we have illustrated our  $s$ -channel simplified model and we have motivated our choice for leptophilic model. Now we want to sample the model parameter space by varying the free parameters of our theory, which are  $m_\chi$ ,  $m_{Z'}$ ,  $g_{\text{SM}}$  and  $g_{\text{DM}}$ . In particular, we fix  $g_{\text{DM}} = 1$  and  $g_{\text{SM}} = 1$ , considered universal for all flavours of leptons, and we vary the mass parameters to compute  $\langle\sigma v\rangle$ . We further complement the study by confronting the scan with the experimental constrains described in sec. 4.5.

The simulations for the theoretical predictions have been done with MADDM, as described in sec. 4.4.1. We have performed a scan grid for the following mass ranges:  $[191 - 10^5]$  GeV for dark matter mass, and  $[100 - 10^5]$  GeV for the mediator mass. MADDM provides the computation of  $\langle\sigma v\rangle$  using MADEVENT. In addition, the energy spectra at source are computed using the PPPC4DMIDew [92] table interpolation. These tables provide the energy spectra with the electroweak corrections described in sec. 3.3.1.

Being the branching ratio the same for all final leptons, we considered  $6 \cdot \langle\sigma v\rangle_{l\bar{l}}$  for the total velocity averaged cross section, where  $l$  is a single lepton. Few considerations can be done by looking at fig. 4.3. The 2D panel shows the values of  $\langle\sigma v\rangle_{\text{max}}$  chosen for each value of  $m_\chi$ , varying different masses of  $m_{Z'}$ . These values are represented via the continuous bordeaux line. This line is bumpy because it follows the resonance region. The value of  $\langle\sigma v\rangle$  decreases with increasing  $m_\chi$ , as one expects. They are compared with the experimental constrain of Fermi-LAT and predictions for the future KM3NeT as described in sec. 3.4 labelled as in figure. We can find three intersection points between line of  $\langle\sigma v\rangle_{\text{max}}$  and those representing Fermi-LAT constrain and predictions for the future KM3NeT: (i)  $m_\chi = 2$  TeV corresponding to intersection with Fermi-LAT,  $m_\chi = 3.7$  TeV corresponding to intersection with KMENeT(2) and  $m_\chi = 16.1$  TeV for intersection with KM3NeT(1). Considering these points, one can conclude that while Fermi-LAT limits on  $\langle\sigma v\rangle$  can exclude dark matter masses up to 2 TeV, the future KM3NeT is more promising. Indeed, KM3NeT(1) can constrain  $m_\chi$  up to 16.1 TeV and KM3NeT(2) up to 3.7 TeV.

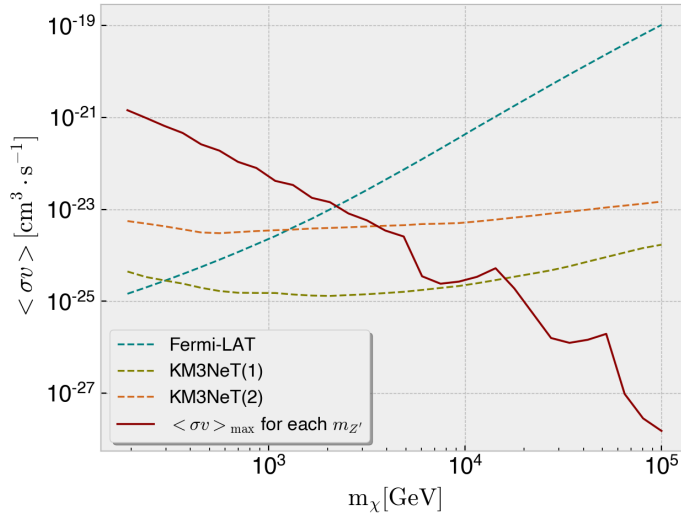


Figure 4.2: 2D plot representing the Fermi-LAT constrain and future predictions for KM3NeT we have considered for our analysis in the plane  $\langle \sigma v \rangle$  and  $m_\chi$ , as labelled. The experimental bound and projections are compared with the value of  $\langle \sigma v \rangle_{\text{max}}$  for each value of  $m_{Z'}$  (bordeaux solid line). This line is bumpy because it follows the resonance region.

The left panel of fig. 4.2 illustrates the  $\langle \sigma v \rangle$  behavior as a function of  $m_\chi$  and  $m_{Z'}$  through a colormap. The central region on the panel is dominated by the enhancement due to the resonance. As expected according (4.18),  $\langle \sigma v \rangle$  values are larger for smaller mass of both  $\chi$  and  $Z'$ ; it decreases for small values of  $m_\chi$ -large values of  $m_{Z'}$  and for mirrored-case as well. Black lines are added just to have a reference. The right figure represents the experimental exclusions/predictions. Different regions of the plot are excluded by experimental bounds labelled in the figure; both direct and indirect data are considered. The main portion of parameter space is excluded by XENON1T which incorporate regions excluded by Fermi-LAT and in the range of exploration of KM3NeT(2). KM3NeT(1) will be still promising, being able to constrain regions with dark matter mass up to 6.8 TeV and boson mass up to 12 TeV.

## 4.7 Secluded WIMP dark matter

The secluded dark matter scenario regards models in which dark matter particles annihilate into a pair of non-Standard Model mediators, which subsequently decay into Standard Model particles, differently from the previous situation. This model is the second case of simplified model described in sec. 4.3 and is motivated with the same

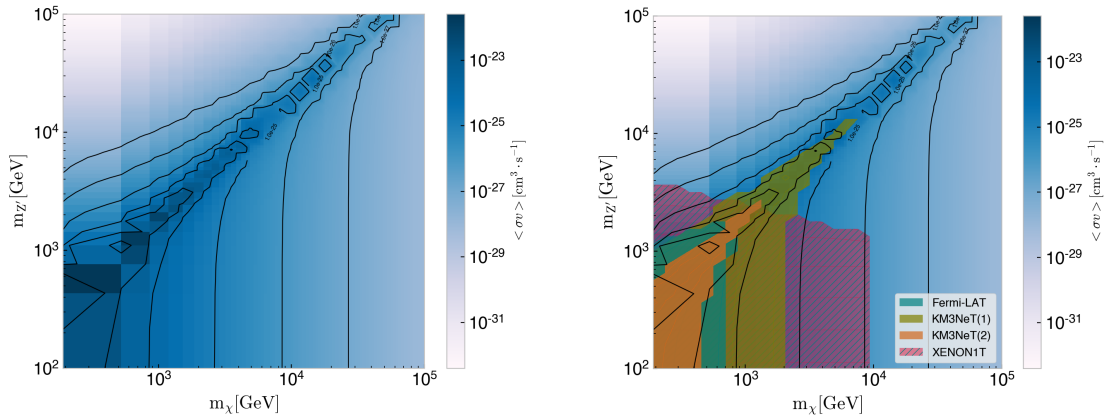


Figure 4.3: **spin-1-s-channel:  $2 \rightarrow 2$  case** The left panel represents the velocity averaged cross section  $\langle\sigma v\rangle$  as a function of  $m_\chi$  and  $m_{Z'}$ . Black lines represent different numerical values for  $\langle\sigma v\rangle$  for sake of reference. The left panel figure shows the experimental exclusions on the averaged cross section for the annihilation of dark matter particles into leptons. Experimental constrains are labelled as in figure. Large region of parameter space is excluded by XENON1T data and by KM3NeT (1) prediction which overwrites both Fermi-LAT limit and KM3NeT (2) prediction.

reasons.

The secluded models aim at analyzing the parameter space characterised by  $m_\chi > m_{Z'}$  and  $g_{\text{SM}} \ll 1$ . The first requirement guarantees kinematically allowed region of the parameter space for the process in fig. 4.1 i.e.  $\chi\bar{\chi} \rightarrow Z'Z'$ , with the mediator bosons being on shell but metastable because of a non zero coupling with the Standard Model particles. The second condition is dictated by the requirement of not spoiling the predictions of BBN. In fact, the mediator lifetime should be shorter than 1s in order to guarantee its decay before the beginning of BBN. Otherwise it would inject energy into the thermal bath and delay the formation of the primordial nuclei. This however does not provide strong constraints on  $g_{\text{SM}}$ , as we will show later.

The assumption of having  $g_{\text{SM}} \ll 1$  allows the dark matter sector to be secluded from the Standard Model in a natural way, thanks to a very small cross-section for direct detection and collider searches. Actually, the reduction of the coupling of the dark matter and Standard Model suppresses the collider and direct detection rates by many orders of magnitude, because they scale as  $g_{\text{SM}}^2$ .

In contrast, indirect detection signatures from dark matter annihilation are consistent with a small  $g_{\text{SM}}$ , because eventually the  $Z'$  boson will decay and provide potentially observable signals.

We have considered the same conditions as for the generic simplified model described in sec. 4.3: fermionic dark matter annihilating in a pair of mediators that decay sub-

sequently in leptons with couplings  $g_{\text{SM}}$ . This process is described via the Feynman diagram in fig. 4.1 (right panel).

The annihilation averaged cross section  $\langle\sigma v\rangle$  which is described with eq. (4.20), depends on  $g_\chi^4$  and we have to take it up to perturbative limit i.e.  $g_\chi = 4\pi$ . Moreover,  $\langle\sigma v\rangle$  is independent on  $g_{\text{SM}}$  and for this reason we can choose it as small as we desire. This is the main advantage of the secluded models. To fix the coupling with the Standard Model, one looks at the expression of the decay width  $\Gamma$  in eq. (4.19) and requires that the decay width is less than 1 s for the reasons we explained before. Being the lifetime of  $Z'$  the inverse of  $\Gamma$ , one obtains

$$\tau \lesssim 1 \text{ s} \quad \rightarrow \quad g_{\text{SM}} \gtrsim 10^{-13}. \quad (4.27)$$

which is the upper bound, requiring the minimum value of  $m_{Z'}$ , for our case it is 100 GeV. To illustrate the phenomenology of this simplified secluded model, we consider two different scenarios:

- $m_\chi \simeq m_{Z'}$  in the mass range GeV – TeV;
- $m_\chi \ll m_{Z'}$ : a boson mediator significantly lighter than the dark matter particle. In this case we have considered the Sommerfeld enhancement, described in the next section, because of the significant gap between the mediator and dark matter masses.

The experimental limits described in sec. 3.4 are included in both the considered cases.

### 4.7.1 Sommerfeld enhancement

The theory of the Sommerfeld enhancement was developed by Arnold Sommerfeld [100]. The Sommerfeld enhancement plays an interesting role when a light force carrier is present in a theory. If there is an attractive (repulsive) interaction, creating a Yukawa potential, the mediator, in fact, can distort the wave function of the incoming particles away from the plane-wave approximation, yielding significant enhancement (or suppression) to annihilation cross section [101]. Including Sommerfeld enhancement, the left Feynman diagram of fig. 4.1 must be modified in the left panel of fig. 4.4.

Although annihilation of dark matter in early Universe and nowadays is determined by the same particle physics processes, the kinematics is very different in terms of velocity. As the Universe continues to cool down after the dark matter freeze-out, its velocity decreases. In fact, at freeze out, thermal relics have velocity  $v \simeq 0.3c$  while today the velocity is estimated near the value  $v \simeq 10^{-3}c$ . One of the consequences is that the numerical values of the annihilation cross section may be different, if  $\langle\sigma v\rangle$  depends on  $v$ , because of the Sommerfeld effect.

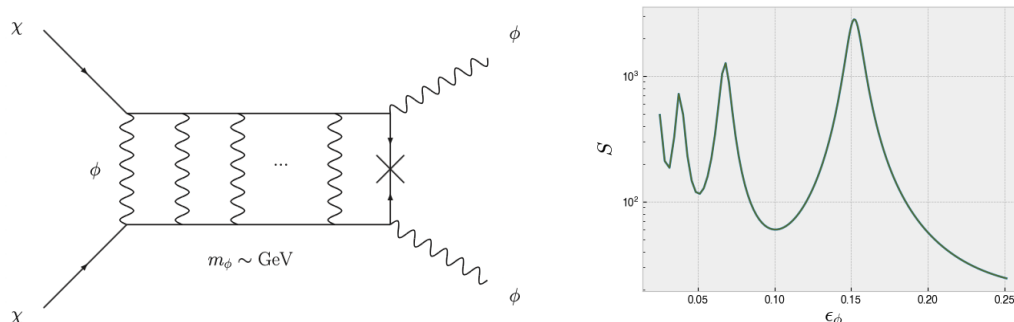


Figure 4.4: The left panel represents the Feynman diagram describing annihilation of dark matter including Sommerfeld effect; the right panel is an illustration of the Sommerfeld enhancement factor  $S$  as a function of  $\epsilon_{Z'} = m_{Z'}/(\alpha_\chi m_\chi)$ , keeping constant the value of  $\epsilon_v = v/\alpha_\chi$ . Considered mass ranges are  $[500 - 5000]$  GeV and  $[1 - 100]$  GeV for  $\chi$  and  $Z'$  respectively and as coupling  $g_\chi = 1$

We will see that the Sommerfeld enhancement is proportional to the velocity of dark matter particles

$$S \propto \frac{1}{v}. \quad (4.28)$$

This means that for dark matter freeze out at early times the Sommerfeld effect is negligible and the thermal cross section is  $\langle \sigma v \rangle_0 \simeq 3 \cdot 10^{-26} \text{ cm}^3/\text{s}$ ; nowadays the Sommerfeld enhancement should be included because, being inversely related with  $v$ , it gives a significant contribution.

For our model, thermal annihilation cross section in the early Universe at tree level is dominated by  $s$ -wave processes as we point out in sec. 4.2, i.e. it is not suppressed at low velocities being velocity independent.

To understand better the origin of the Sommerfeld enhancement, let's considering a simple example of two non-relativistic particles moving towards an annihilation zone. One can include an interacting potential affecting both the particle before the annihilation; this interaction can be parametrized with  $V(\vec{r})$ . The Sommerfeld enhancement factor  $S$  is defined as the ratio of the annihilation cross section with and without the potential  $V(\vec{r})$  is

$$S = \frac{\sigma}{\sigma_0}. \quad (4.29)$$

Being the cross sections proportional to the squared of the system wavefunction, one can explicit the above definition as

$$S = \frac{|\chi(0)|^2}{|\chi_0(0)|^2}, \quad (4.30)$$

where  $\chi$  is the wavefunction under the effect of the potential  $V(\vec{r})$  before annihilation and  $\chi_0$  is the one without the interacting potential. We are considering  $r = 0$  because the annihilation happens at zero separation. This means that to find the Sommerfeld factor, one needs to solve the Schrödinger equation including the interaction potential. The latter can take different forms depending on the mass of the mediator causing the effect, as described later.

In the simplest scenario, one has a single dark matter particle component  $\chi$  and a light force carrier  $Z'$ , with fine structure constant  $\alpha_\chi \equiv \frac{g_{\text{DM}}^2}{4\pi}$ , massless or significantly lighter with respect to dark matter mass i.e.  $m_{Z'} \ll m_\chi$ . It is possible to define two limits of Sommerfeld factor:  $S_0$  in limit of the massless force carrier, mimicking the Coulomb potential and  $S$  in limit of massive  $Z'$  with Yukawa potential.

In case of the attractive Coulomb potential one has to solve the following Schrodinger equation with the potential  $V(r) = -\frac{\alpha_\chi}{r}$ . The two body wavefunction obeys the radial Schrodinger equation [101]

$$\frac{1}{m_\chi} \chi''(r) + \frac{\alpha_\chi}{r} \chi(r) = -m_\chi v^2 \chi(r). \quad (4.31)$$

$S_0$  in the case is

$$S_0 = \frac{\pi \alpha_\chi}{1 - e^{-\pi \alpha_\chi / v}}, \quad (4.32)$$

where  $v = v_{\text{rel}}/2$  is the dark matter particle's velocity in the centre-of-mass frame [102]. In the case of Yukawa potential

$$V(r) = -\frac{g_{\text{DM}}}{4\pi r} e^{-m_{Z'} r} = -\frac{\alpha_\chi}{r} e^{-m_{Z'} r}, \quad (4.33)$$

where  $g_{\text{DM}}$  is the coupling parameter and  $m_{Z'}$  is the mass of the force carrier. One has to solve numerically Schrodinger equation with the above potential

$$\frac{1}{m_\chi} \frac{d^2 \chi}{dr^2} + \frac{\alpha_\chi}{r} e^{-m_{Z'} r} \chi = -m_\chi v^2 \chi \quad (4.34)$$

with the boundary condition  $\chi'(r) = im_\chi v \chi(r)$  and  $\chi(r) = e^{im_\chi v r}$  when  $r \rightarrow \infty$ .

The resulting analytic approximation for the Sommerfeld enhancement is

$$S = \frac{\pi}{\epsilon_v} \frac{\sinh\left(\frac{2\pi\epsilon_v}{\pi^2\epsilon_{Z'}/6}\right)}{\cosh\left(\frac{2\pi\epsilon_v}{\pi^2\epsilon_{Z'}/6}\right) - \cos\left(2\pi\sqrt{\frac{1}{\pi^2\epsilon_{Z'}/6} - \frac{\epsilon_v^2}{(\pi^2\epsilon_{Z'}/6)}}\right)}, \quad (4.35)$$

where by definition  $\epsilon_v = v/\alpha_\chi$  and  $\epsilon_{Z'} = m_{Z'}/\alpha_\chi m_\chi$ . At low velocities, the Sommerfeld factor saturates as  $S \sim 1/\epsilon_{Z'}$ . For specific values of  $\epsilon_{Z'}$ , the Yukawa potential develops threshold bound states and these give rise to resonant enhancements of the Sommerfeld

enhancement [101]. Notice that while in regions away from the resonances the enhancement is proportional to  $v^{-1}$ , near the resonances, the Sommerfeld is enhanced by a factor  $v^{-2}$ . For  $\alpha_\chi m_{Z'} \ll m_\chi v^2$ , the Yukawa potential becomes indistinguishable from the Coulomb potential and no strong resonances appear in  $S$ . This behaviour of the Sommerfeld factor is illustrated in the right panel of fig. 4.4, where is plotted  $S$  factor as a function of the parameter  $\epsilon_{Z'}$ . Notice that the  $S$  factor presents typical resonance structure: they are, for  $\epsilon_v \ll \epsilon_{Z'}$ , at

$$m_{Z'} = \frac{6\alpha_\chi m_{Z'}}{\pi^2 n^2}, \quad (4.36)$$

with  $n \in \mathbb{N}$ . At this resonances, for low  $v$ , Sommerfeld enhancement factor is given by [102]

$$S \simeq \frac{\pi^2 \alpha_\chi m_{Z'}}{6m_\chi v^2}. \quad (4.37)$$

#### 4.7.2 Secluded model: $m_{Z'} \simeq m_\chi$ case

In this section we discuss our study of the first scenario of secluded dark matter, where dark matter and mediator have comparable masses.

For this case we have considered dark matter mass in range  $[500 - 5000]$  GeV and the mass of mediator  $Z'$  in  $[200 - 2000]$  GeV. We have considered  $g_\chi = \sqrt{4\pi}$  to enhance the  $\langle\sigma v\rangle$  in the detectable range.

The numerical simulations have been made with MADDM. In this case we have used directly MG5AMC, asking the mediators decay into Standard Model leptons rather than using PYTHIA8 for  $Z'$  decay. Notice that in this case is not possible to use PPC4DMIDew because tables do not contain BSM particles.

We were not able to produce the gamma-ray energy spectra coming from the 4 leptons final state with MADDM because of numerical instabilities. Hence in order to be able to derive the Fermi-LAT upper limits for the secluded model in this scenario, we adopted the following approximation. This approximation amounts to consider a single boson with mass  $m_{Z'}$  decaying in Standard Model particles. This is a reasonable approximation given that bosons can be considered as produced at rest. We show in fig. 4.5 the energy spectra for the two cases. These distributions are for  $\gamma, \nu_e, \nu_\mu$  and  $\nu_\tau$ , obtained from a  $\mu^-$  and  $\mu^+$  final state from dark matter annihilation. The continuous lines represent the energy spectra for  $\nu_e, \nu_\mu, \nu_\tau$  and  $\gamma$ , coming from  $\chi\bar{\chi} \rightarrow \mu^+\mu^-$  and the dashed lines those coming from subsequently decaying of  $Z'Z'$  into 4 muons. In the first case we considered  $m_\chi = 10$  TeV and  $m_{Z'} = 9800$  GeV while in the second one we considered  $m_{Z'} = 4900$  GeV. For both the cases we have used PYTHIA8 and we required  $5 \cdot 10^5$  events.

This approximation is adequate for  $\gamma$  and  $\nu_\tau$  energy spectra. For  $\nu_e$  and  $\nu_\mu$  it can be considered valid as long as  $X \simeq 0.0025$  or  $K \simeq 24.5$  GeV.

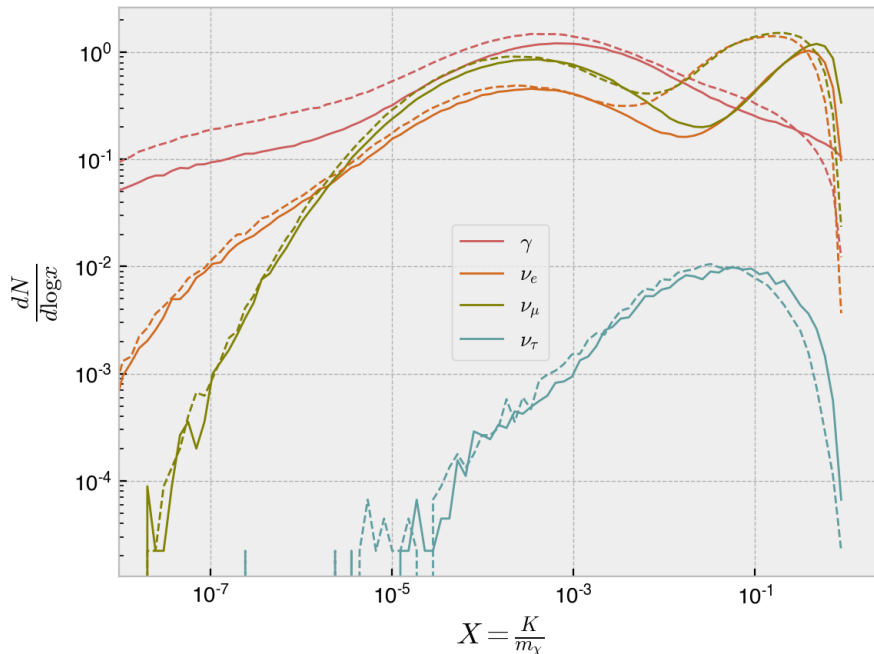


Figure 4.5: Comparison of stable particle energy spectra  $dN/d\log x$  coming from  $\chi\bar{\chi} \rightarrow \mu^+\mu^-$  and  $\chi\bar{\chi} \rightarrow Z'Z'$  subsequently decaying into muons. We have considered  $m_\chi = 10$  TeV and  $m_{Z'} = 9800$  GeV for  $2 \rightarrow 2$  and  $m_{Z'} = 4900$  GeV for  $2 \rightarrow 4$  case. Different colours in the panel label the various energy spectra:  $\gamma$ ,  $\nu_e$ ,  $\nu_\mu$  and  $\nu_\tau$ . Continuous lines represent the products of dark matter annihilation into two muons while the dashed lines represent final products of muons originated from decays of the 2  $Z'$ . Both cases were simulated with PYTHIA8 requiring  $5 \cdot 10^5$  events and include EW showering effects.

Being the energy spectra approximately similar we have adopted the approximation of  $2 \rightarrow 2$  case for the  $2 \rightarrow 4$  case. We used this approximation for the KM3NeT predictions as well.

We report in fig. 4.6 the results of numerical simulations. The left panel shows illustrates the interplay between  $\langle\sigma v\rangle$  and the experimental constraints, as labelled in the figure. The solid red line represent the maximum value of  $\langle\sigma v\rangle$  for each value of  $Z'$ . In this case, the intersection points are: (i)  $m_\chi = 1.5$  TeV for Fermi-LAT upper limit and (ii)  $m_\chi = 2.4$  TeV for KM3NeT (2). One can conclude that Fermi-LAT probes the region of the parameter space with mass up to 1.5 TeV, while KM3NeT (2) will be sensitive to masses up to 2.4 TeV. Notice that KM3NeT (1) line is completely below with respect to the red line, meaning that it probably would be able to constrain the entire considered mass range.

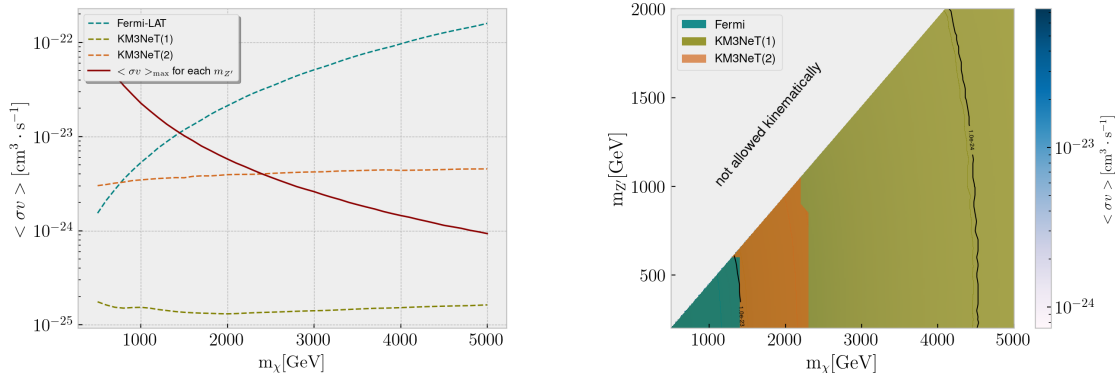


Figure 4.6: **Secluded:  $m_\chi \simeq m_{Z'}$  case** The left panel is a 2D plot in  $m_\chi - \langle \sigma v \rangle$  plane representing the considered experimental constrain provided by Fermi-LAT data and predictions for upper limit of the future KM3NeT compared to max values of  $\langle \sigma v \rangle_{\max}$  for each value of  $m_{Z'}$ , as labelled. The right panel represents the model parameter space with the experimental constrains. The grey region is not allowed kinematically; experimental constrains are labelled as in the figure. The whole parameter space considered here can be probed by KM3NeT (1).

The left panel of fig. 4.6 shows the excluded regions of parameter space  $m_\chi - m_{Z'}$ . The grey region is not kinematically allowed for the considered process. All the parameter space is excluded by the prediction of the upper limit of KM3NeT (1) which incorporate both KM3NeT (2) prediction and Fermi-LAT experimental bound. Moreover, Fermi-LAT can exclude region of parameter space for  $m_\chi \simeq 1.5$  TeV and  $m_{Z'} \simeq 0.6$  TeV, while KM3NeT (2) would be able to explore region with  $m_\chi \simeq 2.2$  TeV and  $m_{Z'} \simeq 1$  GeV.

### 4.7.3 Secluded models: $m_{Z'} \ll m_\chi$ case

For this case we have considered the  $m_\chi$  in range  $[500 - 10^4]$  GeV and  $m_{Z'}$  in range  $[10^{-3} - 240]$  GeV. We have included the Sommerfeld enhancement factor described in sec. 4.7.1. To compute the  $S$  factor we considered eqs. (4.32) and (4.35): in the limit of negligible mass boson, we have considered the  $S$  factor due to a Coulomb potential; otherwise we have considered the  $S$  factor from a Yukawa potential. The two different expressions are normalized introducing a factor between eq. 4.32 and eq. 4.35, taking a benchmark point for each of them.

In left panel of fig. 4.7 is the 3D plot of  $\langle \sigma v \rangle$  including Sommerfeld enhancement. The enhancement of  $\langle \sigma v \rangle$  is nearly two orders of magnitude. Notice that it shows the typical resonance structure due to the Sommerfeld resonances. In right panel of fig. 4.7 is shown the parameter space of  $m_\chi - m_{Z'}$  with excluded regions by two experimental constrains. Fermi-LAT excludes the region with  $m_\chi$  up to 0.7 TeV and  $m_{Z'}$  up to 0.08

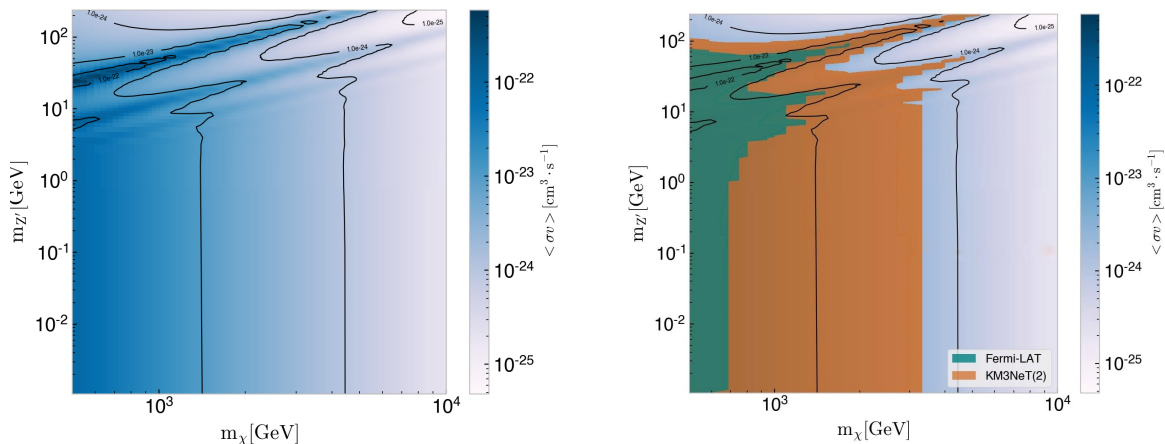


Figure 4.7: **Secluded:  $m_{Z'} \ll m_\chi$  case** Left panel shows the velocity averaged cross section  $\langle\sigma v\rangle$  including Sommerfeld enhancement as a function of  $m_\chi - m_{Z'}$ . It shows the typical resonance structure. Black lines are added as reference for numerical values. The right panel shows the parameter space of  $\langle\sigma v\rangle$  explored with Fermi-LAT upper limit and potential prediction for the future KM3NeT (2) which are labelled as in figure. A large portion of the parameter space would be excluded by KM3NeT (2).

TeV. The prediction for KM3NeT (2) limit overwrite completely Fermi-LAT exclusion and potentially can probe the region of parameter space with  $m_\chi \simeq 3.3$  TeV and  $m_{Z'}$  up to 0.1 TeV.

## 4.8 $L_\mu - L_\tau$ gauge model

A possible ultraviolet completion for the Dark Sector can be obtained considering the gauging of  $L_\mu - L_\tau$  symmetry associated to  $U'(1)$  abelian group. If this symmetry is broken a massive  $Z'$  boson is present, with model independent mass and couplings to the Standard Model particles. Actually, with in the particle content of the Standard Model it is possible to gauge one of the three differences of lepton flavours  $L_e - L_\mu$ ,  $L_e - L_\tau$  or  $L_\mu - L_\tau$  without introducing an anomaly. In particular,  $L_\mu - L_\tau$  should be preferred over the two other two combinations because in the limit of conserved symmetry, the neutrino mass matrix is automatically  $\mu - \tau$  symmetric and predicts one degenerate neutrino pair. The necessary breaking of the symmetry will split their masses and generate small departures from the  $\mu - \tau$  symmetry, reproducing the neutrino phenomenology in agreement with current data [103].

An important property of the gauged  $L_\mu - L_\tau$  symmetry is that it does not affect the first generation of leptons, but only muons and taus. This symmetry was introduced to

explain an anomaly in the rare  $B \rightarrow K^*, \mu^+ \mu^-$  observed by the LHCb collaboration in 2013 [104]. Another motivation for the model is the possibility of an explanation for the anomalous magnetic moment of the muon using loop-contribution of the heavy  $Z'$  gauge boson present in this kind of theories [103].

The model has further been extended to include a dark matter candidate. One considers dark matter candidate connected to Standard Model particles via the new gauge interaction [105, 106, 107].

The simplified model discussed in the previous sections can be embedded in the framework of this theory. Indeed, we consider the minimal Dark sector composed by  $Z'$  boson associated to the  $L_\mu - L_\tau$  symmetry and by Dirac fermionic dark matter which we assume to be charged under the new local symmetry.

The dark matter phenomenology is then dictated by gauge interactions mediated by the massive  $Z'$  which couples to the second and third lepton generations. All these requirements are the same as for sec. 4.3.

Here we repeat our consideration in more rigorous way. Gauging the symmetry, the new gauge boson couples to the Standard Model fields via the covariant derivative

$$D_\alpha = \partial_\alpha + ig' q_{\mu-\tau} Z', \quad (4.38)$$

where  $g'$  is the  $U(1)_{\mu-\tau}$  coupling strength and  $q_{\mu-\tau}$  the corresponding charge; the interaction with leptons then is

$$\mathcal{L}_{\text{SM}} \supset q_l g' (\bar{l}_2 \gamma_\alpha l_2 - \bar{l}_3 \gamma_\alpha l_3 + \bar{\mu}_R \gamma_\alpha \mu_R - \bar{\tau}_R \gamma_\alpha \tau_R) Z'^\alpha, \quad (4.39)$$

where  $q_l$  is the free parameter which quantifies the overall charge of the considered leptons under the  $L_\mu - L_\tau$  symmetry. Making explicit the above equation

$$\mathcal{L}_{\text{SM}} \supset q_l g' (\bar{\mu} \gamma_\alpha \mu - \bar{\tau} \gamma_\alpha \tau + \bar{\nu}_\mu \gamma_\alpha P_L \nu_\tau - \bar{\nu}_\tau \gamma_\alpha P_L \nu_\tau) Z'^\alpha. \quad (4.40)$$

dark matter, singlet under the Standard Model gauge group, is charged under this new  $U(1)_{\mu-\tau}$  as well. The gauge boson  $Z'$  interacts with the dark matter through

$$\mathcal{L}_{\text{DM}} \supset q_\chi g' \bar{\chi} \gamma_\alpha \chi Z'^\alpha, \quad (4.41)$$

where  $q_\chi$  is the dark matter charged under the  $U(1)_{\mu-\tau}$  symmetry. In our case we keep  $q_l = 1$  without loss of generality and  $q_\chi = q_l$  or in other words we assume that Dirac fermionic dark matter  $\chi$  features a "universal coupling" to the  $Z'$ , equal to that of leptons.

Notice that the Lagrangian is the same of eq. (4.4), except that the first generation of leptons is excluded, and the same processes shown in fig. 4.1 are allowed.  $\langle \sigma v \rangle$  is the same as in eq. (4.18) for 2 massless lepton final state and as in eq. (4.20) for the production of two bosons subsequently decaying in the Standard Model particles.

Since in this model dark matter particles do not interact directly with quarks, scattering off of nuclei occurs only through a loop. The basic idea is that dark matter-nucleon

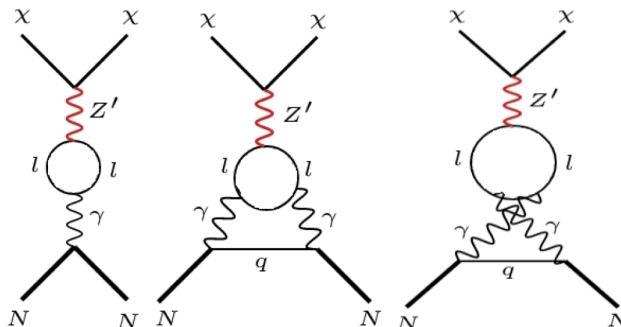


Figure 4.8: Feynman diagrams describing spin-independent dark matter-nucleon scattering at the loop level. The left diagram describes one loop interaction while the other two are 2-loop diagrams which are suppressed. Diagrams taken from [105].

scattering can be described in terms of virtual charged leptons running in the loop that couple to both the mediator  $Z'$  and the photon which couples to nucleons. This process is described by the Feynman diagrams in fig. 4.8. The 2-loop diagrams are suppressed and therefore negligible. Adopting the result in [108], the expression for dark matter-nucleon interaction cross section is

$$\sigma_{SI} = \frac{1}{A^2} \frac{\mu_N}{9\pi} \left( \frac{\alpha_{\text{em}} Z g^2 q_\chi q_l}{\pi m_{Z'}^2} \log \left( \frac{m_\mu^2}{m_\tau^2} \right) \right)^2, \quad (4.42)$$

where  $A$  is the mass number,  $Z$  is the atomic number,  $m_N$  is the nucleus mass,  $q_l$  and  $q_\chi$  are gauge-group charges.  $\sigma_{SI}$  is  $v$ -independent because  $Z'$  boson has vector-like interactions with both the charged leptons and dark matter.

For direct detection, we have considered XENON1T upper limit. Xenon has  $Z = 54$  and  $m_N \simeq 129 \text{ GeV}$ . (4.42) has the dependence on  $(\log(m_\mu/m_\tau))^2$  because it is a leading log approximation to the Renormalization Group Equation [105].

We have compute the same analysis as in sec. 4.6 and 4.7 looking at how the parameter space can be excluded via the experimental constrains described in sec. 3.4.

In the first case we have analyzed the annihilation of dark matter particles in mass range  $[190 - 10^5] \text{ GeV}$ , assuming massless final states considering  $Z'$  couplings to both the dark matter and the Standard Model with  $g_{\text{SM}} = g_{\text{DM}} = 1$ . The numerical simulations has been performed with MADDM computing energy spectra of stable particles with the PPC4DMIDew tables [92]. Being the branching ratio the same for all the final state leptons, we have considered  $6 \cdot \langle \sigma v \rangle$  of single lepton. Left panel of fig. 4.9 is a 2D plot showing the comparison between  $\langle \sigma v \rangle_{\text{max}}$  chosen for each value of  $m_\chi$ , considering different masses of  $m_{Z'}$ . These values are represented via the solid bordeaux line. Looking at intersection points of Fermi-LAT experimental upper limit and prediction for future

#### 4.8. $L_\mu - L_\tau$ GAUGE MODEL

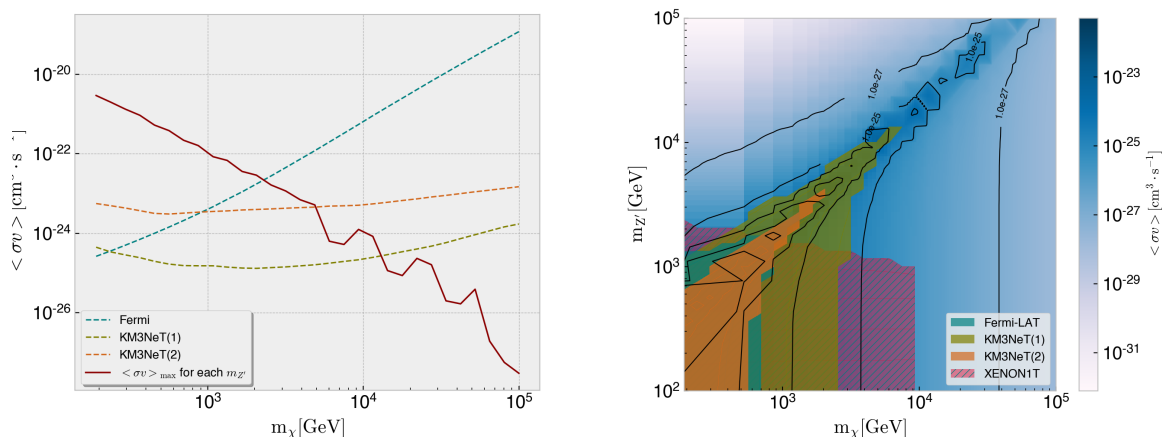


Figure 4.9:  $L_\mu - L_\tau : 2 \rightarrow 2$  case The 2D left plot represents the comparison between  $\langle \sigma v \rangle_{\max}$  chosen for each value of  $m_{Z'}$  (solid bordeaux line) compared with the experimental constraints, as labelled in the legend, as function of  $m_\chi$ . The right panel represents the 3D colormap showing the model parameter space excluded via different experimental upper limits, as labelled. The parameter space of the model is mostly constrained by XENON1T and will be probed by KM3NeT (1) which incorporates both Fermi-LAT and KM3NeT (2).

KM3NeT, labelled as in figure, and red line, we can find the following values: (i) Fermi-LAT arrives up to 2.3 TeV, (ii) KM3NeT (1) up to 13 TeV and (iii) KM3NeT (2) up to 5 TeV. The right panel shows the 3D plot with excluded regions. The main part of the parameter space is excluded by XENON1T: we have used the analytic expression of eq. 4.42 and we compared it with XENON1T upper limit. Indeed, it probes the parameter space up to 2.2 TeV for  $m_{Z'}$  and  $m_\chi$  up to 9.8 TeV. Fermi-LAT upper limit on  $\langle \sigma v \rangle$  excludes the region of  $m_\chi - m_{Z'}$  plane up to 0.7 TeV and 1.3 TeV respectively. KM3NeT (2) would overlap Fermi-LAT upper limit and would arrive to exclude regions with masses up to 1.8 TeV for  $m_\chi$  and  $m_{Z'} \simeq 3.8$  TeV. The KM3NeT (1) would explore the region with  $m_\chi \simeq 7$  TeV and  $m_{Z'} \simeq 12$  TeV. The black lines in the plot are only indicative and are used just for easier reading of the colormap.

For the second case we have considered a dark matter mass in the range  $[500 - 10^4]$  GeV while  $m_{Z'}$  varies between  $[0.1 - 240]$  GeV. The theoretical predictions for the velocity averaged cross sections have been done with MADDM using MADEVENT for the  $\langle \sigma v \rangle$  computation and PYTHIA8 for the computation of energy spectra of stable particles. In this case we have added the Sommerfeld enhancement, as described in sec. 4.7.1. We have used both limits for the Sommerfeld factors: for a light boson with  $m_{Z'} < 0.9$  GeV and high masses of dark matter  $m_\chi > 5000$  GeV we used  $S$  factor from Coulomb potential being the mediator mass very light compared with the mass of dark matter. Otherwise

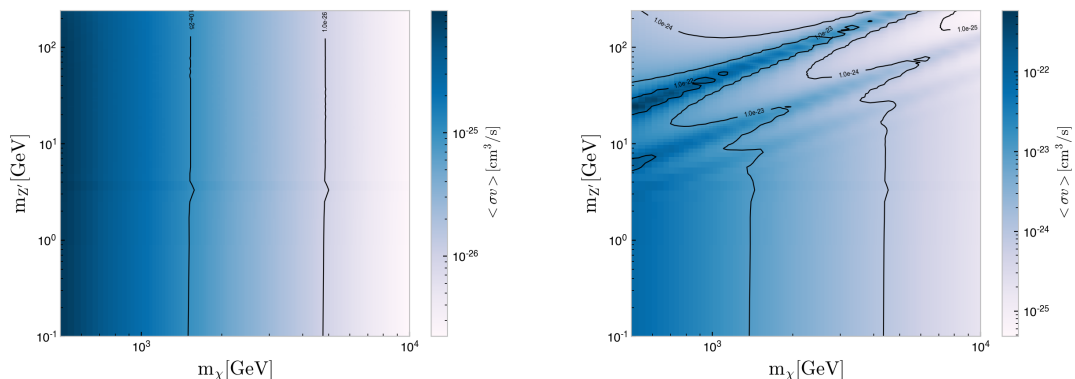


Figure 4.10: Comparison of  $\langle\sigma v\rangle$  with and without Sommerfeld enhancement. The left panel shows the results without including  $S$ , while the right one represents  $\langle\sigma v\rangle$  adding the Sommerfeld factor. The right panel shows the typical resonant structure. Black lines are added as a reference for the numerical values.

we considered the  $S$  factor from the Yukawa potential. Moreover, we have found the normalization matching between two expressions eq. (4.32) and eq. (4.35), computing both of them in a benchmark point. In left panel fig. 4.10 are compared two plots: the left one represents  $\langle\sigma v\rangle$  with Sommerfeld enhancement factor. The enhancement of the cross section is nearly two orders of magnitude and it shows the typical resonances due to the Sommerfeld factor.

In the right panel of fig. 4.11 we have implemented the Fermi-LAT and XENON1T experimental bounds and prediction for the upper limits of future KM3NeT. To compute the scattering cross section between dark matter and Xenon nucleus we have used eq. (4.42) with  $A = 131$  and  $m_N = 129$  GeV and we compared the result with the upper limit for SI cross section of XENON1T experiment. This upper limit excludes the lower part of the parameter space, constraining  $m_{Z'}$  masses up to 1.9 GeV. The Fermi-LAT upper limit explores the parameter space for low values of  $m_\chi$ , namely up to 1.7 TeV and  $m_{Z'}$  up to 17 GeV. The larger part of parameter space would be excluded by KM3NeT (2), which would constrains  $m_\chi - m_{Z'}$  masses up to 3.5 TeV and 240 GeV respectively.

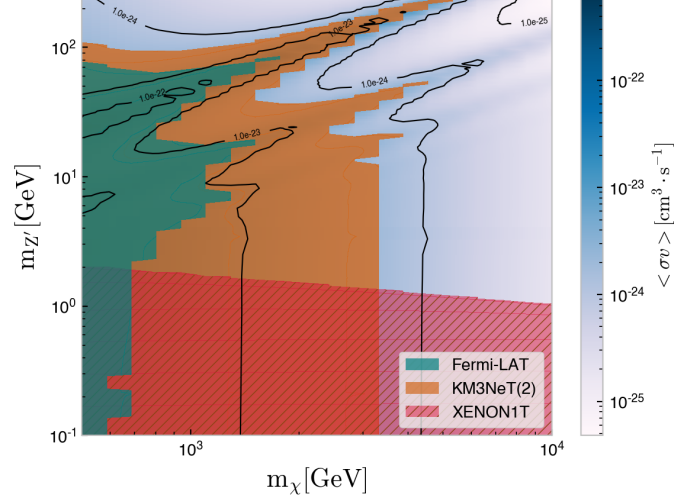


Figure 4.11:  $L_\mu - L_\tau : 2 \rightarrow 4$  case 3D  $\langle \sigma v \rangle$  plot in  $m_\chi - m_{Z'}$  parameter space, where the experimental constrains for direct and indirect detection are compared with the theoretical predictions and to the future sensitivity of KM3NeT, as labelled. A large part of the parameter space will be probed via KM3NeT(2), while the lower part is constrained by the XENON1T experiment.

# Chapter 5

## Conclusions and outlook

In this thesis we analyzed a spin 1-s-channel simplified model describing dark matter annihilation into leptons through a massive  $Z'$  boson. We motivated our choice for leptophilic model, by our interest in establishing the reach of the future KM3NeT neutrino telescope. In particular, the neutrino energy spectrum can lead to very clear signatures of dark matter annihilation. Moreover, this model provides an annihilation cross section which is velocity independent and as a consequence it is not velocity suppressed.

We considered Dirac fermionic dark matter, singlet under the Standard Model gauge group, and a  $Z'$  massive boson which couples to both the Standard Model sector and the dark matter sector. After having built the Lagrangian describing the interactions between the dark matter and the Standard Model, we studied two different processes: (i)  $2 \rightarrow 2$  and (ii)  $2 \rightarrow 4$ .

In the first case (i), we considered the dark matter and  $Z'$  masses in the range GeV-TeV and both couplings of  $Z'$   $g_{\text{SM}} = g_{\text{DM}} = 1$ . We explored the parameter space importing experimental constrains for indirect and direct detection: for the former we implemented the Fermi-LAT upper limit on  $\langle\sigma v\rangle$  while for the direct detection we considered the XENON1T exclusion bound for spin independent interactions.

For second case (ii), we introduced a secluded scenario in which two mediator bosons are produced from the annihilation of dark matter particles. These bosons subsequently decay producing four leptons in total. For our analysis, we considered two different mass range: (1) same settings as in case (i) and (2)  $m_{Z'} \ll m_\chi$ , namely a very light vector mediator, which can give rise to Sommerfeld enhanced annihilation cross sections. In both cases we tested how the parameter space of the sampled models can be probed by the future neutrino telescope KM3NeT.

In the last part of our analysis, we treated the  $L_\mu - L_\tau$  gauge symmetry: in this case the  $Z'$  is the gauge boson associated to this  $U(1)$  Abelian symmetry. Even if the phenomenology is expected to be similar to simplified model we treat, this model is anomaly free. We repeated an analysis similar to the case of the minimal  $Z'$  model, focusing the attention on the  $2 \rightarrow 2$  and  $2 \rightarrow 4$  annihilation processes. We further

---

implemented the experimental constraints and projections for the reach of KM3NeT for this scenario, on the line of the above studies.

Our numerical results were obtained with the dark matter software MADDM: this numerical tool, using an UFO model, can compute relevant observables for dark matter detection and provide experimental constraints. Another numerical tool that we used is RUNDM: being MADDM unable to handle loops, to compute the dark matter-Nucleon interaction cross section. We run our coupling from the GeV-TeV scale of the mediator mass down to the nuclear scale, relevant for direct detection.

For our analysis, we have used two different predictions for KM3NeT sensitivity, considering the angular power spectrum method (a) and the prediction made with a likelihood analysis based on the ANTARES data (b). Both of them have been considered for  $2 \rightarrow 2$  processes and we have found that (b) is more promising, being able to exclude a larger region of the parameter space with masses up to 10 TeV along the resonance region  $m_{Z'} = 2m_\chi$ , as one can see considering right panels of fig. 4.3 and 4.9. In the case of  $2 \rightarrow 4$  process and for the secluded model with  $m_\chi \simeq m_{Z'}$ , we could approximate the energy spectra of four leptons with those of two leptons but with  $Z'$  mass twice the standard case. In this case, (b) is able to exclude a larger part of the parameter region as well, as shown in the right panel of fig. 4.6. For the secluded model with  $m_\chi \gg m_{Z'}$ , we have available only the (a) prediction for KM3NeT: in both the secluded scenario and the secluded  $L_\mu - L_\tau$  case, it was able to exclude the model parameter space up to few TeV for  $m_\chi$  and 240 GeV for  $m_{Z'}$ , as shown in right panel of fig. 4.9 and fig. 4.11. KM3NeT predictions are very promising, compared with Fermi-LAT data, being able to constrain larger regions of the parameter space; this is true for all the considered cases. Furthermore, it is interesting to notice that XENON1T upper limits are able to constrain large regions as well, even if the considered models are leptophilic: the dark matter-nucleon scattering can occur only through loops. In case of simplified model loops are independent on dark sector and are due only to Standard Model particles: RUNDM provides the correct RGE for couplings. In case of  $L_\mu - L_\tau$  gauge symmetry, the strongest constraint comes from the kinetic mixing between the  $Z'$  and the  $Z$  gauge boson, generated at one loop level.

There are several possibilities to improve the present analysis. Concerning the theoretical part, one can sample other promising simplified models, as for example a  $t$ -channel model for Dirac fermionic dark matter and a scalar mediator. This model in particular is well motivated by supersymmetric models in which the neutralino is a pure wino and interacts solely with the supersymmetric scalars and the fermions. Furthermore, other well known gauge symmetries can be extended to embed a dark matter candidate: for example, instead of gauging the lepton number symmetry, one can gauge  $B - L$ , the difference between baryon number and lepton number, which is a global accidental symmetry of the Standard Model. In the latter case the couplings to quarks are turned on, implying that the model will receive additional constraints from collider searches.

From a numerical point of view, it is possible to improve the software MADDM by

---

adding the capability to compute one-loop interactions for direct detection, as these were the leading contributions in our case. Moreover, the KM3NeT exclusion limits can be included among the experimental constrains released with the software, once the neutrino telescope construction is completed and it becomes fully operative.

# Bibliography

- [1] PLANCK collaboration, *Planck 2018 results. VI. Cosmological parameters*, *Astron. Astrophys.* **641** (2020) A6 [1807.06209].
- [2] L. Bergstrom, *Dark Matter Candidates*, *New J. Phys.* **11** (2009) 105006 [0903.4849].
- [3] S. P. Martin, *A Supersymmetry primer*, *Adv. Ser. Direct. High Energy Phys.* **21** (2010) 1 [hep-ph/9709356].
- [4] M. Drewes et al., *A White Paper on keV Sterile Neutrino Dark Matter*, *JCAP* **01** (2017) 025 [1602.04816].
- [5] C. El Aisati, C. Garcia-Cely, T. Hambye and L. Vanderheyden, *Prospects for discovering a neutrino line induced by dark matter annihilation*, *JCAP* **10** (2017) 021 [1706.06600].
- [6] A. Berlin, D. Hooper and S. D. McDermott, *Simplified Dark Matter Models for the Galactic Center Gamma-Ray Excess*, *Phys. Rev. D* **89** (2014) 115022 [1404.0022].
- [7] F. Ambrogio, C. Arina, M. Backovic, J. Heisig, F. Maltoni, L. Mantani et al., *MadDM v.3.0: a Comprehensive Tool for Dark Matter Studies*, *Phys. Dark Univ.* **24** (2019) 100249 [1804.00044].
- [8] FERMI-LAT collaboration, *Fermi Large Area Telescope Fourth Source Catalog*, *Astrophys. J. Suppl.* **247** (2020) 33 [1902.10045].
- [9] XENON collaboration, *First Dark Matter Search Results from the XENON1T Experiment*, *Phys. Rev. Lett.* **119** (2017) 181301 [1705.06655].
- [10] KM3NET collaboration, *Letter of intent for KM3NeT 2.0*, *J. Phys. G* **43** (2016) 084001 [1601.07459].
- [11] A. Dekker, M. Chianese and S. Ando, *Probing dark matter signals in neutrino telescopes through angular power spectrum*, *JCAP* **09** (2020) 007 [1910.12917].

---

BIBLIOGRAPHY

---

- [12] KM3NET, ANTARES collaboration, *Searches for dark matter with the ANTARES and KM3NeT neutrino telescopes*, *PoS ICRC2019* (2020) 552.
- [13] E. W. Kolb and M. S. Turner, *The early universe*, vol. 69. 1990.
- [14] P. Coles and F. Lucchin, *Cosmology: The Origin and Evolution of Cosmic Structure, Second Edition*. 2002.
- [15] M. Bauer and T. Plehn, *Yet Another Introduction to Dark Matter: The Particle Physics Approach*, vol. 959 of *Lecture Notes in Physics*. Springer, 2019, 10.1007/978-3-030-16234-4, [1705.01987].
- [16] D. Bauman, “Cosmology part iii.” dbaumann@damtp.cam.ac.uk, 7, 2019.
- [17] D. Tong, “Lectures on cosmology.” [www.damtp.cam.ac.uk/user/tong/cosmo.html](http://www.damtp.cam.ac.uk/user/tong/cosmo.html).
- [18] D. H. Rogstad and G. S. Shostak, *Gross Properties of Five Scd Galaxies as Determined from 21-CENTIMETER Observations*, **176** (1972) 315.
- [19] G. Bertone and D. Hooper, *History of dark matter*, *Rev. Mod. Phys.* **90** (2018) 045002 [1605.04909].
- [20] D. J. Fixsen, *The Temperature of the Cosmic Microwave Background*, **707** (2009) 916 [0911.1955].
- [21] PLANCK collaboration, *Planck 2015 results. I. Overview of products and scientific results*, *Astron. Astrophys.* **594** (2016) A1 [1502.01582].
- [22] K. Garrett and G. Duda, *Dark Matter: A Primer*, *Adv. Astron.* **2011** (2011) 968283 [1006.2483].
- [23] A. Schneider, R. E. Smith and D. Reed, *Halo Mass Function and the Free Streaming Scale*, *Mon. Not. Roy. Astron. Soc.* **433** (2013) 1573 [1303.0839].
- [24] S. D. M. White, C. S. Frenk, M. Davis and G. Efstathiou, *Clusters, filaments, and voids in a universe dominated by cold dark matter*, *Astrophys. J.* **313** (1987) 505.
- [25] J. L. Feng, *Dark Matter Candidates from Particle Physics and Methods of Detection*, *Ann. Rev. Astron. Astrophys.* **48** (2010) 495 [1003.0904].
- [26] T. Lin, *Dark matter models and direct detection*, *PoS* **333** (2019) 009 [1904.07915].
- [27] Y.-F. Li, *Detection Prospects of the Cosmic Neutrino Background*, *Adv. Ser. Direct. High Energy Phys.* **25** (2015) 233 [1504.03966].

---

BIBLIOGRAPHY

---

- [28] R. D. Peccei and H. R. Quinn, *CP conservation in the presence of pseudoparticles*, *Phys. Rev. Lett.* **38** (1977) 1440.
- [29] D. M. Jacobs, G. D. Starkman and B. W. Lynn, *Macro Dark Matter*, *Mon. Not. Roy. Astron. Soc.* **450** (2015) 3418 [1410.2236].
- [30] E. Witten, *Cosmic separation of phases*, *Phys. Rev. D* **30** (1984) 272.
- [31] A. Atreya, A. Sarkar and A. M. Srivastava, *Reviving quark nuggets as a candidate for dark matter*, *Phys. Rev. D* **90** (2014) 045010 [1405.6492].
- [32] Y. Bai, A. J. Long and S. Lu, *Dark Quark Nuggets*, *Phys. Rev. D* **99** (2019) 055047 [1810.04360].
- [33] H.-C. Cheng, J. L. Feng and K. T. Matchev, *Kaluza-Klein dark matter*, *Phys. Rev. Lett.* **89** (2002) 211301 [hep-ph/0207125].
- [34] A. Birkedal, A. Noble, M. Perelstein and A. Spray, *Little Higgs dark matter*, *Phys. Rev. D* **74** (2006) 035002 [hep-ph/0603077].
- [35] F. Quevedo, S. Krippendorff and O. Schlotterer, *Cambridge Lectures on Supersymmetry and Extra Dimensions*, 1011.1491.
- [36] J. F. Navarro, C. S. Frenk and S. D. M. White, *The Structure of cold dark matter halos*, *Astrophys. J.* **462** (1996) 563 [astro-ph/9508025].
- [37] J. Einasto, *On the Construction of a Composite Model for the Galaxy and on the Determination of the System of Galactic Parameters*, *Trudy Astrofizicheskogo Instituta Alma-Ata* **5** (1965) 87.
- [38] A. Burkert, *The Structure of dark matter halos in dwarf galaxies*, *IAU Symp.* **171** (1996) 175 [astro-ph/9504041].
- [39] T. Bringmann and C. Weniger, *Gamma Ray Signals from Dark Matter: Concepts, Status and Prospects*, *Phys. Dark Univ.* **1** (2012) 194 [1208.5481].
- [40] C. Garcia-Cely and J. Heeck, *Indirect searches of dark matter via polynomial spectral features*, *JCAP* **08** (2016) 023 [1605.08049].
- [41] ICECUBE collaboration, *Search for Neutrinos from Dark Matter Self-Annihilations in the center of the Milky Way with 3 years of IceCube/DeepCore*, *Eur. Phys. J. C* **77** (2017) 627 [1705.08103].
- [42] FERMI-LAT collaboration, *Updated search for spectral lines from Galactic dark matter interactions with pass 8 data from the Fermi Large Area Telescope*, *Phys. Rev. D* **91** (2015) 122002 [1506.00013].

---

BIBLIOGRAPHY

---

- [43] I. Esteban, M. C. Gonzalez-Garcia, M. Maltoni, I. Martinez-Soler and T. Schwetz, *Updated fit to three neutrino mixing: exploring the accelerator-reactor complementarity*, *JHEP* **01** (2017) 087 [1611.01514].
- [44] A. Ibarra, S. Lopez Gehler and M. Pato, *Dark matter constraints from box-shaped gamma-ray features*, *JCAP* **07** (2012) 043 [1205.0007].
- [45] P. Ciafaloni, D. Comelli, A. Riotto, F. Sala, A. Strumia and A. Urbano, *Weak Corrections are Relevant for Dark Matter Indirect Detection*, *JCAP* **03** (2011) 019 [1009.0224].
- [46] M. Schumann, *Direct Detection of WIMP Dark Matter: Concepts and Status*, *J. Phys. G* **46** (2019) 103003 [1903.03026].
- [47] M. C. Smith et al., *The RAVE Survey: Constraining the Local Galactic Escape Speed*, *Mon. Not. Roy. Astron. Soc.* **379** (2007) 755 [astro-ph/0611671].
- [48] T. Marrodán Undagoitia and L. Rauch, *Dark matter direct-detection experiments*, *J. Phys. G* **43** (2016) 013001 [1509.08767].
- [49] W. de Boer, *Precision Experiments at LEP*, *Adv. Ser. Direct. High Energy Phys.* **23** (2015) 107 [1509.06050].
- [50] A. Costantini, F. De Lillo, F. Maltoni, L. Mantani, O. Mattelaer, R. Ruiz et al., *Vector boson fusion at multi-TeV muon colliders*, *JHEP* **09** (2020) 080 [2005.10289].
- [51] L. Evans and P. Bryant, *LHC machine*, *Journal of Instrumentation* **3** (2008) S08001.
- [52] H1AND FOR THE ZEUS collaboration, *Parton Distribution Functions*, in *31st International Symposium on Physics In Collision*, 11, 2011, 1111.5452.
- [53] S. Y. Hoh, J. R. Komaragiri and W. A. T. Wan Abdullah, *Dark matter searches at the large hadron collider*, *AIP Conference Proceedings* **1704** (2016) 020005 [<https://aip.scitation.org/doi/pdf/10.1063/1.4940063>].
- [54] HESS collaboration, *Search for  $\gamma$ -Ray Line Signals from Dark Matter Annihilations in the Inner Galactic Halo from 10 Years of Observations with H.E.S.S.*, *Phys. Rev. Lett.* **120** (2018) 201101 [1805.05741].
- [55] J. Coronado-Blázquez and M. A. Sánchez-Conde, *Constraints to dark matter annihilation from high-latitude HAWC unidentified sources*, *Galaxies* **8** (2019) 5 [2001.02536].

---

BIBLIOGRAPHY

---

- [56] L. E. Strigari, *Dark matter in dwarf spheroidal galaxies and indirect detection: a review*, *Rept. Prog. Phys.* **81** (2018) 056901 [1805.05883].
- [57] J. Bolmont et al., *The camera of the fifth H.E.S.S. telescope. Part I: System description*, *Nucl. Instrum. Meth. A* **761** (2014) 46 [1310.5877].
- [58] HAWC collaboration, *Dark Matter Searches with HAWC*, *PoS ICRC2017* (2018) 891 [1708.07461].
- [59] V. A. Acciari, T. Arlen, T. Aune, M. Beilicke, W. Benbow, D. Boltuch et al., *VERITAS SEARCH FOR VHE GAMMA-RAY EMISSION FROM DWARF SPHEROIDAL GALAXIES*, *The Astrophysical Journal* **720** (2010) 1174.
- [60] C. A. Argüelles, A. Diaz, A. Kheirandish, A. Olivares-Del-Campo, I. Safa and A. C. Vincent, *Dark Matter Annihilation to Neutrinos*, 1912.09486.
- [61] ICECUBE collaboration, *The IceCube Upgrade – Design and Science Goals*, *PoS ICRC2019* (2020) 1031 [1908.09441].
- [62] ANTARES collaboration, *Search for dark matter towards the Galactic Centre with 11 years of ANTARES data*, *Phys. Lett. B* **805** (2020) 135439 [1912.05296].
- [63] D. Akerib, H. Araújo, X. Bai, A. Bailey, J. Balajthy, E. Bernard et al., *The lux experiment*, *Physics Procedia* **61** (2015) 74.
- [64] LUX collaboration, *Technical Results from the Surface Run of the LUX Dark Matter Experiment*, *Astropart. Phys.* **45** (2013) 34 [1210.4569].
- [65] XENON collaboration, *The XENON1T Dark Matter Experiment*, *Eur. Phys. J. C* **77** (2017) 881 [1708.07051].
- [66] SUPERCDMS Soudan collaboration, *Demonstration of Surface Electron Rejection with Interleaved Germanium Detectors for Dark Matter Searches*, *Appl. Phys. Lett.* **103** (2013) 164105 [1305.2405].
- [67] S. collaboration, *SuperCDMS supercdms experiment*, 2021.
- [68] R. Cerulli, P. Villar, F. Cappella, R. Bernabei, P. Belli, A. Incicchitti et al., *DAMA annual modulation and mirror Dark Matter*, *Eur. Phys. J. C* **77** (2017) 83 [1701.08590].
- [69] J. Schieck et al., *Direct Dark Matter Search with the CRESST II Experiment*, *PoS ICHEP2016* (2016) 217 [1611.02113].
- [70] M. Bossa, *DarkSide-50, a background free experiment for dark matter searches*, *Journal of Instrumentation* **9** (2014) C01034.

---

BIBLIOGRAPHY

---

- [71] COSINE-100 collaboration, *Search for a Dark Matter-Induced Annual Modulation Signal in NaI(Tl) with the COSINE-100 Experiment*, *Phys. Rev. Lett.* **123** (2019) 031302 [1903.10098].
- [72] DEAP collaboration, *Search for dark matter with a 231-day exposure of liquid argon using DEAP-3600 at SNOLAB*, *Phys. Rev. D* **100** (2019) 022004 [1902.04048].
- [73] SUPERCDMS collaboration, *Search for Low-Mass Weakly Interacting Massive Particles Using Voltage-Assisted Calorimetric Ionization Detection in the SuperCDMS Experiment*, *Phys. Rev. Lett.* **112** (2014) 041302 [1309.3259].
- [74] C. Boehm, D. G. Cerdeño, P. A. N. Machado, A. Olivares-Del Campo, E. Perdomo and E. Reid, *How high is the neutrino floor?*, *JCAP* **01** (2019) 043 [1809.06385].
- [75] A. collaboration, *ATLAS collaboration atlas results*, 2021.
- [76] E. Morgante, *Simplified Dark Matter Models*, *Adv. High Energy Phys.* **2018** (2018) 5012043 [1804.01245].
- [77] C. Arina, B. Fuks and L. Mantani, *A universal framework for t-channel dark matter models*, *Eur. Phys. J. C* **80** (2020) 409 [2001.05024].
- [78] H. Ruegg and M. Ruiz-Altaba, *The Stueckelberg field*, *Int. J. Mod. Phys. A* **19** (2004) 3265 [hep-th/0304245].
- [79] F. Kahlhoefer, K. Schmidt-Hoberg, T. Schwetz and S. Vogl, *Implications of unitarity and gauge invariance for simplified dark matter models*, *JHEP* **02** (2016) 016 [1510.02110].
- [80] T. Hahn, *Generating Feynman diagrams and amplitudes with FeynArts 3*, *Comput. Phys. Commun.* **140** (2001) 418 [hep-ph/0012260].
- [81] V. Shtabovenko, R. Mertig and F. Orellana, *New Developments in FeynCalc 9.0*, *Comput. Phys. Commun.* **207** (2016) 432 [1601.01167].
- [82] E. Bagnaschi et al., *Global Analysis of Dark Matter Simplified Models with Leptophobic Spin-One Mediators using MasterCode*, *Eur. Phys. J. C* **79** (2019) 895 [1905.00892].
- [83] G. Arcadi, Y. Mambrini and F. Richard, *Z-portal dark matter*, *JCAP* **03** (2015) 018 [1411.2985].

---

BIBLIOGRAPHY

---

- [84] G. Bélanger, F. Boudjema, A. Goudelis, A. Pukhov and B. Zaldivar, *micrOMEGAs5.0 : Freeze-in*, *Comput. Phys. Commun.* **231** (2018) 173 [1801.03509].
- [85] T. Bringmann, J. Edsjö, P. Gondolo, P. Ullio and L. Bergström, *DarkSUSY 6 : An Advanced Tool to Compute Dark Matter Properties Numerically*, *JCAP* **07** (2018) 033 [1802.03399].
- [86] A. Alloul, N. D. Christensen, C. Degrande, C. Duhr and B. Fuks, *Feynrules 2.0 a complete toolbox for tree-level phenomenology*, *Computer Physics Communications* **185** (2014) 2250.
- [87] M. Backovic, K. Kong and M. McCaskey, *MadDM v.1.0: Computation of Dark Matter Relic Abundance Using MadGraph5*, *Physics of the Dark Universe* **5-6** (2014) 18 [1308.4955].
- [88] M. Backović, A. Martini, O. Mattelaer, K. Kong and G. Mohlabeng, *Direct Detection of Dark Matter with MadDM v.2.0*, *Phys. Dark Univ.* **9-10** (2015) 37 [1505.04190].
- [89] J. Alwall, R. Frederix, S. Frixione, V. Hirschi, F. Maltoni, O. Mattelaer et al., *The automated computation of tree-level and next-to-leading order differential cross sections, and their matching to parton shower simulations*, *JHEP* **07** (2014) 079 [1405.0301].
- [90] F. Maltoni and T. Stelzer, *MadEvent: Automatic event generation with MadGraph*, *JHEP* **02** (2003) 027 [hep-ph/0208156].
- [91] T. Sjöstrand, S. Ask, J. R. Christiansen, R. Corke, N. Desai, P. Ilten et al., *An introduction to PYTHIA 8.2*, *Comput. Phys. Commun.* **191** (2015) 159 [1410.3012].
- [92] M. Cirelli, G. Corcella, A. Hektor, G. Hutsi, M. Kadastik, P. Panci et al., *PPPC 4 DM ID: A Poor Particle Physicist Cookbook for Dark Matter Indirect Detection*, *JCAP* **03** (2011) 051 [1012.4515].
- [93] LUX collaboration, *Results from a search for dark matter in the complete LUX exposure*, *Phys. Rev. Lett.* **118** (2017) 021303 [1608.07648].
- [94] LUX collaboration, *Limits on spin-dependent WIMP-nucleon cross section obtained from the complete LUX exposure*, *Phys. Rev. Lett.* **118** (2017) 251302 [1705.03380].
- [95] PICO collaboration, *Dark Matter Search Results from the PICO-60 C<sub>3</sub>F<sub>8</sub> Bubble Chamber*, *Phys. Rev. Lett.* **118** (2017) 251301 [1702.07666].

---

BIBLIOGRAPHY

---

- [96] F. D’Eramo, B. J. Kavanagh and P. Panci, *You can hide but you have to run: direct detection with vector mediators*, *JHEP* **08** (2016) 111 [1605.04917].
- [97] A. Crivellin, F. D’Eramo and M. Procura, *New Constraints on Dark Matter Effective Theories from Standard Model Loops*, *Phys. Rev. Lett.* **112** (2014) 191304 [1402.1173].
- [98] F. D’Eramo and M. Procura, *Connecting Dark Matter UV Complete Models to Direct Detection Rates via Effective Field Theory*, *JHEP* **04** (2015) 054 [1411.3342].
- [99] FERMI-LAT, DES collaboration, *Searching for Dark Matter Annihilation in Recently Discovered Milky Way Satellites with Fermi-LAT*, *Astrophys. J.* **834** (2017) 110 [1611.03184].
- [100] A. Sommerfeld, *Über die beugung und bremsung der elektronen*, *Annalen der Physik* **403** (1931) 257.
- [101] N. Arkani-Hamed, D. P. Finkbeiner, T. R. Slatyer and N. Weiner, *A Theory of Dark Matter*, *Phys. Rev. D* **79** (2009) 015014 [0810.0713].
- [102] J. L. Feng, M. Kaplinghat and H.-B. Yu, *Sommerfeld Enhancements for Thermal Relic Dark Matter*, *Phys. Rev. D* **82** (2010) 083525 [1005.4678].
- [103] J. Heeck and W. Rodejohann, *Gauged  $L_\mu - L_\tau$  Symmetry at the Electroweak Scale*, *Phys. Rev. D* **84** (2011) 075007 [1107.5238].
- [104] LHCb collaboration, *Measurement of Form-Factor-Independent Observables in the Decay  $B^0 \rightarrow K^{*0} \mu^+ \mu^-$* , *Phys. Rev. Lett.* **111** (2013) 191801 [1308.1707].
- [105] W. Altmannshofer, S. Gori, S. Profumo and F. S. Queiroz, *Explaining dark matter and B decay anomalies with an  $L_\mu - L_\tau$  model*, *JHEP* **12** (2016) 106 [1609.04026].
- [106] P. Schwaller, T. M. P. Tait and R. Vega-Morales, *Dark Matter and Vectorlike Leptons from Gauged Lepton Number*, *Phys. Rev. D* **88** (2013) 035001 [1305.1108].
- [107] E. Madge and P. Schwaller, *Leptophilic dark matter from gauged lepton number: Phenomenology and gravitational wave signatures*, *JHEP* **02** (2019) 048 [1809.09110].
- [108] J. Kopp, V. Niro, T. Schwetz and J. Zupan, *DAMA/LIBRA and leptonically interacting Dark Matter*, *Phys. Rev. D* **80** (2009) 083502 [0907.3159].
- [109] K. B. P. P. D’eramo, F., *runDM (Version 1.0) [Computer software]*, .